Ab initio prediction of crystalline phases and their electronic properties : from ambient to extreme pressures

Jingming Shi

N° d'ordre NNT : 2017LYSE1110

THÈSE DE DOCTORAT DE L'UNIVERSITÉ DE LYON
opérée au sein de
l'Université Claude Bernard Lyon 1

École Doctorale ED52
Physique et d'Astrophysique de Lyon

Spécialité de doctorat :
Discipline : Physique

Soutenue publiquement le 06/07/2017, par :
Jingming SHI

Ab initio prediction of crystalline phases and their electronic properties : from ambient to extreme pressures

---

Devant le jury composé de :

NIEHAUS Thomas, Professeur, Université Claude Bernard Lyon 1	Président
BLASE Xavier, Directeur de Recherches CNRS, Institut Néel, Grenoble	Rapporteur
SAITTA Marco, Professeur, Université Pierre et Marie Curie-Paris-Sorbonne	Rapporteur
RADESCU Silvana, Professeur, Universidad de la Laguna	Examinatrice
MARTINET Christine, IR CNRS, Université Claude Bernard Lyon 1	Examinatrice
MARQUES Miguel, Professeur, Martin-Luther-Universität	Examinateur
BOTTI Silvana, Professeur, Friedrich-Schiller University of Jena	Co-directrice de thèse
SAN MIGUEL Alfonso, Professeur, Université Claude Bernard Lyon 1	Directeur de thèse

Abstract

In this thesis we use global structural prediction methods (Particle Swarm Optimization and Minima Hopping Method) and high-throughput techniques to predict crystal structures of different systems under different conditions. We performed structural prediction by using the Crystal structure Analysis by Particle Swarm Optimization(CALYPSO) combined with Density Functional Theory (DFT) that made possible to unveil several stable compounds, so far unknown, on the phase diagrams of Ba–Si and N–H–O. Afterwards, we performed a high-throughput investigation on ternary compounds of composition ABX_2, where A and B are elements of the periodic table up to Bi, and X is a chalcogen (O, S, Se, and Te) by using DFT and combining calculations of crystal prototypes with structural prediction (Minima Hopping Method). The following paragraphs summarize the content by chapter of this document.

Chapter 1 is a short introduction of this thesis.

Chapter 2 includes the basic theory used in this thesis. Firstly, a short introduction of DFT is presented. Then, we describe some approximate exchange-correlation functions that make DFT practical. Next, we introduce different structural prediction algorithms, especially Particle Swarm Optimization and Minima Hopping Method which we used in this thesis. Finally, we discuss how to determine if a new structure is thermodynamically stable.

In Chapter 3, we first consider the Ba–Si system. Using an unbiased structural search based on a particle-swarm optimization algorithm combined with DFT calculations, we investigate systematically the ground-state phase stability and structural diversity of Ba–Si binaries at high pressure. The phase diagram turns out to be quite intricate, with several compositions stabilizing/destabilizing as a function of pressure. In particular, we identify novel phases of BaSi, $BaSi_2$, $BaSi_3$, and $BaSi_5$ that might be synthesizable experimentally over a wide range of pressures. Our results not only clarify and complete the previously known structural phase diagram, but also provide new insights for understanding the Ba–Si binary system.

Chapter 4 contains the investigation of the phases diagram of the N–H–O system. By using an *ab initio* evolutionary structural search, we report the prediction of two novel stable crystalline phases in the N–H–O ternary phase diagram at high pressure, namely NOH_4 and

HNO_3 (nitric acid). Our calculations reveal that the new $C2/m$ phase of NOH_4 becomes stable at 71 GPa, while the $P2_1/m$ phase of HNO_3 stabilizes at 39 GPa. Both phases remain thermodynamically stable at least up to 150 GPa, the maximum pressure we considered. The $C2/m$ phase of NOH_4 contains two O–H layers and one "dumbbell cluster" layer formed by two NH_3 molecules linked by a N–N covalent bond. The $P2_1/m$ phase of HNO_3 contains a surprising "quasi clover" layer formed N–O–H covalent bonds. Further calculations show that both phases are semiconductors, with a band gap of 6.0 eV and 2.6 eV for NOH_4 and NHO_3, respectively. We also confirmed that the composition NOH_5 (NH_3H_2O) becomes unstable at pressures above 122 GPa, decomposing into NH_3 and H_2O.

Chapter 5 focuses on p-type transparent electrodes of ternary chalcogenides. We use a high-throughput approach based on DFT to find delafossite and related layered phases of composition ABX_2, where A and B are elements of the periodic table, and X is a chalcogen (O, S, Se, and Te). From the 15 624 compounds studied in the trigonal delafossite prototype structure, 285 are within 50 meV/atom from the convex hull of stability. These compounds are further investigated using global structural prediction methods to obtain their lowest-energy crystal structure. We find 79 systems not present in the "materials project database" that are thermodynamically stable and crystallize in the delafossite or in closely related structures. These novel phases are then characterized by calculating their band gaps and hole effective masses. This characterization unveils a large diversity of properties, ranging from normal metals, magnetic metals, and some candidate compounds for *p*-type transparent electrodes.

At the end of the thesis, we give our general conclusions and an outlook.

Résumé

Dans cette thèse nous utilisons des méthodes globaux de prédiction des structures cristallographiques avec les algorithmes d'optimisation par essaims particuliers (« Particle Swarm Optimization » en anglais) et de « Minima Hopping Method » combinés à des techniques de grande capacité de traitement de données afin de prédire la structure cristalline de différents systèmes et dans des conditions thermodynamiques variées. Nous avons réalisé des prédictions structurales utilisant l'analyse cristalline par optimisation par essaims particuliers (CALYPSO) combinés avec la Théorie Fonctionnelle de la Densité (DFT) ce qui a permis de mettre en évidence la stabilité de plusieurs composés jusqu'à la inconnus dans le digramme de phases du système Ba–Si et dans le système N–H–O. Nous avons également réalisé une étude à haute capacité de traitement de données sur un système ternaire de composition ABX_2, avec A et B des éléments du tableau périodique allant jusqu'au bismuth et X étant un chalcogénure (O, S, Se ou Te) . Nous avons utilisé la Théorie Fonctionnelle de la Densité combinant calculs de prototypes structuraux à partir des prédictions structurelles avec la méthode de « Minima Hopping ». Dans les paragraphes suivants nous résumons le contenu de différents chapitres de cette thèse.

Le premier chapitre qui constitue une brève introduction au travail de cette thèse est suivi du chapitre 2 présentant les aspects théoriques utilisés dans ce travail. D'abord il est fait une brève introduction à la Théorie Fonctionnelle de la Densité. A continuation nous décrivons quelques fonctions d'échange-corrélation choisies qui constituent des approximations rendant l'utilisation de la DFT efficace. Ensuite nous présentons différents procédés de prédiction structurale, et en particulier les algorithmes d'optimisation par essaims particuliers et de « Minima Hopping » eu nous avons utilisés dans cette thèse. Finalement il est discuté comment doit-on se prendre pour évaluer la stabilité thermodynamique des nouvelles phases identifiées.

Dans le chapitre 3, nous considérons le système Ba-Si. A travers l'utilisation d'une recherche structurale non-biaisée basée sur l'algorithme d'optimisation par essaims particuliers combinée avec des calculs DFT, nous faisons une étude systématique de la stabilité des phases et de la diversité structurale du système binaire Ba-Si sous haute pression. Le diagramme de phases résultant est assez complexe avec plusieurs compositions se stabilisant et se déstabilisant en fonction de la pression. En particulier, nous avons identifié des nouvelles

phases de stœchiométrie BaSi, $BaSi_2$, $BaSi_3$ et $BaSi_5$ qui devraient pouvoir être synthétisées expérimentalement dans un domaine de pressions étendu. Nos résultants permettent non seulement de compléter le diagramme de phase de Ba–Si, mais ils donnent plus largement des clefs pour la compréhension du système binaire Ba–Si.

Dans le chapitre 4 est présentée notre étude du diagramme de phases du système N–H–O. S'appuyant sur une recherche structural «évolutive » de type ab initio, nous prédisons deux nouvelles phases du système ternaire N–H–O qui sont NOH4 et HNO_3 (acide nitrique). La nouvelle phase de NOH_4 a une symétrie $C2/m$ et devient stable à partir de 71 GPa tandis que la phase $P2_1/m$ de HNO_3 est stabilisée à 39 GPa. Les deux phases restent thermodynamiquement stables jusqu'à 150 GPa, la pression limite de notre étude. La phase $C2/m$ de NOH_4 présente deux couches O–H et une couche de type agrégat d'haltères formée de deux molécules NH_3 connectées par des liaisons covalentes N–N. La phase $P2_1/m$ de HNO_3 (acide nitrique) contient une couche surprenante de type quasi-trèfle formée des liaisons covalentes N–O–H. Le calcul de la structure électronique montre que les deux phases sont semiconductrices. Les gaps électroniques pour les phases de NOH_4 et NHO_3 sont de 6.0 et 2.6 eV respectivement. Nous confirmons également que la composition NOH_5 (NH_3H_2O) perd son stabilité pour des pressions supérieures à 122 GPa se décomposant en NH_3 et H_2O à cette pression.

Le chapitre 5 se focalise sur les électrodes transparentes de type-p à base des chalcogénures ternaires. Nous utilisons une approche à grande capacité de traitement de données basée sur la DFT pour obtenir la delafossite et d'autres phases voisines de composition ABX_2, avec A et B des éléments du tableau périodique et X des chalcogénures (O, S, Se et Te). A partir d'an total de 15624 composés étudiés dans la structure prototypique de la delafossite, 285 structures se trouvent dans la limite de stabilité d'enveloppe convexe avec une marge de dispersion de 50 meV/atome. Ces composés sont étudiés par les méthodes de prédiction structurale afin d'obtenir leur structure cristalline de plus basse énergie. Nous trouvons 79 systèmes qui sont absents de la base de données « Materials project database », qui sont stables du point de vue thermodynamique et qui cristallisent soit dans la structure delafossite, soit dans des structures très proches. Ces nouvelles phases sont ensuite caractérisées déterminant leur gap électronique et la masse effective des trous. Cette caractérisation révèle une grande diversité de propriétés allant depuis les métaux ordinaires aux métaux magnétiques et permettant d'identifier quelques candidats pour des électrodes transparents de type-p.

Nous présentons enfin à la fin du manuscrit nos conclusions générales et les perspectives de ce travail.

Contents

Chapter 1

Introduction

The discovery of new materials often lies at the base of important innovations for industrial applications. Moreover, it provides insight into fundamental scientific issues. We can obtain new materials by tailoring intrinsic materials parameters that can be controlled during synthesis and processing, such as dimensionality, composition and geometric size of the sample features. On the other hand, we can also use external conditions to induce changes in the material, such as temperature, pressure, electric, magnetic fields or others. In particular, pressure is a fundamental thermodynamic variable that can be used to control the properties of materials, because it can reduce interatomic distances, change bond patterns and profoundly modify electronic orbitals. It is thus a powerful tool for finding novel materials that are inaccessible at ambient conditions. Pressure can enable the creation of new materials mainly through four routes. Firstly, pressure can produce new materials through structural phase transitions. High pressure can change the energetics of the various possible structures by altering the interatomic distances and bonding patterns thus stabilizing new materials. A well known example is synthetic diamond which is made by the compression of graphite. The sp^2 C–C bonding in graphite changes into sp^3 C–C bonding in diamond due to the applied pressure. Secondly, pressure can stabilize new stoichiometries. Structural phase transitions originate from qualitative changes in the potential energy landscape. Pressure can also effectively modify the compositional landscape, leading to stabilization of the exotic stoichiometries that would not be expected from the conventional wisdom based on chemical rules at ambient conditions. Examples include Li_xAl_{1-x} [1], Na_xAu_{1-x} [2] and unusual stoichiometries of hydrogen sulfide H_3S [3]. Thirdly, pressure can enable new chemical reactions. Pressure can affect the chemical reactivity of elements by influencing the electronic orbitals and their occupancy. The outer atomic orbitals (such as the s, p and d orbitals) will hybridize as a result of the changing of the energetic ordering of the orbitals induced by pressure. Finally, pressure can change the electronic properties of materials.

Even in the case when the structure and stoichiometry remain unchanged under pressure, the electronic properties can be fundamentally modified, because pressure can reduce the interatomic distances and strengthen interatomic interactions. This can broaden energy bands thus enabling insulator-to-metal, semiconductor-to-metal or metal-to-superconductor transitions. For example, superconductivity of $BaSi_2$ changes remarkably under pressure [4]. The main goals of this thesis are to discover new stoichiometries and new phases of the Ba–Si and N–H–O systems under high pressure and to explore their properties and the underlying physical mechanisms. Our study can give us a fundamental understanding and potential applications and prospects of these two systems.

As the demand for the materials is endlessly growing, high-throughput computational materials design also became a burgeoning area in recent years, in particular, because experimental discovery is bound by high costs and is very time-consuming. The high-throughput computational materials design is based on the marriage between computational quantum-mechanical-thermodynamic approaches and a multitude of techniques rooted in database construction and intelligent data mining. The concept is simple yet powerful: create a large database containing the calculated thermodynamic and electronic properties of existing and hypothetical materials, and then intelligently interrogate the database in the search of materials with the desired properties. Clearly, the entire construction should be validated by reality, namely the existing materials must be predicted correctly and the hypothetical ones should be eventually synthesized. Such reality check feeds back to the theory to construct better databases and increased predictive power. With the advent of efficient and accurate theoretical tools and inexpensive computers, high-throughput computational materials design has become an important tool for finding new materials. This method has successfully screened many different kind of materials and applications, such as solar energy harvesting [5], water photospliting [6], carbon capture and gas storage [7], topological insulators [8] and thermoelectric materials [9]. In the domaing solar energy harvesting, another goal of this thesis is to find delafossite and related layered phases of composition ABX_2 which possess p-type transparent conduction, where A and B are elements of the periodic table, and X is a chalcogen (O, S, Se, and Te) by using high-throughput computational materials design. This study can provide precious indications for further experimental synthesis and opens the way for more specific theoretical and experimental studies of dopability and transport properties, which can be restricted only to the most interesting candidates.

This thesis is organized as follows: Chapter 2 is an introduction to the theoretical framework. Then Chapter 3 and Chapter 4 are about novel phases of the Ba–Si system under high pressure and the phases diagram of the N–H–O system under high pressure. Chapter 5 is concerned with the investigation of ternary chalcogenides for p-type transparent electrodes

through high-throughput computational materials design. Finally, in Chapter 6 we present a summary and relevant conclusions of this thesis.

Chapter 2

Theoretical background

Ab initio or first-principles methods have emerged in the last two decades as a powerful tool to probe the properties of matter at the microscopic scale. These approaches are used to derive macroscopic observables under the controlled condition of a "computational experiment," and with a predictive power rooted in the quantum-mechanical description of interacting atoms and electrons. Density functional theory (DFT) has become the default method of choice for most applications, due to its combination of reasonable scaling with system size and good accuracy in reproducing most ground state properties. Such an electronic structure approach can then be combined with molecular dynamics to provide an accurate description of thermodynamic properties and phase stability, atomic dynamics, and chemical reactions, or as a tool to sample the features of a potential energy surface. Due to the development of computer technology, large and complex systems are now accessible. For example, the largest system that simulated with DFT contains over 2 million atoms [10].

In this chapter, I will introduce the basic concepts and methods that were used in this thesis. As DFT is one of the most basic theoretical tools, I give a short introduction of this theory. Then, in the following sections, I describe different structural prediction algorithms. Finally, I give a discussion on the stability of crystal phases.

2.1 Density functional theory

We consider a N-electron system (atom, molecule, or solid) in the Born-Oppenheimer approximation [11] and non-relativistic approximation. The Schrödinger equation [12] can be written as

$$\hat{H}\Psi(\mathbf{x}_1,\mathbf{x}_2,\ldots,\mathbf{x}_N) = E\Psi(\mathbf{x}_1,\mathbf{x}_2,\ldots,\mathbf{x}_N)\,, \tag{2.1}$$

where $\mathbf{x}_i$ comprehends the spatial and spin coordinates of electron i $(\mathbf{r}_i, \sigma_i)$. The Hamiltonian operator is formally written as

$$\hat{H} = \hat{T} + \hat{V}_{\text{ext}} + \hat{V}_{\text{ee}}\,, \tag{2.2}$$

where

$$\hat{T} = -\sum_{i=1}^{N} \frac{1}{2}\nabla_i^2\,, \tag{2.3}$$

is the kinetic enery operator,

$$\hat{V}_{\text{ext}} = \sum_{i=1}^{N} v_{\text{ext}}(\mathbf{r}_i)\,, \tag{2.4}$$

$$v_{\text{ext}}(\mathbf{r}_i) = -\sum_{I} \frac{Z_I}{r_{iI}}\,, \tag{2.5}$$

is the sum of the external potential operators. Here, capital indices stand for the nuclear coordinates and Z_I is the atomic number of the nuclei I. Hartree atomic units are used throughout. Furthermore

$$\hat{V}_{\text{ee}} = \sum_{i<j}^{N} \frac{1}{\mathbf{r}_{ij}}\,, \tag{2.6}$$

$$\mathbf{r}_{ij} = |\mathbf{r}_i - \mathbf{r}_j|\,, \tag{2.7}$$

is the electron-electron interaction operator. To obtain the total energy of the system we have also to add the nuclei-nuclei repulsive energy contribution,

$$V_{\text{nn}} = \sum_{I<J} \frac{Z_I Z_J}{r_{IJ}}\,. \tag{2.8}$$

2.1.1 The Hohenberg-Kohn theorem

Consider an electronic system with an arbitrary external local potential v_{ext}. The corresponding ground-state wave function Ψ can be obtained by solving the Schrödinger equation (2.1), from which the associated ground-state density $n_0(\mathbf{r})$ can be deduced. Therefore, one has a mapping from the potential v_{ext} to the ground-state density $n_0(\mathbf{r})$. In 1964, Hohenberg and Kohn [13] showed that this mapping can be inverted, i.e, the ground-state density $n_0(\mathbf{r})$ determines the potential v_{ext} up to an arbitrary addictive constant. This can be easily proved

by *reductio ad absurdum*. The ground-state density $n_0(\mathbf{r})$ determines the potential v_{ext}, which in turn determines the Hamiltonian, and everything about the many-body problem. In other words, the potential v is a unique (up to an additive constant) functional of the ground-state density n, and for instance the ground-state wave function Ψ is also a unique functional of n (which can be denoted by $\Psi[n]$). Consequently, Hohenberg and Kohn defined the universal (i.e., independent from the external potential) density functional

$$F[n] = \langle \Psi[n] | \, \hat{T} + \hat{V}_{\text{ee}} \, | \Psi[n] \rangle \, , \tag{2.9}$$

which can be used to define the total electronic energy under an external potential v_{ext} as a functional of the density:

$$\begin{aligned} E_{v_{\text{ext}}}[n] &= \langle \Psi | \, \hat{T} + \hat{V}_{\text{ext}} + \hat{V}_{\text{ee}} \, | \Psi \rangle \\ &= F[n] + \int d\mathbf{r} \, n(\mathbf{r}) v_{\text{ext}}(\mathbf{r}) \, . \end{aligned} \tag{2.10}$$

Hohenberg and Kohn further showed that the density functional $E_{v_{\text{ext}}}[n]$ satisfies a variational property: The ground-state energy E_0 of the system considered is obtained by minimizing this functional with respect to $N-$electron densities n that are ground-state densities associated with some local potential (referred to as v-representable densities)

$$E_0 = \min_{\{n\}} E_{v_{\text{ext}}}[n] \, . \tag{2.11}$$

the minimum being reached for the ground-state density $n_0(\mathbf{r})$ corresponding to the potential v_{ext}. This can also be written as

$$\frac{\delta}{\delta n(\mathbf{r})} \left[E_{v_{\text{ext}}}[n] - \mu \int n(\mathbf{r}) \, d\mathbf{r} \right] = \frac{\delta F[n]}{\delta n(\mathbf{r})} + v_{\text{ext}}(\mathbf{r}) - \mu = 0 \, . \tag{2.12}$$

where μ is a Lagrange multiplier that ensures the normalization of the density to the total number of electrons. Therefore, solving Eq. (2.12) would give us the exact ground-state of any electronic system.

The existence of a mapping from a ground-state density to a local potential, the existence of the universal density functional, and the variational property with respect to the density constitute the Hohenberg-Kohn theorem. Even though the original Hohenberg-Kohn theorem assumes a nondegenerate ground-state, it was showed later that the theorem is in fact also valid for a degenerate ground states (see, e.g., Ref. 12).

2.1.2 Kohn-Sham equations

As we discussed above, Hohenberg and Kohn in 1964 presented two theorems that are the core of the modern DFT [13]. They are known as the first and second Hohenberg-Kohn theorems. The Hohenberg-Kohn theorems tell us that the ground-state energy is a functional of the electronic density, however, the form of this functional remains unknown. The energy include kinetic energy and exchange-correlation energy parts which can not be written as an explicit functional of the density. To deal with this problem, Kohn and Sham considered an explicit system of non-interacting electrons ($\hat{V}_{\text{ee}} = 0$) with the same density of the real system [14]. In this case, the many-body ground state wave function can be written as a Slater determinant of single particle wave functions ψ_i,

$$\Psi_s(\mathbf{x}_1, \mathbf{x}_2, \ldots, \mathbf{x}_N) = \frac{1}{\sqrt{N!}} \begin{vmatrix} \psi_1(\mathbf{r}_1) & \psi_2(\mathbf{r}_1) & \cdots & \psi_N(\mathbf{r}_1) \\ \psi_1(\mathbf{r}_2) & \psi_2(\mathbf{r}_2) & \cdots & \psi_N(\mathbf{r}_2) \\ \vdots & \vdots & \ddots & \vdots \\ \psi_1(\mathbf{r}_N) & \psi_2(\mathbf{r}_N) & \cdots & \psi_N(\mathbf{r}_N) \end{vmatrix}, \tag{2.13}$$

that satisfy:

$$\left[-\frac{1}{2}\nabla^2 + v_{\text{KS}}(\mathbf{r}) \right] \psi_i(\mathbf{r}) = \varepsilon_i \psi_i(\mathbf{r}) \,. \tag{2.14}$$

Here, v_{KS} is a fictitious external potential. The ground-state density is obtained from the N lowest occupied orbitals and can be written as:

$$n(\mathbf{r}) = \sum_{i=1}^{N} |\psi_i(\mathbf{r})|^2 \,. \tag{2.15}$$

For the interacting system, the universal functional can be written as

$$F_{\text{HK}}[n] = T_s[n] + E_{\text{H}}[n] + E_{\text{xc}}[n] \,, \tag{2.16}$$

where $E_{\text{H}}[n]$ is the Hartree energy functional

$$E_{\text{H}}[n] = \frac{1}{2} \int d\mathbf{r} \int d\mathbf{r}' \, \frac{n(\mathbf{r})\, n(\mathbf{r}')}{|\mathbf{r} - \mathbf{r}'|} \,, \tag{2.17}$$

that represents the classical electrostatic repulsion energy for the charge distribution. While T_s is the independent-particle kinetic energy that can be given by

$$T_s = -\frac{1}{2} \sum_{i=1}^{N} \langle \psi_i | \nabla^2 | \psi_i \rangle = \frac{1}{2} \sum_{i=1}^{N} |\nabla \psi_i|^2 \,, \tag{2.18}$$

$E_{\mathrm{xc}}[n]$ is the exchange-correlation energy functional that remains to be approximate. This function can be written as

$$E_{\mathrm{xc}}[n] = F_{\mathrm{HK}}[n] - (T_s[n] + E_{\mathrm{H}}[n])\,, \tag{2.19}$$

or in the more revealing form

$$E_{\mathrm{xc}}[n] = T[n] + V_{\mathrm{ee}}[n] - (T_s[n] + E_{\mathrm{H}}[n])\,. \tag{2.20}$$

which contains a kinetic contribution and a potential contribution. With these modified potentials the Euler equation of the Hohenberg-Kohn equation (2.12) can be written as

$$\frac{\delta T_s[n]}{\delta n(\mathbf{r})} + v_{\mathrm{ext}}(\mathbf{r}) + \frac{1}{2}\int d\mathbf{r}'\,\frac{n(\mathbf{r}')}{|\mathbf{r}-\mathbf{r}'|} + \frac{\delta E_{\mathrm{xc}}[n]}{\delta n(\mathbf{r})} - \mu = 0\,. \tag{2.21}$$

We then define the Kohn-Sham potential

$$v_{\mathrm{KS}}[n](\mathbf{r}) = v_{\mathrm{ext}}(\mathbf{r}) + v_{\mathrm{H}}[n](\mathbf{r}) + v_{\mathrm{xc}}[n](\mathbf{r})\,, \tag{2.22}$$

where

$$v_{\mathrm{H}}[n](\mathbf{r}) = \frac{1}{2}\int d\mathbf{r}'\,\frac{n(\mathbf{r}')}{|\mathbf{r}-\mathbf{r}'|}\,, \tag{2.23}$$

$$v_{\mathrm{xc}}[n](\mathbf{r}) = \frac{\delta E_{\mathrm{xc}}[n]}{\delta n(\mathbf{r})}\,. \tag{2.24}$$

The Euler equation of the Hohenberg-Kohn equation (2.21) can be rewritten as

$$\frac{\delta T_s[n]}{\delta n(\mathbf{r})} + v_{\mathrm{KS}}[n](\mathbf{r}) - \mu = 0\,. \tag{2.25}$$

Solving this equation is equivalent to solving the single-particle Schrödinger equation:

$$\left[-\frac{1}{2}\nabla^2 + v_{\mathrm{KS}}[n](\mathbf{r})\right]\psi_i(\mathbf{r}) = \varepsilon_i\psi_i(\mathbf{r})\,. \tag{2.26}$$

Equations (2.25) and (2.26) are known as the Kohn-Sham equations [15]. The orbitals satisfying (2.26) are called the Kohn-Sham orbitals. The Kohn-Sham Hamiltonian can be written as:

$$\hat{H}_{\mathrm{KS}} = -\frac{1}{2}\nabla^2 + v_{\mathrm{KS}}[n](\mathbf{r})\,, \tag{2.27}$$

v_{KS} is called Kohn-Sham potential. The Kohn-Sham equations are similar to the Hartree-Fock equations, with the difference that they involve a local exchange potential instead of a nonlocal one, and an additional local correlation potential.

2.2 Making DFT practical: approximations

We review here the main classes of approximate exchange-correlation functionals. These classes are roughly ordered from the simplest to the most sophisticated ones. The discussion is focused on the contents of the approximations, not their performance in practical calculations. On average, more sophisticated approximations are usually more accurate than simpler ones, even though many exceptions can be found.

2.2.1 The local density approximation

In the local-density approximation (LDA), introduced by Kohn and Sham [15], the exchange-correlation functional is written as

$$E_{\mathrm{xc}}^{\mathrm{LDA}}[n] = \int n(\mathbf{r})\varepsilon_{\mathrm{xc}}^{\mathrm{unif}}(n(\mathbf{r}))dr\,, \tag{2.28}$$

where $\varepsilon_{\mathrm{xc}}^{\mathrm{unif}}(n)$ is the exchange-correlation energy per particle of the infinite uniform electron gas with the density n. The uniform electron gas represents a family of systems of interacting electrons with an arbitrary spatially constant density n that acts as a parameter. Thus, in the LDA, the exchange-correlation energy per particle of an inhomogeneous system at a spatial point of density $n(\mathbf{r})$ is approximated as the exchange-correlation energy per particle of the uniform electron gas of the same density.

The function $\varepsilon_{\mathrm{xc}}^{\mathrm{unif}}(n)$ is a sum of exchange and correlation contributions,

$$\varepsilon_{\mathrm{xc}}^{\mathrm{unif}}(n) = \varepsilon_{\mathrm{x}}^{\mathrm{unif}}(n) + \varepsilon_{\mathrm{c}}^{\mathrm{unif}}(n)\,. \tag{2.29}$$

The exchange energy per particle of the uniform electron gas can be calculated analytically

$$\varepsilon_{\mathrm{x}}^{\mathrm{unif}}(n) = c_{\mathrm{x}} n^{1/3}\,, \tag{2.30}$$

where

$$c_{\mathrm{x}} = -(3/4)(3/\pi)^{1/3}\,. \tag{2.31}$$

The LDA exchange functional is associated with the names of Dirac [16] and Slater [17].

The correlation energy per particle $\varepsilon_{\rm c}^{\rm unif}(n)$ of the uniform electron gas can not be calculated analytically. This quantity has been obtained numerically for a number of densities n using accurate quantum Monte Carlo calculations [18], and fitted to a parametrized function of n satisfying the known high- and low-density expansions. Expressed in terms of the Wigner-Seitz radius $r_{\rm s} = (3/(4\pi n))^{1/3}$, the first terms of the high-density expansion ($r_{\rm s} \to 0$) have the form

$$\varepsilon_{\rm c}^{\rm unif}(n) = A\ln r_{\rm s} + B + Cr_{\rm s}\ln r_{\rm s} + O(r_{\rm s})\,, \tag{2.32}$$

and the first terms of the low-density expansion ($r_{\rm s} \to +\infty$) have the form

$$\varepsilon_{\rm c}^{\rm unif}(n) = \frac{a}{r_{\rm s}} + \frac{b}{r_{\rm s}^{3/2}} + O(\frac{1}{r_{\rm s}^2})\,, \tag{2.33}$$

where A, B, C, a, and b are constants. The two most used parameterizations are the one of Vosko, Wilk, and Nusair (VWN) [19] and the one of Perdew and Wang (PW92) [20]. Their forms are too complicated to be given here. These parameterizations also include the generalization to spin densities $\varepsilon_{\rm c}^{\rm unif}(n_\uparrow, n_\downarrow)$ differing from $\varepsilon_{\rm c}^{\rm unif}(n)$ for spin-polarized systems ($n_\uparrow \neq n_\downarrow$) (sometimes specifically referred to as the local-spin-density (LSD) approximation).

2.2.2 Generalized gradient approximations

The next logical step beyond the LDA is the gradient-expansion approximation (GEA). One way of deriving the GEA is to start from the uniform electron gas, introduce a weak and slowly-varying external potential $v_{\mathbf{r}}$, and expand the exchange- correlation energy in terms of the gradients of the density. At second order, one obtains a functional of the form

$$E_{\rm xc}^{\rm GEA}(n) = E_{\rm xc}^{\rm LDA}(n) + \int C_{\rm xc} n(\mathbf{r})^{4/3} \left(\frac{\nabla n(\mathbf{r})}{n(\mathbf{r})^{4/3}} \right)^2 dr\,, \tag{2.34}$$

where

$$C_{\rm xc} = C_{\rm x} + C_{\rm c}\,, \tag{2.35}$$

is the sum of the exchange and correlation coefficients of the second order gradient expansion. Note that the gradient expansion is most naturally written in terms of the reduced density gradient $\nabla n(\mathbf{r})/n(\mathbf{r})^{4/3}$ which is a dimensionless quantity. The GEA should improve over the LDA provided that the reduced density gradient is small. Unfortunately, for real systems, the reduced density gradient can be large in some regions of space, and the GEA turns out to be a worse approximation than the LDA.

The failure of the GEA lead to the development of generalized-gradient approximations (GGA), which really started in the 1980s, of the generic form

$$E_{\mathrm{xc}}^{\mathrm{GGA}}(n) = \int n(\mathbf{r}) f(n(\mathbf{r}), \nabla n(\mathbf{r})) dr\,, \tag{2.36}$$

where f is some function. The GGA are semilocal approximations in the sense that f does not only use the local value of the density $n(\mathbf{r})$ but also its gradient $\nabla n(\mathbf{r})$. For simplicity, we consider here only the spin-independent form, but in practice GGA functionals are more generally formulated in terms of spin densities $(n_\uparrow, n_\downarrow)$ and their gradients $(\nabla n_\uparrow, \nabla n_\downarrow)$.

Many GGA functionals have been proposed. We very briefly review here some of the most widely used ones.

B88 exchange functional

The Becke 88 (B88 or B) [21] exchange functional is formulated as an additive correction to LDA. It consists in a compact function of $n(\mathbf{r})$ and $|\nabla n(\mathbf{r})|/n(\mathbf{r})^{4/3}$ chosen to satisfy the exact asymptotic behavior of the exchange energy per particle, and with an empirical parameter fitted to Hartree-Fock exchange energies of rare-gas atoms.

LYP correlation functional

The Lee-Yang-Parr (LYP) [22] correlation functional is one of the rare functionals which have not been constructed starting from the LDA. It originates from the Colle-Salvetti [23] correlation-energy approximation depending on the Hartree-Fock pair density and containing four parameters fitted to helium data. By making a further reasonable approximation, LYP turned the Colle-Salvetti expression into a density functional depending on the density $n(\mathbf{r})$, the square of the density gradient $|\nabla n(\mathbf{r})|^2$, and the Laplacian of the density $\nabla^2 n(\mathbf{r})$. The dependence on the Laplacian can be exactly eliminated by an integration by parts [24].

PBE exchange-correlation functional

For the Perdew-Burke-Ernzerhof functional (PBE) [25], the exchange and correlation energies per particle are expressed as simpler functions of $n(\mathbf{r})$ and $|\nabla n(\mathbf{r})|$ enforcing less exact conditions and with no fitted parameters. Specifically, the function used for correlation enforces the second-order small-gradient expansion in the high-density limit, the vanishing of correlation in the large-gradient limit, and the removal of the logarithm divergence of the LDA in the high-density limit (see Equation 2.32). The function used for exchange is chosen to cancel out the second-order small-gradient expansion of correlation and to enforce the Lieb-Oxford bound in the large-gradient limit.

2.2.3 Meta-generalized gradient approximations

The meta-generalized-gradient approximations (meta-GGA or mGGA) are of the generic form,

$$E_{\rm xc}^{\rm mGGA} = \int n(\mathbf{r}) f(n(\mathbf{r}), \nabla n(\mathbf{r}), \nabla^2 n(\mathbf{r}), \tau(\mathbf{r})) dr\,. \tag{2.37}$$

They use more ingredients than the GGAs, namely the Laplacian of the density $\nabla^2 n(\mathbf{r})$ and the non-interacting kinetic energy density $\tau(\mathbf{r})$:

$$\tau(\mathbf{r}) = \frac{1}{2}\sum_{i=1}^{N} |\psi_i(\mathbf{r})|^2\,, \tag{2.38}$$

where $\psi_i(\mathbf{r})$ are the KS orbitals. Note that meta-GGAs are only implicit functionals of the density since $\tau(\mathbf{r})$ is itself an implicit functional of the density through the orbitals. This tacitly implies an extension of the usual KS method. The meta-GGAs are considered part of the family of semilocal approximations, in the sense that $\tau(\mathbf{r})$ depends only the gradient of the orbitals. Again, we consider here only the spin-independent form, but meta-GGA are more generally formulated in terms of spin-resolved quantities $(n_\uparrow, n_\downarrow, \nabla n_\uparrow, \nabla n_\downarrow, \nabla^2 n_\uparrow, \nabla^2 n_\downarrow, \tau_\uparrow, \tau_\downarrow)$.

One motivation for the introduction of the variable $\tau(\mathbf{r})$ is that it appears in the short-range expansion of the exchange hole [26], which for the case of a closed-shell system is

$$n_{\rm x}(\mathbf{r}, \mathbf{r}') = -\frac{n(\mathbf{r})}{2} - \frac{1}{3}\left[\nabla^2 n(\mathbf{r}) - 4\tau(\mathbf{r}) + \frac{|\nabla n(\mathbf{r})|^2}{2n(\mathbf{r})}\right]|r - r'|^2 + \ldots\,. \tag{2.39}$$

Another important motivation is that $\tau(\mathbf{r})$ can be use to make the correlation energy per particle correctly vanish in spatial regions where the density has a one-electron character. This is done by comparing $\tau(\mathbf{r})$ with the von Weizsäcker kinetic energy density

$$\tau^{\rm W}(\mathbf{r}) = \frac{|\nabla n(\mathbf{r})|^2}{8n(\mathbf{r})}\,. \tag{2.40}$$

Which is exact for one-electron systems, e.g. by introducing the ratio $\tau(\mathbf{r})/\tau^W(\mathbf{r})$.

One the most used meta-GGA approximation is the Tao-Perdew-Staroverov-Scuseria (TPSS) [27] exchange-correlation functional.

2.2.4 Hybrid approximations

Based on arguments relying on the adiabatic-connection formalism, in 1993 Becke [28] proposed to mix a fraction of the exact or Hartree-Fock (HF) exchange energy with GGA

functionals. In particular, he proposed a three-parameter hybrid (3H) approximation [29] of the form

$$E_{\mathrm{xc}}^{\mathrm{3H}} = aE_{\mathrm{x}}^{\mathrm{HF}} + bE_{\mathrm{x}}^{\mathrm{GGA}} + (1-a-b)E_{\mathrm{x}}^{\mathrm{LDA}} + cE_{\mathrm{c}}^{\mathrm{GGA}} + (1-c)E_{\mathrm{c}}^{\mathrm{LDA}}\,, \tag{2.41}$$

where the three parameters a, b, and c are determined by fitting to experimental data. Note that $E_{\mathrm{x}}^{\mathrm{HF}}$ depends on the occupied orbitals and has the exact-exchange expression:

$$E_{\mathrm{x}}^{\mathrm{HF}} = -\frac{1}{2}\sum_{i=1}^{N}\sum_{j=1}^{N}\int\int \frac{\psi_i^*(\mathbf{r_1})\psi_j(\mathbf{r_1})\psi_j^*(\mathbf{r_2})\psi_i(\mathbf{r_2})}{|\mathbf{r_1}-\mathbf{r_2}|}dr_1 dr_2\,. \tag{2.42}$$

This constitutes an extension of the usual KS method, sometimes referred to as generalized Kohn-Sham [30]. The main benefit of adding a fraction of HF exchange is to decrease the self-interaction error in the exchange functional which tends to favor delocalized electron densities over localized electron densities. The most famous and widely used three-parameter hybrid approximation is B3LYP [31], which uses the B88 exchange functional and the LYP correlation functional, and the parameters a = 0.20, b = 0.72, and c = 0.81.

In 1996, Becke proposed a simpler one-parameter hybrid (1H) approximation [32]

$$E_{\mathrm{xc}}^{\mathrm{1H}} = aE_{\mathrm{x}}^{\mathrm{HF}} + (1-a)E_{\mathrm{x}}^{\mathrm{DFA}} + E_{\mathrm{c}}^{\mathrm{DFA}}\,, \tag{2.43}$$

where $E_{\mathrm{x}}^{\mathrm{DFA}}$ and $E_{\mathrm{c}}^{\mathrm{DFA}}$ can be any (semilocal) density-functional approximation (DFA), and the fraction a of HF exchange has to be determined. The fraction of HF exchange should be small enough to keep the compensation of errors usually occurring between the approximate semilocal exchange functional $E_{\mathrm{x}}^{\mathrm{DFA}}$ and the approximate semilocal correlation functional $E_{\mathrm{c}}^{\mathrm{DFA}}$. Fits to experimental data often give an optimal parameter a around 0.25. A rationale has also been proposed in favor of this value [33]. For example, PBE0 [34, 35] is a popular one-parameter hybrid approximation which uses a = 0.25 and the PBE exchange and correlation functionals.

A strategy that has been sometimes used to construct approximations of the form of Equation 2.43 is to employ parameterized flexible functions for $E_{\mathrm{x}}^{\mathrm{DFA}}$ and $E_{\mathrm{c}}^{\mathrm{DFA}}$ and systematically optimize all the parameters (including the fraction a of HF exchange) on large sets of physicochemical properties of molecular systems. For example, the Becke 97 (B97) exchange-correlation functional [36] is a hybrid GGA approximation containing 13 parameters optimized on atomic exchange and correlation energies, atomization energies, ionization potentials, and proton affinities. Another example is the so-called family of "Minnesota" functionals, and in particular the M06 exchange-correlation functional [37] which is a hybrid meta-GGA approximation containing 36 parameters optimized on a very large set of diverse

physicochemical properties concerning main-group thermochemistry, reaction barrier heights, noncovalent interactions, electronic spectroscopy, and transition metal bonding.

2.2.5 Double-hybrid approximations

In 2006, Grimme [38] introduced a two-parameter double-hybrid (2DH) approximation

$$E_{\mathrm{xc}}^{\mathrm{2DH}} = a_{\mathrm{x}} E_{\mathrm{x}}^{\mathrm{HF}} + (1-a_{\mathrm{x}}) E_{\mathrm{x}}^{\mathrm{DFA}} + (1-a_{\mathrm{c}}) E_{\mathrm{c}}^{\mathrm{DFA}} + a_{\mathrm{c}} E_{\mathrm{c}}^{\mathrm{MP2}}\,, \tag{2.44}$$

mixing a fraction a_x of the HF exchange energy with a semilocal exchange DFA, and a fraction a_c of the second-order Møller-Plesset (MP2) correlation energy $E_{\mathrm{c}}^{\mathrm{MP2}}$ with a semilocal correlation DFA. In equation (2.44), the first three terms are first calculated in a self-consistent manner, and then the last term $E_{\mathrm{c}}^{\mathrm{MP2}}$ is added perturbatively using the orbitals determined in the first step. The expression of $E_{\mathrm{c}}^{\mathrm{MP2}}$ is

$$E_{\mathrm{c}}^{\mathrm{MP2}} = -\frac{1}{4} \sum_{i=1}^{N} \sum_{j=1}^{N} \sum_{a \geq N+1} \sum_{b \geq N+1} \frac{|(ia|jb) - (ib|ja)|^2}{\varepsilon_a - \varepsilon_b - \varepsilon_i - \varepsilon_j}\,, \tag{2.45}$$

where $(ia|jb)$ are two-electron integrals, ε are orbital energies, and i, j and a, b run over occupied and virtual spin orbitals, respectively. The presence of nonlocal MP2 correlation allows one to use a larger fraction of nonlocal HF exchange. For example, Grimme proposed the B2-PLYP approximation which uses the B88 exchange and LYP correlation functionals, and the parameters $a_x = 0.53$ and $a_c = 0.27$ optimized on experimental heats of formation of a set of molecules.

In 2011, Sharkas, Toulouse, and Savin [39] showed how the double-hybrid approximations can be rigorously reformulated using the adiabatic-connection formalism, which leads to a one-parameter double-hybrid (1DH) approximation

$$E_{\mathrm{xc}}^{\mathrm{1DH}} = \lambda E_{\mathrm{x}}^{\mathrm{HF}} + (1-\lambda) E_{\mathrm{x}}^{\mathrm{DFA}} + (1-\lambda^2) E_{\mathrm{c}}^{\mathrm{DFA}} + \lambda^2 E_{\mathrm{c}}^{\mathrm{MP2}}\,, \tag{2.46}$$

where the fraction HF exchange $a_x = \lambda$ is now connected to the fraction of MP2 correlation $a_c = \lambda^2$. It turns out that using $a_x = \lambda = 0.53$ nearly reproduces the parameter $a_c = \lambda^2 = 0.28 \simeq 0.27$ independently optimized in B2-PLYP.

The double-hybrid approximations are examples of correlation functionals depending on virtual orbitals. Another example of a correlation functional depending on virtual orbitals is the random-phase approximation (RPA), which goes beyond second order and has been the subject of intensive developments since the 2000s.

2.2.6 Range-separated hybrid approximations

Based on earlier ideas of Savin [40] in 2001, Iikura, Tsuneda, Yanai, and Hirao [41] proposed a long-range correction (LC) scheme

$$E_{\mathrm{xc}}^{\mathrm{LC}} = E_{\mathrm{x}}^{\mathrm{lr,HF}} + E_{\mathrm{x}}^{\mathrm{sr,DFA}} + E_{\mathrm{c}}^{\mathrm{DFA}}, \tag{2.47}$$

where $E_{\mathrm{x}}^{\mathrm{lr,HF}}$ is the HF exchange energy for a long-range electron-electron interaction

$$E_{\mathrm{x}}^{\mathrm{lr,HF}} = -\frac{1}{2}\sum_{i=1}^{N}\sum_{j=1}^{N}\int\int \phi_i^*(\mathbf{r_1})\phi_j(\mathbf{r_2})\phi_j^*(\mathbf{r_2})\phi_i(\mathbf{r_1})\omega_{ee}^{lr}dr_1dr_2\,, \tag{2.48}$$

where $\omega_{ee}^{lr} = erf(\mu r_{12})/r_{12}$ where $r_{12} = |r_1 - r_2|$ is the inter-electronic distance and erf is the error function

$$erf(x) = \frac{2}{\sqrt{\pi}}\int_0^x e^{-t^2}dt\,, \tag{2.49}$$

and $E_{\mathrm{x}}^{\mathrm{sr,DFA}}$ is the DFA exchange energy for the complementary short-range interaction. In addition, the short-range exchange part is easier to approximate with a semilocal DFA. The parameter μ in the error function controls the range of the separation and must be chosen, e.g. by fitting to experimental data. In practice, a value around $\mu \simeq 0.3$ - 0.5 bohr^{-1} is often found to be optimal. A popular example of such LC approximations is LC-ω PBE [42] which uses a short-range version of the PBE exchange functional, as well as the standard PBE correlation functional. Note that the LC scheme has also been referred to as the range-separated hybrid exchange (RSHX) scheme [43].

In 2004, Yanai, Tew, and Handy [44], introduced a more flexible scheme called the Coulomb-attenuating method (CAM) [44] in which fractions of HF exchange are added at both short and long range

$$E_{\mathrm{xc}}^{\mathrm{CAM}} = aE_{\mathrm{x}}^{\mathrm{sr,HF}} + bE_{\mathrm{x}}^{\mathrm{lr,HF}} + (1-a)E_{\mathrm{x}}^{\mathrm{sr,DFA}} + (1-b)E_{\mathrm{x}}^{\mathrm{lr,DFA}} + E_{\mathrm{c}}^{\mathrm{DFA}}, \tag{2.50}$$

where $E_{\mathrm{x}}^{\mathrm{sr,HF}}$ is the HF exchange energy for the short-range interaction and $E_{\mathrm{x}}^{\mathrm{lr,HF}}$ is the DFA exchange energy for the long-range interaction. The reintroduction of HF exchange at short range improves thermodynamic properties such as atomization energies. According to this scheme, the authors proposed the CAM-B3LYP approximation which uses short- and long-range versions of the B88 exchange functional, the same correlation functional used in B3LYP (i.e., 0.81 $E_c^{\mathrm{LYP}} + 0.19E_c^{\mathrm{LDA}}$), and optimized parameters $a = 0.19$, $b = 0.65$, and $\mu = 0.334$ bohr^{-1}. Another example in this class of approximations is the ωB97X exchange-

correlation functional [45] which is based on the B97 exchange-correlation functional with reoptimized parameters, and uses $a = 0.16$, $b = 1$, and $\mu = 0.3$ bohr^{-1}. Another functional that can be considered as part of this class of approximations is the Heyd-Scuseria-Ernzerhof (HSE) exchange-correlation functional [46], which uses the parameters $a = 0.25, b = 0$ (i.e. no long-range HF exchange), and $\mu = 0.15$ bohr^{-1}, with a long-range version of the PBE exchange correlation functional and the standard PBE correlation functional. The absence of HF exchange at long range makes this approximation particularly useful for solids.

2.3 Structural prediction algorithms

The crystal structure occupies a central and often critical role in material science, particularly when establishing a correspondence between material performance and its basic composition, since the properties of a material are intimately tied to its crystal structure. Experimentally, the structure is determined by x-ray diffraction. It has solved numerous problems of crystal structure. However, only a small faction of systems have been studied experimentally, especially at high pressure. Therefore, it is often useful to be able to predict the crystal structure with theoretical techniques. There are two main different ways to predict the structure of a material. They are high-throughput methods and global crystal structure prediction methods. It is well known that nature often chooses the same solution to similar problems. Therefore, one can take a known, experimentally characterized structure, change its chemical composition, and hope that this will be also a stable phase for a new composition. This is the main idea of high-throughput methods. This method was already used successfully for many systems, such as delafossites, perovskites and clathrates. Higher success rates can be achieved by using sophisticated machine learning algorithms, which can help to choose the most likely substitutions. This approach is currently widely used with very good results, and applications to several areas have already been published [47–50]. However, as it relies heavily on experimental data, it fails to find compounds that are very different from what is already known. In this case, the global structure prediction methods that only use the chemical composition are possible. However, these methods are rather complex as they basically involve classifying a huge number of energy minima on the potential energy surface. About 20 years ago John Maddox even published an article in Nature to question the predictive power provided with only the knowledge of chemical composition [51]. His words still remain largely true, as evidenced by poor results of the latest blind test for crystal structure prediction [52]. Owing to significant progress in both computational power and basic material theory, it is now possible to predict the crystal structure using standard methods based on DFT and beyond. Some of these are simulated annealing [53], genetic

algorithms [54–58], basin hopping [59, 60], metadynamics [61, 62], random sampling [63–65], data mining [66], particle-swarm optimization [67, 68] and minima hoping [69, 70]. In the next paragraph we will discuss the two main algorithms that were used in this thesis: particle-swarm optimization (CALYPSO) and minima hoping method (MHM).

2.3.1 Particle swarm optimization

Particle-swarm optimization was first proposed by Kennedy and Eberhart in the mid 1900s [71, 72]. As a stochastic global optimization method, particle-swarm optimization is inspired by the choreography of a bird flock and can be seen as a distributed behavior algorithm that performs multidimensional search. According to the particle-swarm optimization, the behavior of each individual is affected by either the best local or the best global individual to help it fly through a hyperspace. Moreover, an individual can learn from its part experiences to adjust its flying speed and direction. Therefore, all the individuals in the swarm can quickly converge to the global position and near-optimal geographical position by the behavior of the flock and their flying histories. Particle-swarm optimization (PSO) has been verified to perform well on many optimization problems. Y. Ma and Y. Wang implemented PSO algorithm for crystal structure prediction in the crystal structure analysis by particle swarm optimization CALYPSO code [67, 68]. In this algorithm, a structure (an individual) in the searching phase space is viewed as a particle $x^t_{i,j}$. A set of individual particles is called a population or a generation. During the generation of particles, the new particle, $x^{t'}_{i,j}$, depends on its previous position, $x^t_{i,j}$, and its velocity, $v^{t'}_{i,j}$, as $x^{t'}_{i,j} = x^t_{i,j} + v^{t'}_{i,j}$. It is necessary to note that the velocity plays an important role on the determination of the speed and direction of the particle movement. The new velocity of each individual i at the jth dimension is calculated based on its previous location ($x^t_{i,j}$) before optimization, previous velocity $v^t_{i,j}$, current location $pbest^t_{i,j}$ with an achieved best fitness, i.e., lowest enthalpy, of this individual, and the population global location $gbest^t_{i,j}$ with the best fitness value for the entire population according to equation 2.51

$$v^{t'}_{i,j} = \omega v^t_{i,j} + c_1 r_1 (pbest^t_{i,j} - x^t_{i,j}) + c_2 r_2 (gbest^t_{i,j} - x^t_{i,j}), \tag{2.51}$$

where j $\in (1,2,3)$, ω (in the range of 0.9–0.4) denotes the inertia weight and controls the momentum of the particle. c_1 is a self-confidence factor and expresses how much the particle trusts its own past experience while c_2 is a swarm confidence factor and expresses how much it trusts the swarm. r_1 and r_2 are two separately generated random numbers and uniformly distributed in the range [0, 1]. The velocity update formula includes random parameters r_1 and r_2 to ensure good coverage of the searching space and avoid entrapment in local

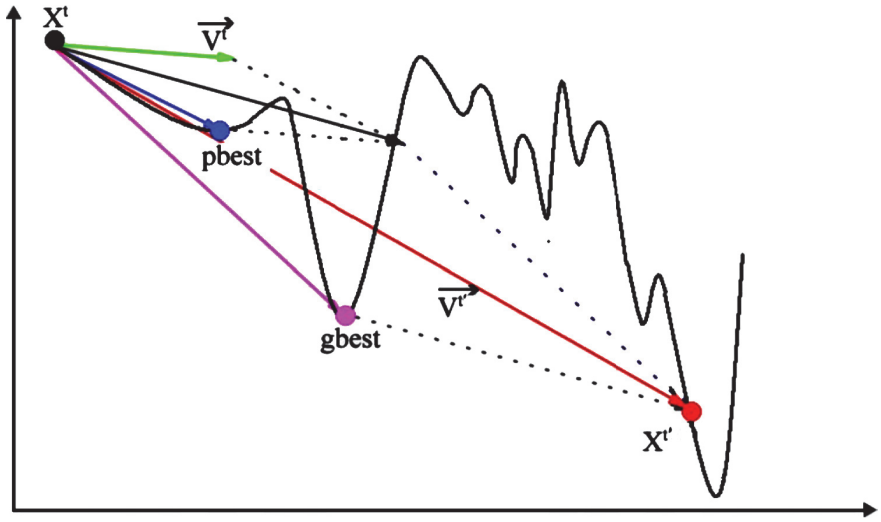

Figure 2.1 Depiction of the velocity and position updates in PSO. The black solid line approximates a typical energy landscape. Arrows represent either the velocity at the relative positions of particle (here represent a structure). An initial velocity v^t develops to $v^{t'}$ after one PSO step through Eq. 2.51.

optima. As shown in equation 2.51, it is quite obvious that the movement of particles in the search space is dynamically influenced by their individual past experience ($pbest^t_{i,j}$, $v^t_{i,j}$) and successful experiences attained by the whole swarm $gbest^t_{i,j}$. Thus the velocity makes the particles to move toward to global minimum and accelerates the convergence speed. The possible potential energy face of each particle can be shown in Fig. 2.1.

2.3.2 Minima hopping method

The Minima Hopping Method, developed by S. Gödecker and M. Amsler [69, 70], is a structural prediction algorithm that tries to find the global minimum of a potential energy surface by jumping between local minima using short molecular dynamics (MD) runs (solid arrows in Fig. 2.2), followed by local geometry optimizations at each minima (dashed arrows). An energy based acceptance criteria assures that each new minimum has a 50% chance of being accepted (δE in the figure). This means that every time a new minimum is found, the acceptance criterion is adjusted to guarantee that, on average, half of the local minima are accepted. In order to avoid revisiting already explored minima, the temperature of the MD runs is adjusted dynamically during the search. This is done to allow escaping local minima surrounded by high energy barriers. A *softening* process is used to accelerate the minimization problem as it is expected that (on average) crossing low energy barriers will lead to lower energy minima [73]. Hence, the MD velocities should be aligned along

directions of low curvature – soft modes. In practice, as a perfect alignment would eliminate the random character of the escape step, these directions are chosen only to avoid hard mode directions.

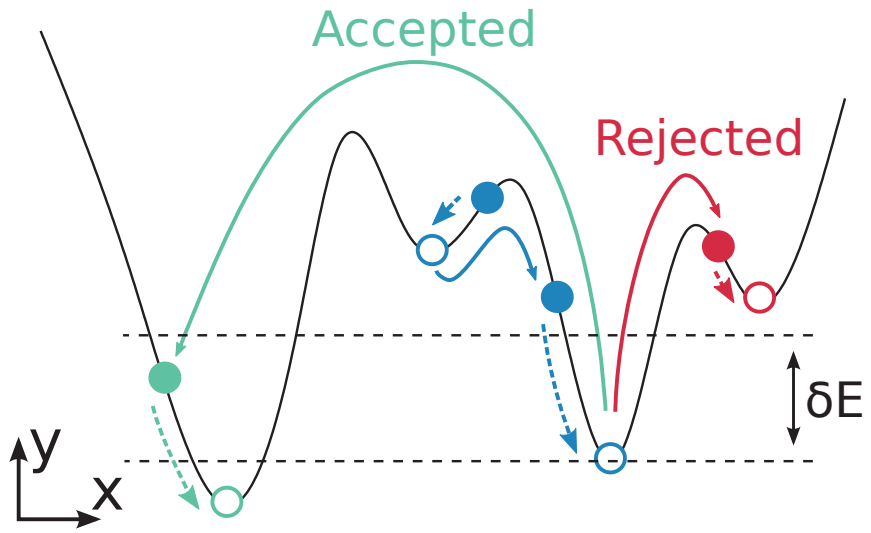

Figure 2.2 Hypothetical potential energy surface for minima hopping method. The x axis represents some internal degree of freedom, while y is the energy for a given configuration.

This method is able to optimize both cell vectors and atomic positions, being the only constraints the stoichiometry and the number of unit cells. In our runs, we start always from a random structure, assuring only that the minimum distance between atoms is at least equal to the sum of their covalent radii.

The minima hopping method has been used for structural prediction in a wide range of materials [74–77], including the dependence on pressure [78] and the exploration of binary phase diagrams [1, 79] with remarkable results.

2.4 Structural stability

How can we determine a new structure is thermodynamically stable? Here we discuss this common problem. As we know, even for a simple system there are also lots of possible compositions. However most of them are not thermodynamically stable. In order to determine if a structure is thermodynamically stable, let us consider a system at zero temperature. We should compare the formation enthalpy of the new compound with all the possible decomposition channels through Eq. 2.52,

$$\Delta H|_P \equiv H(\mathrm{A}_y\mathrm{B}_{1-y}) - yH(\mathrm{A}) - (1-y)H(\mathrm{B})\,. \tag{2.52}$$

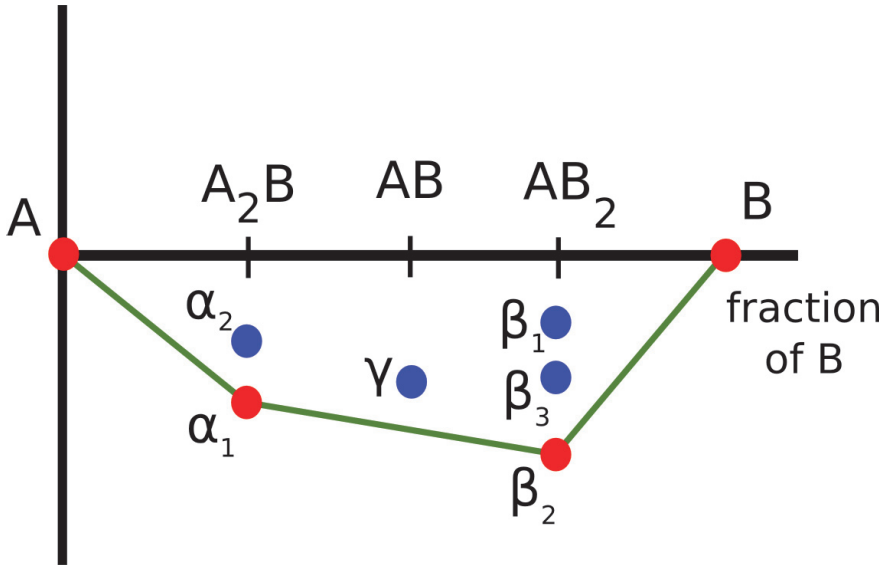

Figure 2.3 An example of convexhull

The distance to the convex hull is the measure of the energy released by decomposing into the stable phases. The structures that are above the convex hull are thermodynamic unstable, while the structures that on the convex hull are thermodynamic stable and may be synthesized experimentally. Fig. 5.2 shows a convex hull (in green) for a A-B binary system. Blue points indicate phases that are not on the hull and therefore unstable and red points indicate stable phases. For instance, the construction shows directly that the phase γ at AB will decompose into α_1 and β_2.

Another important aspect to take in account is the mechanically stability. When we predict a new structure that is thermodynamically stable, we should calculate the phonon spectrum of this new structure to insure that it is mechanically stable. If there are no imaginary phonon frequencies we can say this structure is stable, otherwise this structure is not stable even though it is thermodynamically stable. In this case it is means we did not find the ground state structure for this system.

Chapter 3

New phases of Ba-Si system under high pressure

3.1 Introduction

Alkali-earth silicides are extremely versatile materials, capable of crystallizing in a large variety of structures. For example, $BaSi_2$, perhaps the most studied member of this family, exhibits four different phases at ambient conditions, [80] namely an orthorhombic (*Pnma*), cubic ($P4_332$), trigonal ($P\bar{3}m1$), and hexagonal ($P6/mmm$) phase [81–84]. This rich structural diversity naturally leads to a wealth of interesting physical properties. The orthorhombic and cubic phases are semiconductors [85, 86] with a suitable band-gap for photovoltaic applications [87] and a large absorption coefficient [88]. On the other hand, the trigonal phase is metallic, and becomes superconducting at low temperatures [4, 89–91]. It is interesting to note that this trigonal phase is composed of corrugated planes of silicon intercalated by barium atoms, and can be viewed as the silicene counterpart of intercalated graphite. It is also worth mentioning that alkali-earth disilicides are also used as percursors for the synthesis of silicon clathrates [92, 93]. At ambient pressure there is still another stable composition in the Ba–Si phase diagram, namely BaSi [80, 94], that crystallizes in a metallic CrB-type phase (*Cmcm*).

Unfortunately, at high-pressures there is relatively little experimental and theoretical work performed on this phase diagram. The composition $BaSi_6$, has been synthesized at around 15 GPa [95], but nothing else is known about this system. Moreover, it is by now well known that high pressure can change dramatically the chemistry of even the simplest elements [96], leading to the stabilization of diverse, and often unexpected compositions [97, 98].

The objective of this work is therefore to perform a systematic theoretical study of the high-pressure Ba–Si phase diagram, especially in the silicon rich region. We will concentrate on the pressure range from 0 to 150 GPa as these pressures can nowadays be easily reached in diamond anvil cells. This will be done through an unbiased structural search based on a particle-swarm optimization Algorithm [67, 68] (see Chapter 2) and a first principles density-functional approach to evaluate total energies and forces. The effectiveness of this method has already been demonstrated by several predictions under high pressure [99–107]. We remark that a surprising structural richness has recently been revealed using the same structural search algorithm in the Ca–Si phase diagram [108].

3.2 Methods

We investigated the stoichiometries $BaSi_x$ (x=1, 2, 3, 4, 5, 6), using cells containing 2, 4, 6, and 8 formula units in a pressure range from 0 to 150 GPa. Ground-state structures were obtained using the CALYPSO (Crystal structure AnaLYsis by Particle Swarm Optimization) global structure prediction code [67, 68]. Total energies and forces were calculated with an ab initio density functional approach [14] within the Perdew-Burke-Ernzenhof [25] generalized gradient approximation as implemented in the VASP code [109]. We adopted the all-electron projector-augmented wave method [110] using the valence configurations $5s^2 5p^6 6s^2$ (for Ba) and $3s^2 3p^2$ (for Si). We used a cutoff energy of 600 eV and uniform Monkhorst-Pack k-meshes [111]. The convergence of all ab initio calculations was ensured to better than 1 meV/atom. The phonon density of states was calculated using a finite displacement method [112] as implemented in the PHONOPY package [113]. Electron-phonon coupling (EPC) calculations were carried out with density function perturbation theory using the program Quantum ESPRESSO [114] with a cutoff of 80 Ry, A $12 \times 12 \times 12$ q-point mesh, and a Gaussian smearing of 0.05 Ry. We note that all calculations were performed at 0 K neglecting the zero-point correction to the energy, that in any case is expected to be small for our systems.

3.3 Results and discussion

We investigated the energetic stability of the Ba-Si system by studying the enthalpy of formation for different $BaSi_x$ compounds with pressures from 0 to 150 GPa. The formation enthalpy H of Ba_ySi_{1-y} ($0 < y < 1$) is defined as

$$\Delta H|_P \equiv H(\mathrm{Ba}_y\mathrm{Si}_{1-y}) - yH(\mathrm{Ba}) - (1-y)H(\mathrm{Si}), \tag{3.1}$$

where $H(\mathrm{Ba})$ and $H(\mathrm{Si})$ represent the enthalpy of formation of bulk Ba and Si. For Ba, We used the $Im\bar{3}m$ [115] and $P6_3/mmc$ [116] structures under ambient pressure and high pressure, respectively, while for pure Si we used the $Fd\bar{3}m$ phase at ambient pressure, the Si-VI ($Cmca$) [117] phase at 20 GPa, the Si-VII ($P6_3/mmc$) [118] and Si-X ($Fm\bar{3}m$) [119] phases at high pressure. The enthalpy of formation ΔH, and the respective convex hull of thermodynamic stability, is depicted in Fig. 3.1 for pressures of 0, 5, 20, 50, 100, and 150 GPa.

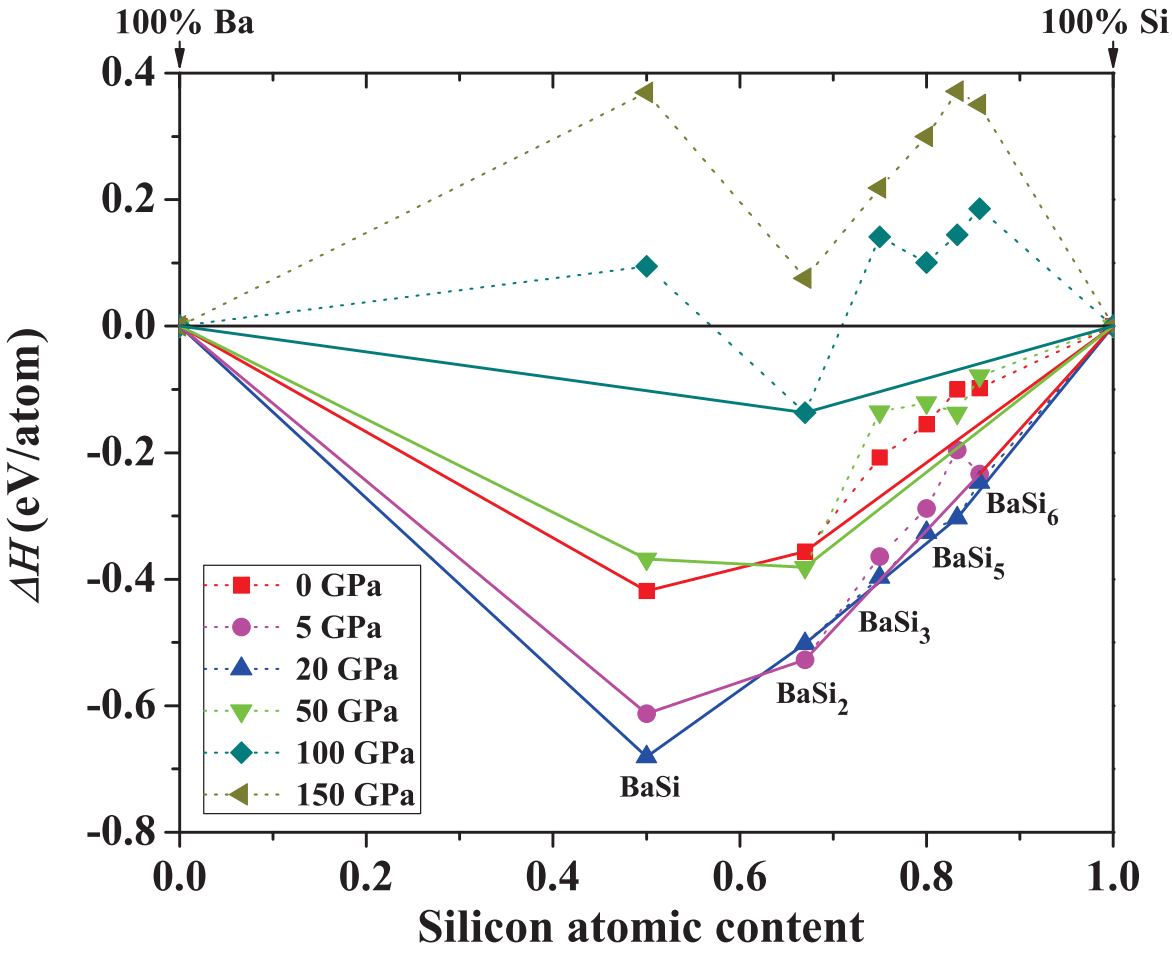

Figure 3.1 Calculated enthalpy of formation (ΔH in eV/atom) of various Ba–Si compounds with respect to the elemental decomposition into bulk Ba and Si at 0, 5, 20, 50, 100, and 150 GPa. The solid lines represent the convex hulls, while the dotted lines are just a guide for the eyes.

From the convex hulls in Fig. 3.1 we can see that all Ba-Si compounds were found to have a negative formation enthalpy at ambient pressure. Both BaSi and $BaSi_2$ are thermodynamically stable, in good agreement with experimental results [80–84], with the former being the most stable composition. The situation, however, becomes quite complex when we increase

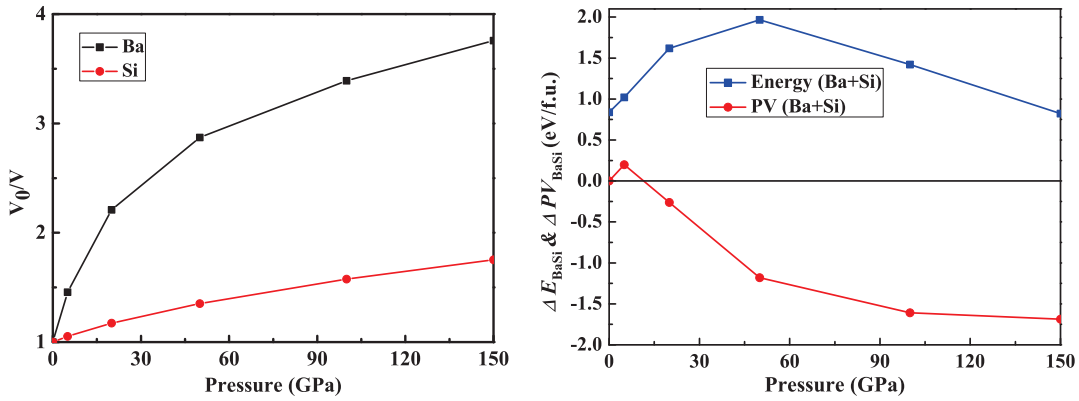

Figure 3.2 (a) Compressibility, V0/V, for Ba and Si. (b) Ground-state energy and PV components of the enthalpy of the elements relative to BaSi.

the pressure. At 5 GPa, also $BaSi_6$ becomes thermodynamically stable, again in agreement with experiment [95]. At 20 GPa, however, the formation enthalpy of $BaSi_5$ decreases, and it becomes thermodynamically stable, thereby destabilizing $BaSi_6$. At this pressure, also $BaSi_3$ has a phase that is extremely close to the convex hull. As the pressure is further increased to 50 GPa, all these compositions with high silicon content become thermodynamically unstable. At 100 GPa BaSi also becomes unstable, and finally, at 150 GPa we do not find any stable binary compound in the Ba–Si system. The same behavior was observed for Ca–Si binaries at pressure above 250 GPa [108]. The explanation given in Ref. [108] is that while both energy and *PV* contributions to the enthalpy favor compound formation at moderate pressures, the ΔPV term quickly grows negative and dominates enthalpy variations at high pressure. The higher compressibility of Ca with respect to Si and Ca–Si binaries is at the origin of the phase separation at higher pressure. A similar explanation applies also to our Ba–Si phase diagram, as a consequence of the higher compressibility of Ba. It can be easily found from Fig. 3.2. The structural parameters of our predicted stable structures for Ba-Si compounds at their corresponding pressures are shown in Tab. 3.1.

The phase transitions of BaSi under pressure are further illustrated in Fig. 3.3, where we plot the relative enthalpies per formula unit with respect to the *Cmcm* structure (that is the ground-state at ambient conditions), including the enthalpy of the most likely decomposition channel.

In the following we give a more detailed analysis of the new stable structures found during our structural prediction runs. The structures are shown in Fig. 3.4. We calculated phonon spectra, which confirmed the dynamical stability of all the new phases. Finally, we determined the electronic character (semiconducting or metallic) by inspection of their electronic density of states.

Table 3.1 Calculated structural parameters of our predicted stable structures for Ba-Si compounds at their corresponding pressures

Space group Pressure	Lattice parameters	Atomic coordinates (fractional)
Imma-BaSi 20 GPa	a=3.67280 Å b=5.08260 Å c=9.43680 Å α=β=γ=90°	Ba(4e) 0.50000 0.25000 0.39804 Si(4e) 0.50000 -0.25000 0.17580
$Fd\bar{3}m$-$BaSi_2$ 50 GPa	a=7.18670 Å b=7.18670 Å c=7.18670 Å α=β=γ=90°	Ba(8a) 0.25000 0.25000 0.25000 Si(16d) 0.62500 0.12500 0.12500
$I4/mmm$-$BaSi_3$ 20 GPa	a=6.84750 Å b=6.84750 Å c=12.17490 Å α=β=γ=90°	Ba1(4e) 0.50000 0.50000 0.31654 Ba5(4d) 0.00000 0.50000 0.25000 Si1(16m) 0.68117 0.31883 0.09624 Si17(8i) 0.66915 0.00000 0.00000
Cmmm-$BaSi_5$ 20 GPa	a=4.2121 Å b=7.2510 Å c=6.3456 Å α=β=γ=90°	Ba1(2c) 0.00000 0.50000 0.50000 Si1(8n) -0.00000 0.83323 0.81577 Si9(2b) 0.00000 0.50000 -0.00000

3.3.1 BaSi

We now focus on Fig. 3.1 and Fig. 3.3 to discuss the stability of BaSi under pressure. We can see that the BaSi composition is stable in a large range of pressures, from ambient pressure to more than 65 GPa, after which the decomposition into Ba and $BaSi_2$ becomes energetically favorable. At ambient pressure, our structural prediction algorithm obtains a ground-state structure with *Cmcm* symmetry. This is the phase already known experimentally, in which Ba atoms form distorted hexagonal structures with one-dimensional channels that are filled with zigzag chains of Si atoms [80, 94]. However, this phase is quickly destabilized by pressure, and a novel structure with space group *Imma* becomes the ground-state at pressures of around 6 GPa.

The new predicted *Imma* phase of BaSi is shown in Fig. 3.4 (a). Its primitive cell has two Ba atoms and two Si atoms. There are striking similarities between this structure and the low-pressure *Cmcm* phase. Both phases contain one-dimensional hexagonal channels formed by Ba atoms, but now the hexagons are regular due to a rearrangement of the Ba-atoms. The Si chains have the same arrangement in both cases. The distance between the two

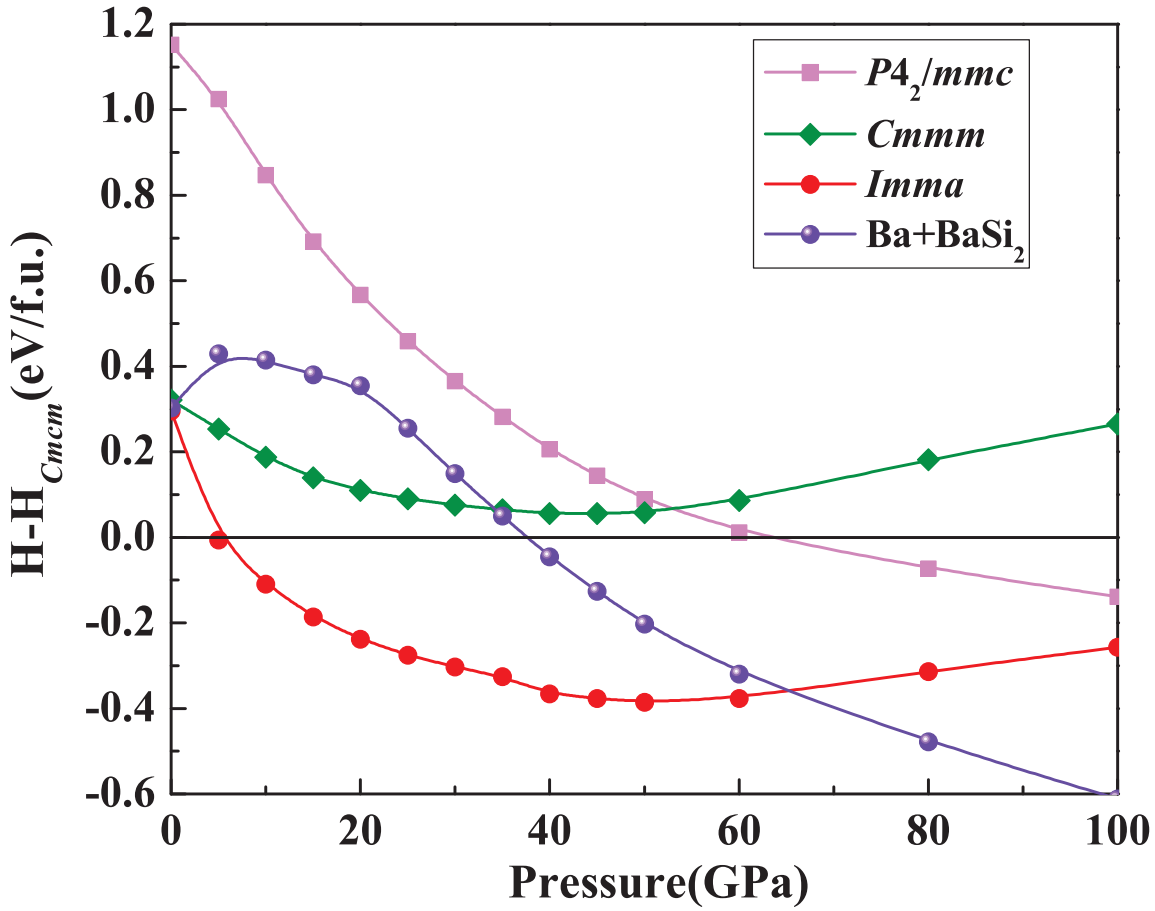

Figure 3.3 Relative enthalpy per formula unit of the different phases of BaSi with respect to the *Cmcm* phase [80, 94] as a function of pressure. The *Imma* phase is a new structure predicted in this work. We also plot the enthalpy of the most likely decomposition channel into Ba and $BaSi_2$. Note that the green line with diamonds refers to a different, meta-stable *Cmcm* phase and not to the ground-state *Cmcm* phase at low-pressures.

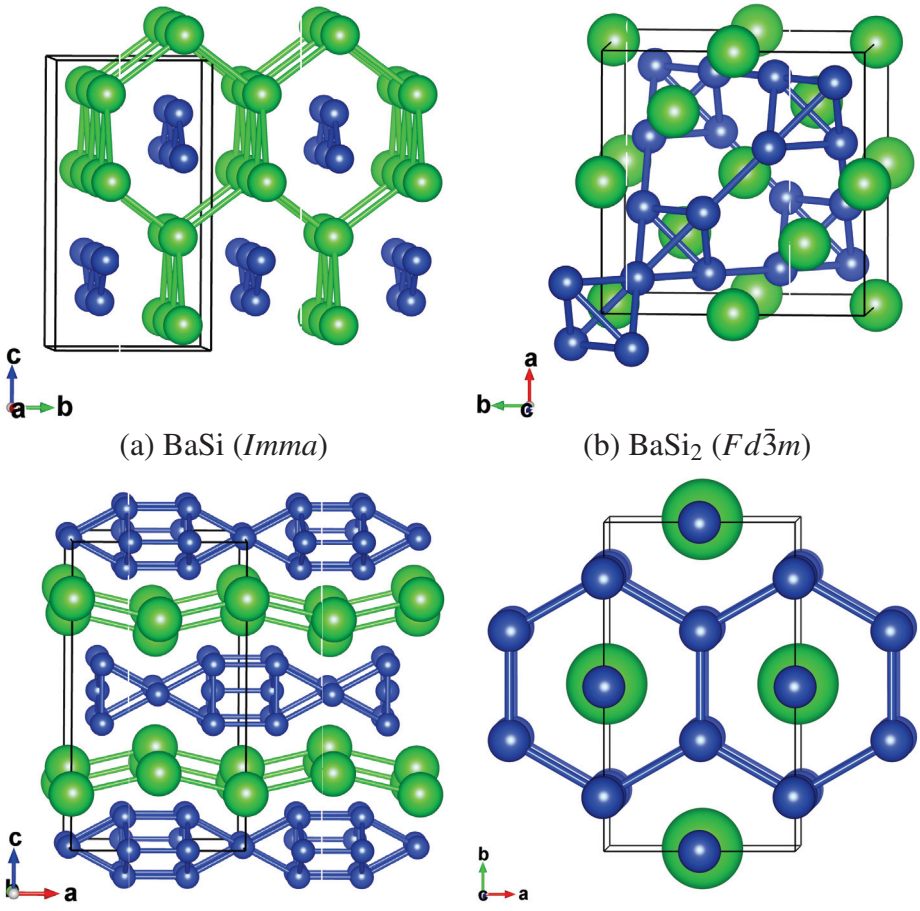

(a) BaSi (*Imma*) (b) $BaSi_2$ ($Fd\bar{3}m$)

(c) $BaSi_3$ ($I4/mmm$) (d) $BaSi_5$ (*Cmmm*)

Figure 3.4 Structures predicted in Ba–Si system: (a) *Imma* phase of BaSi; (b) $Fd\bar{3}m$ phase of $BaSi_2$; (c) $I4/mmm$ phase of $BaSi_3$; and (d) *Cmmm* phase of $BaSi_5$. The green and blue balls represent Ba and Si atoms, respectively.

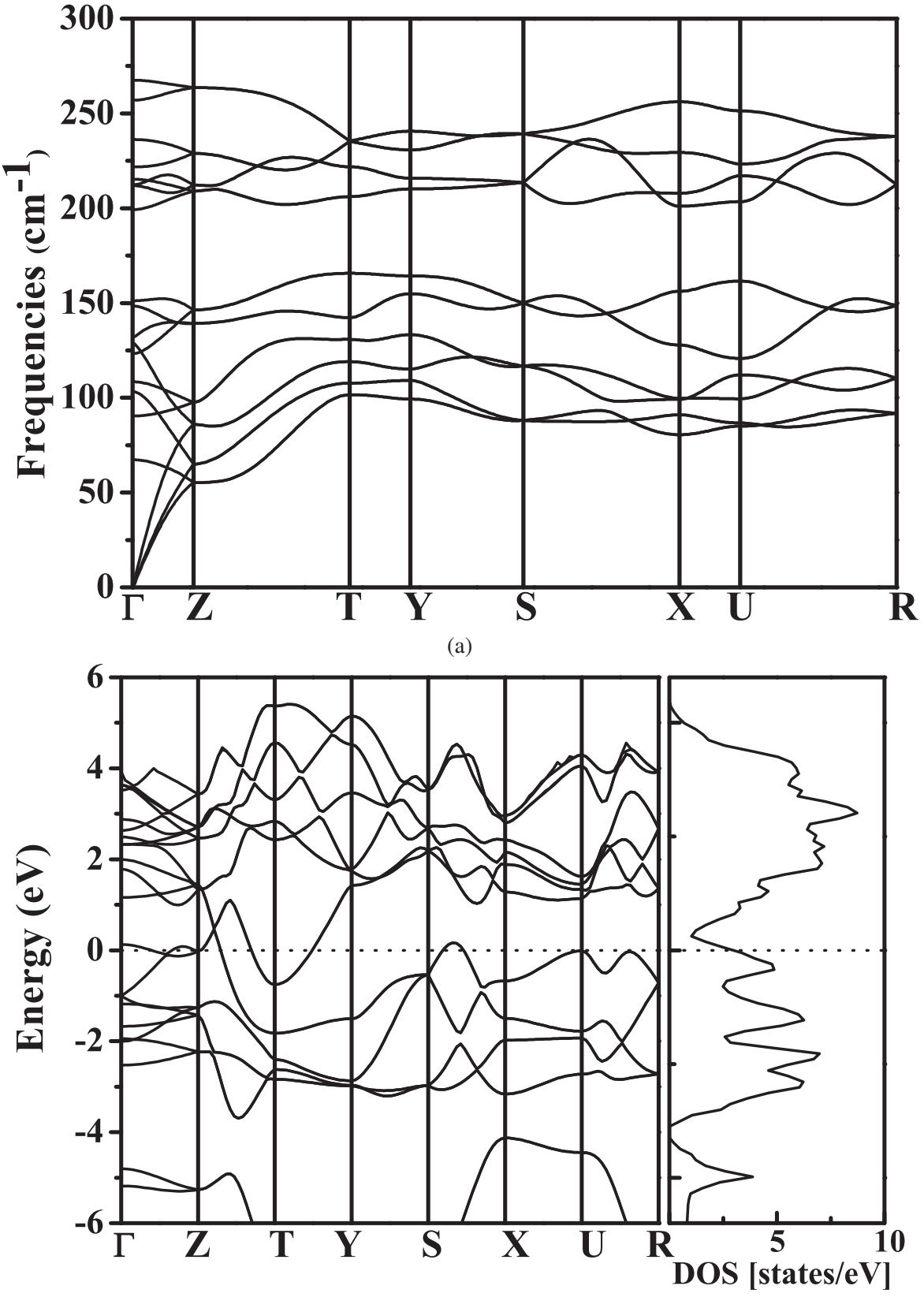

Figure 3.5 (a) Phonon dispersions of the *Imma* phase of BaSi at 20 GPa. (b) Electronic band structures and densities of state of the *Imma* phase of BaSi at 20 GPa.

silicon atoms in the *Imma* phase is 2.31 Å, while the angle of the chain is about 105.34° at 20 GPa. To demonstrate the dynamical stability of this structure, we calculated the phonon dispersion for the *Imma* phase at 20 GPa, as shown in Fig. 3.5a. There are no imaginary phonon frequencies, which indicates that the *Imma* structure is mechanically stable. The electronic band structure and projected density of states (DOS) for the *Imma* structure at 20 GPa are also shown in Fig. 3.5b, showing that this is a metallic phase.

3.3.2 $BaSi_2$

From Fig. 3.1 we can see that $BaSi_2$ is a stable composition from ambient pressure to more than 100 GPa. At ambient pressure our structural prediction runs find many possible low-energy structures, in good agreement with previous studies [81–84, 95, 120–123]. The lowest energy structure is the orthorhombic *Pnma* phase, with several other phases competing in the narrow energy range of a few tenths of an meV/atom. The phase transition from the *Pnma* to the $P4_332$ phase is predicted to occur at 1 GPa, followed by a phase transition to a $P3m1$ structure at about 3.5 GPa, and then to a $P6/mmm$ phase at around 18 GPa. All these results are in good agreement with previous works [81–84]. However, at pressures above 20.8 GPa we found that the ground-state structure is a new cubic phase with $Fd\bar{3}m$ symmetry. Moreover, this is the only low-enthalpy phase that we found in our simulations at high pressure. From Fig. 3.6 we can see that the $Fd\bar{3}m$ phase is stable with respect to decomposition in Ba and Si in a large range of pressures from 21 GPa to more than 100 GPa.

The new $Fd\bar{3}m$ phase can seen in Fig. 3.4 (b). In our opinion this is a remarkable structure for several reasons. Four neighboring silicon atoms form a regular tetrahedron with a side of 2.54 Å at 50 GPa. These tetrahedral then combine into larger tetrahedral, as shown on Fig. 3.4 (b). 6-fold coordination is observed in the first high pressure phase of pure silicon (β-tin structure), even if it is not a regular octahedron. Due to this unique structural arrangement, the $Fd\bar{3}m$ phase is the ground-state in a large range of pressure. In order to ensure the thermal stability of $Fd\bar{3}m$, we calculated the phonon dispersion of this phase at 50 GPa, as shown in Fig. 3.7a. As expected, The $Fd\bar{3}m$ phase is mechanically stable. We also calculated the electronic band structure and projected density of states, as shown in Fig. 3.7b. It is evident that the $Fd\bar{3}m$ phase is also a metallic phase. We obtained the superconducting transition temperature of the $Fd\bar{3}m$ phase by calculating the electron-phonon coupling parameter λ and the Eliashberg phonon spectral function $\alpha^2F(\omega)$. The results are shown in Fig. 3.8. The overall integrated λ is 0.4, while the logarithmic average of the phonon frequency $\omega_{\log}$ is 320 K. The superconducting critical temperature T_c estimated by using the McMillan equation [124] modified by Allen and Dynes. is 1.24 K at 50 GPa with

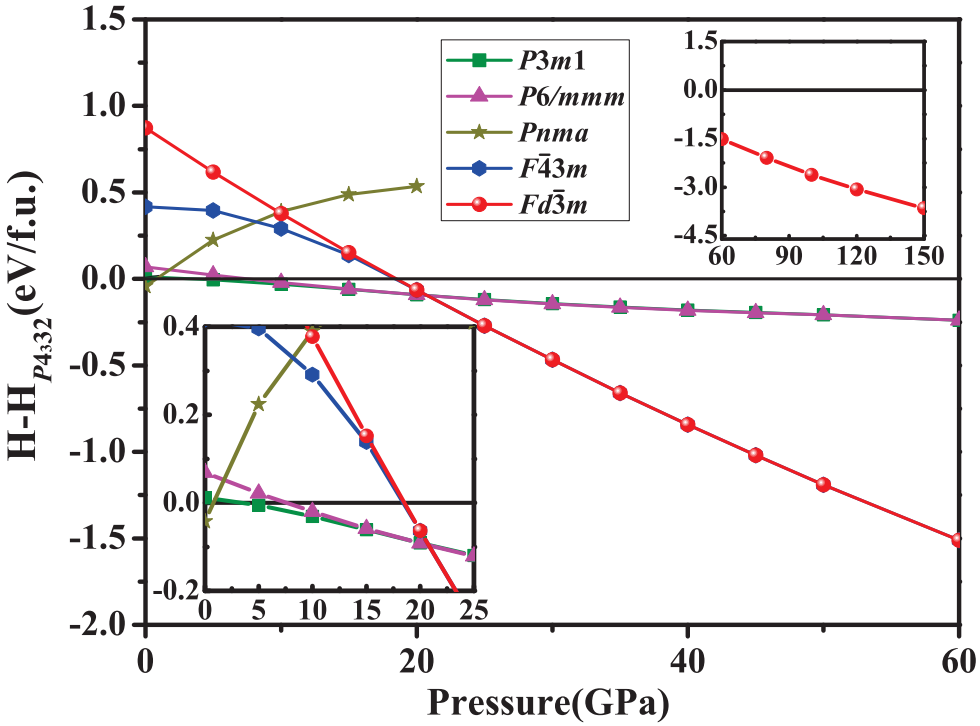

Figure 3.6 Enthalpy per formula unit of the different phases of $BaSi_2$ relative to the $P4_332$ phase as a function of pressure.

the screened Coulomb interaction μ^* =0.12. All these results are in good agreement with a previous work [125]. X-ray diffraction at ambient conditions shows the pressure induced amorphization of $BaSi_2$ beyond 10 GPa [126]. Consequently the experimental identification of the new $Fd\bar{3}m$ phase will most probably need to perform a combined high pressure and high temperature experiment.

There are strong similarities between the tetrahedral arrangement of the Si atoms and the so-called T-carbon, a recently proposed allotrope of diamond [127]. Both phases are constructed from tetrahedra, however T-carbon is obtained by occupying a diamond lattice site with a tetrahedra. In order to better compare both geometrical arrangements we studied the Si framework of our $Fd\bar{3}m$ structure by removing the Ba atoms, and compared it to T-silicon i.e., the phase obtained by replacing C by Si in the T-carbon structure. T-silicon is considerably less dense (with a volume of 52.21 $Å^3$/atom) than our structure (21.61 $Å^3$/atom). For comparison, silicon in the diamond structure has a volume of 20.35 $Å^3$/atom within our numerical approximations. It turns out that our structure is considerably lower in energy than T-silicon (by 0.38 eV per atom), but still considerably higher than silicon in the diamond structure (by 0.66 eV/atom). Unfortunately, such large energy differences probably mean that it is impossible to stabilize these silicon phases at ambient pressure.

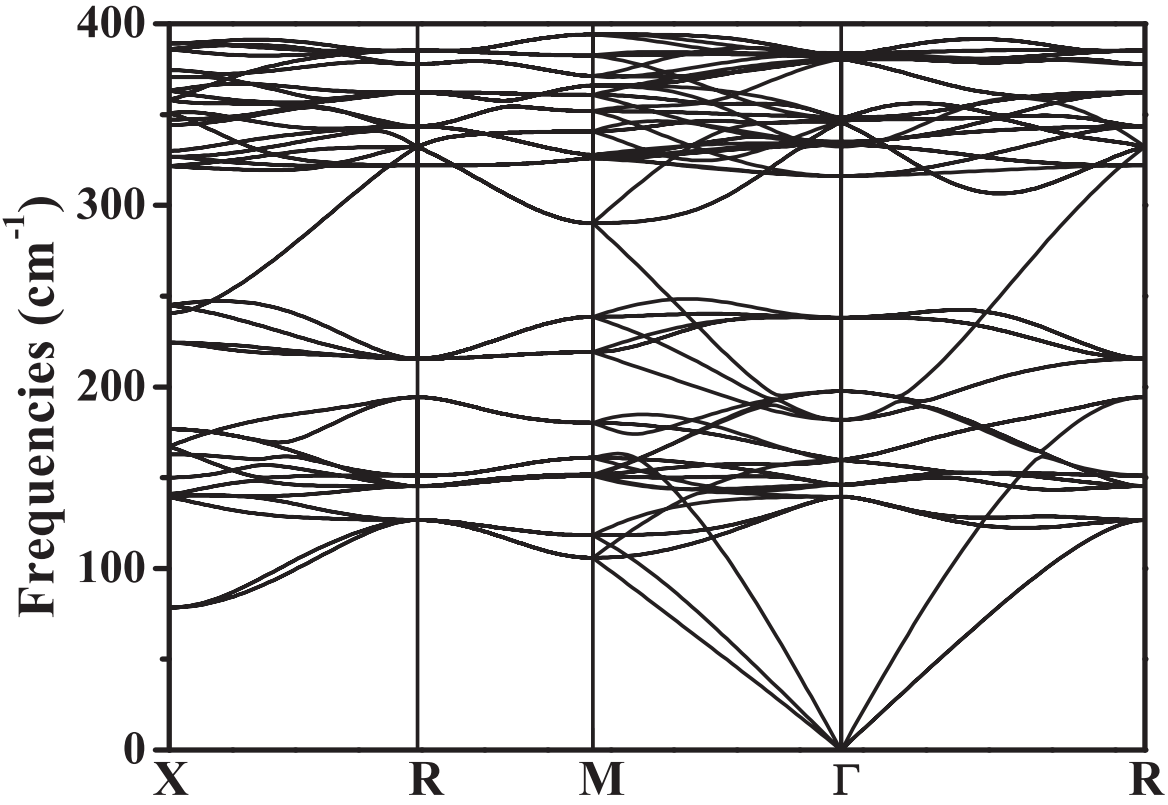

(a)

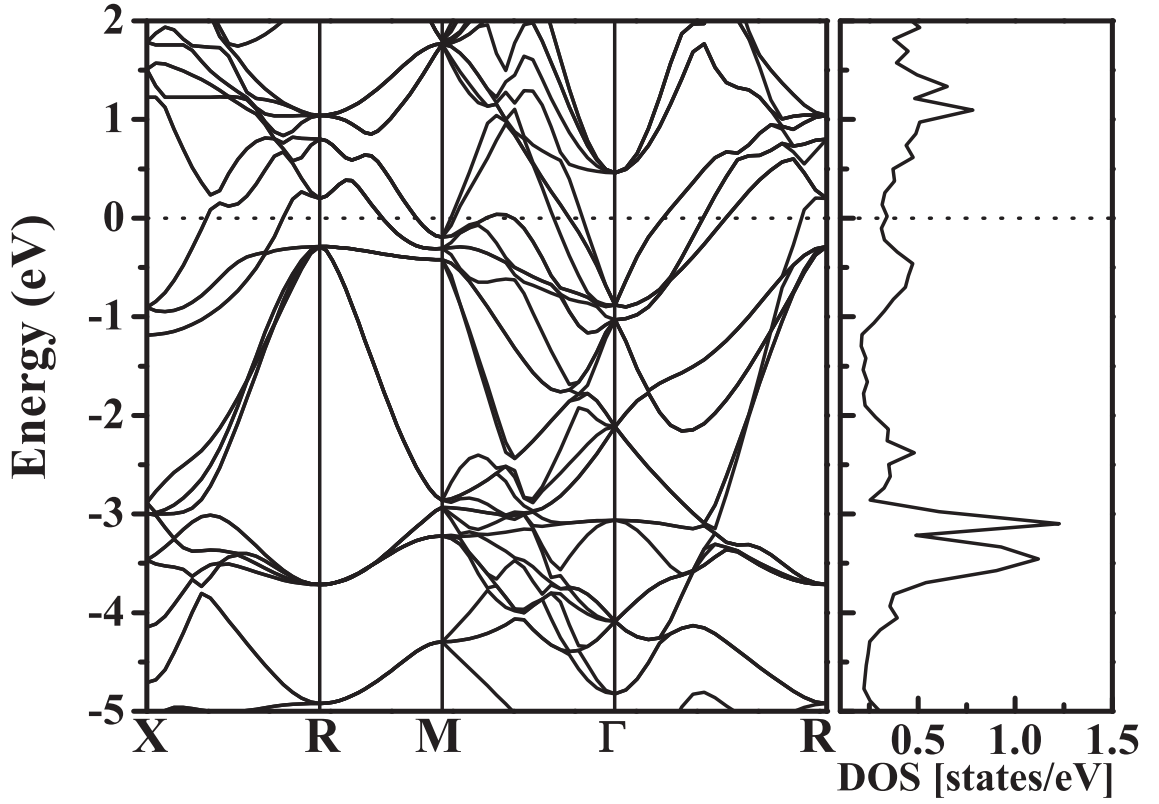

(b)

Figure 3.7 (a) Phonon dispersions of the $Fd\bar{3}m$ phase of $BaSi_2$ at 50 GPa. (b) Electronic band structures and densities of state of the $Fd\bar{3}m$ phase of $BaSi_2$ at 50 GPa.

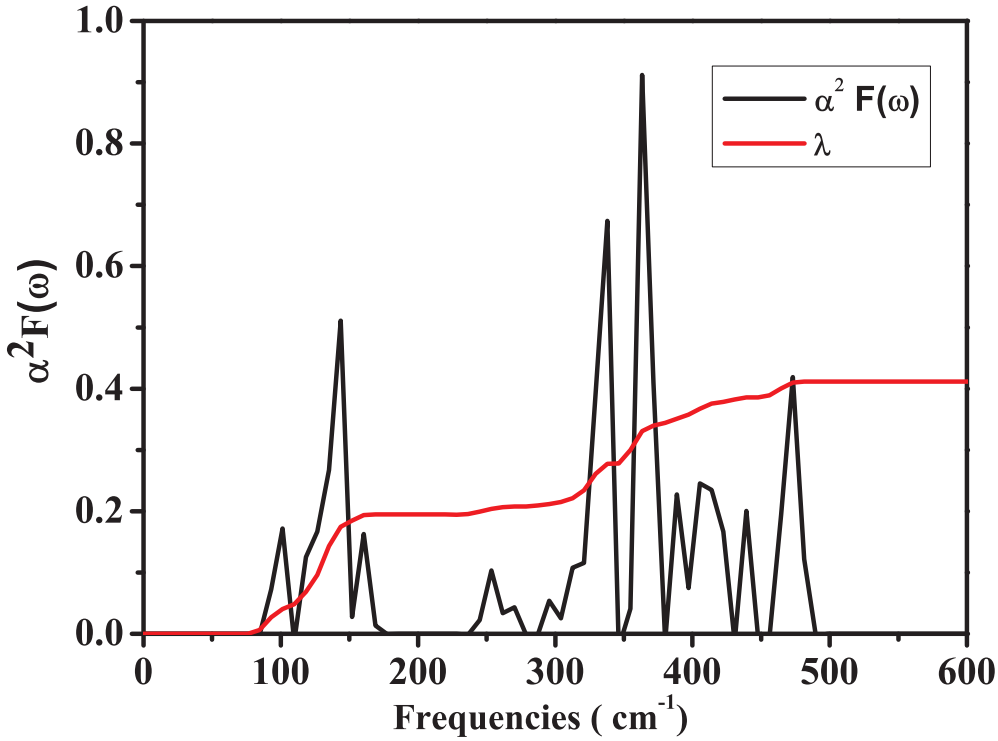

Figure 3.8 Eliashberg phonon spectral function $\alpha^2F(\omega)$ and integrated EPC parameter λ as a function of frequency for the $Fd\bar{3}m$ structure at 50 GPa.

3.3.3 $BaSi_3$, $BaSi_5$ and $BaSi_6$

The composition $BaSi_3$ is very close to the convex hull for pressures of around 20 GPa. Our predicted structure [see Fig. 3.4 (c)] has $I4/mmm$ symmetry and 4 formula units in its primitive cell. This is a very complicated and unusual structure, with corrugated Ba planes separated by Si layers. In these layers we find silicon cubes connected between themselves through bridging Si atoms in a two-dimensional lattice. The smallest distance between two silicon atoms at 20 GPa is 2.34 Å, while the longest Si-Si bond is 2.47 Å.

On the other hand, we found that $BaSi_5$ crystallizes in a fascinating *Cmmm* structure [see Fig. 3.4 (d)] that is on the convex hull in a small pressure range at around 20 GPa. This phase consists of two superposed flat hexagonal Si layers intercalated by Ba atoms that are located at the center of the Si hexagons. Between the two Si planes one finds further Si atoms also at the center of the hexagons. The Si-Si bond distance is in this case 2.43 Å.

The composition $BaSi_6$ is stable at pressures from 5 to 20 GPa. Our structural prediction runs find an interesting structure with *Cmcm* symmetry, where silicon atoms form a beer barrel type polyhedron, with the polyhedra linked by sharing faces to form channels containing the Ba atoms. This is the same structure found in previous works [95].

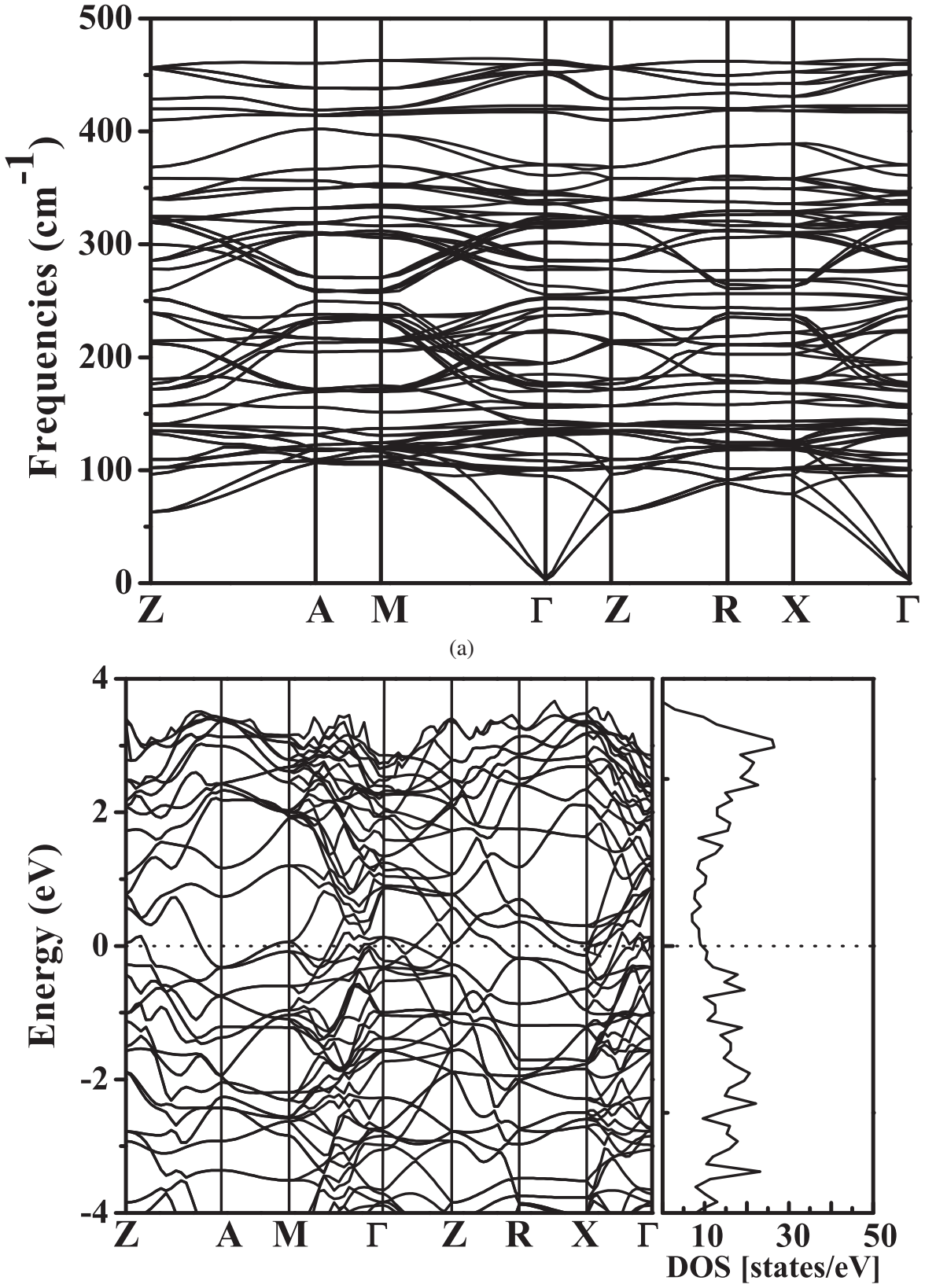

Figure 3.9 (a) Phonon dispersions of the $I4/mmm$ phase of $BaSi_3$ at 20 GPa. (b) Electronic band structures and densities of state of the $I4/mmm$ phase of $BaSi_3$ at 20 GPa.

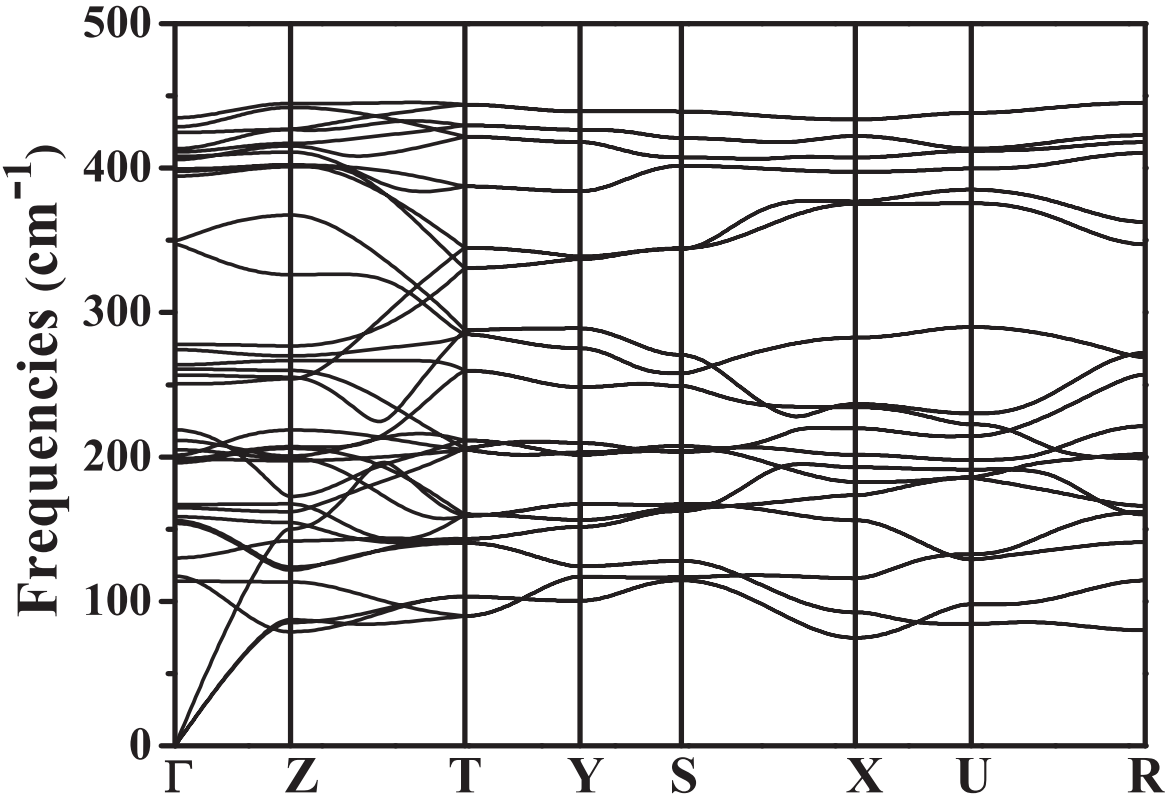

(a)

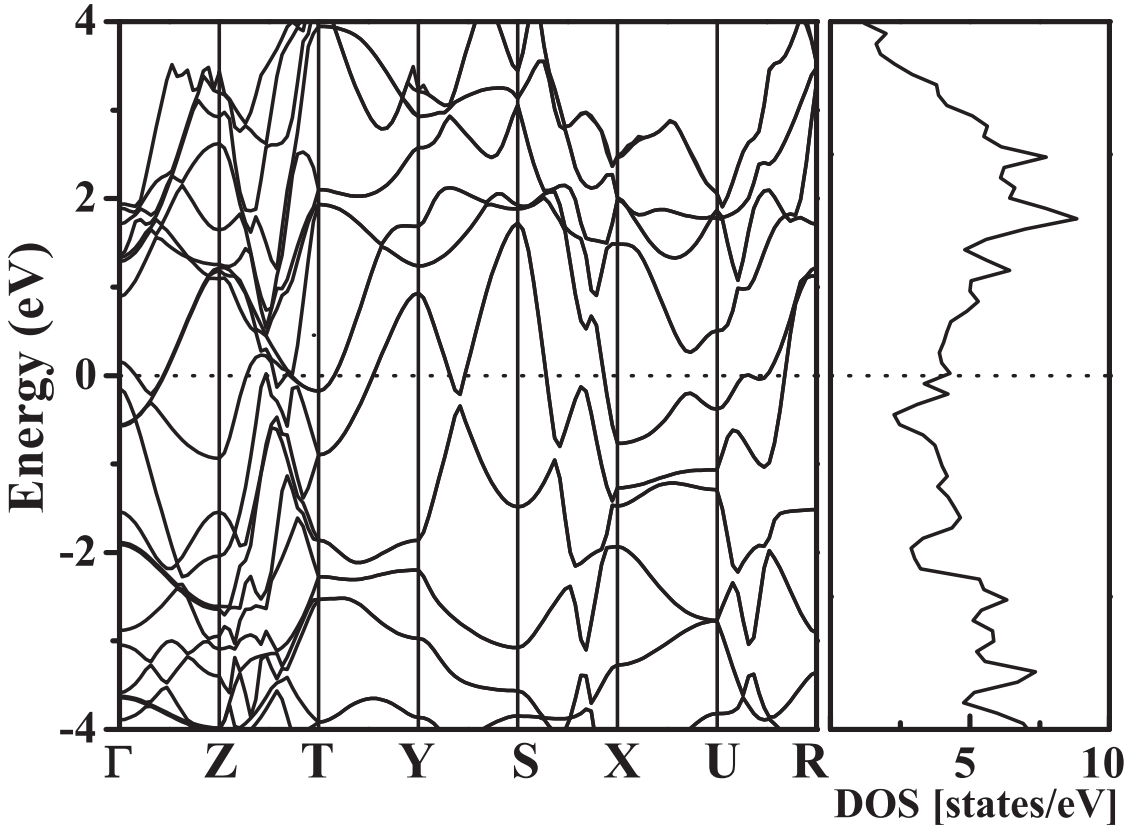

(b)

Figure 3.10 (a) Phonon dispersions of the *Cmmm* phase of $BaSi_5$ at 20 GPa. (b) Electronic band structures and densities of state of the *Cmmm* phase of $BaSi_5$ at 20 GPa.

From the phonon dispersion of the $I4/mmm$ phase of $BaSi_3$ and the $Cmmm$ phase of $BaSi_5$, as shown in Fig. 3.9a and Fig. 3.10a, we can ensure that both structures are mechanically stable. We calculated the band structure and the electronic density of states for the $I4/mmm$ phase of $BaSi_3$ and the $Cmmm$ phase of $BaSi_5$. As shown in Fig. 3.9b and Fig. 3.10b, both phases are metallic.

3.4 Conclusions

In summary, using a global structural prediction method we studied systematically the phase diagram and the electronic properties of Ba–Si compounds. We identify five novel stoichiometric $BaSi_x$ phases with unexpected structures that might be experimentally synthesizable over a wide range of pressure. These include BaSi, $BaSi_2$, $BaSi_3$, $BaSi_5$, and $BaSi_6$. For the BaSi system, we find a new metallic $Imma$ phase that is stable under pressure from 6 GPa to 65 GPa. For $BaSi_2$, there is a new metallic phase $Fd\bar{3}m$ that is stable from 21 GPa to 100 GPa. This phase, in which each Si forms six bonds with other neighboring Si atoms, becomes superconducting below 1.2 K at 50 GPa. Finally, at around 20 GPa two unexpected compositions become stable, namely $BaSi_3$ ($I4/mmm$) and $BaSi_5$ ($Cmmm$), both displaying metallic behavior. These results show the remarkable variety of Ba–Si compounds, and can serve as an important guide for further experimental studies of this binary system.

Chapter 4

Phase diagram of N-H-O system under high pressure

4.1 Introduction

Nitrogen, oxygen and hydrogen are some of the simplest and better studied elements of the periodic table. Moreover, they are some of the most abundant elements in the solar system and form several textbook compounds (such as water, nitrogen oxides, ammonia, nitric acid, etc.) that are fundamental not only to life, but also to modern industry [128–132]. The ternary phase diagram H–N–O is extremely well characterized as a function of temperature at ambient pressure. There are also a large amount of studies, both experimental and theoretical, focused on the binary phase diagrams H–N, H–O, and N–O up to very high pressures [133–135]. However, much less is known about the ternary diagram at high pressure.

Our aim in this chapter is to perform a systematically study of the ternary H–N–O phase diagram as a function of pressure. Our main tool are global structural prediction methods. These methods have proved extremely important in exploring phase-diagrams under pressure in the last years, and have yielded a remarkable number of important results. For example, they were used to show that the xenon apparently missing from the Earth is in fact bound with iron at the interior of our planet [98], or that simple alkali metals become semiconducting and transparent under pressure [136]. More recently, structural prediction was able to find superconductivity with record transition temperature in hydrogen sulfide [137, 138], a prediction that was quickly confirmed experimentally one year later [139].

It is simple to understand the importance and attractiveness of structural prediction in high pressure science. High-pressure changes substantially the chemistry, leading to novel and

unexpected bonding patterns, making predictions based on our (ambient pressure) intuition often to fail spectacularly. Furthermore, high-pressure investigations, requiring delicate diamond anvil cell experiments, are difficult and expensive. Computers, on the other hand, are by now ubiquitous and have reached unparalleled performances. Computer experiments appear therefore as a fast and cost-efficient method to explore the phase diagram of solid substances as a function of pressure.

There are several powerful global structural prediction algorithms developed over the past decade (such as genetic algorithms [54–56], particle swarm methods [67, 68], random search [63], minima hopping method [69, 70], etc.), and these are now available in a number of freely available codes. It is therefore not surprising that global structural prediction studies of bulk solids under pressure have mushroomed over the past years. A large majority of these works concentrate on single stoichiometries or binary phase diagrams. Studies of ternary phase diagrams are of course rarer, due to the much larger number of possible compositions, and the consequent increase of the required computational effort.

4.2 Elementary and binary phase diagrams

The H–N–O phase diagram in its elementary and binary versions has been extensively studied, both experimentally and theoretically, in a wide range of pressures and temperatures. In the following, we will try to summarize briefly the current knowledge of this phase diagram, starting with the elemental phases.

Hydrogen as the first and arguably the simplest element of the periodic table, has attracted much attention since Wigner and Huntington proposed in 1935 that solid hydrogen might dissociate into an atomic metal at around 25 GPa [128]. Unfortunately, the extremely weak X-ray scattering of hydrogen and the lack of convenient experimental methods hindered for a long time experimental studies of the low-temperature and high-pressure structures. Phase I of hydrogen consists of a disordered *hcp* structure [140], while the low temperature and high pressure phases II and III of hydrogen were extensively studied both experimentally and theoretically [63, 103, 141–147]. More recently, experimental results suggest a phase transition to a metallic, atomic phase at around 447 GPa [148], but these results are still under intense debate.

Nitrogen has a remarkably rich phase-diagram, with no less than 13 solid molecule phases [129, 149–155], an amorphous state [150] and two non-molecular phases [156, 157]. At 300 K, nitrogen freezes at 3 GPa to β-N_2, and further compression results in the δ, δ_{loc}, ε, ζ and κ phases at 5, 11, 16, 60, and 115 GPa, respectively [130, 131, 151, 158, 159]. Finally, at about 150 GPa, there is a transition to the amorphous η which exhibits substantial

pressure hysteresis [150, 160]. Recently, Frost and co-workers synthesized λ-N_2 through low temperature compression and observed it to have a remarkably wide stability range [161].

Oxygen also exhibits a rich polymorphism with seven unambiguously established crystalline phases. At ambient pressure and as a function of temperature, oxygen solidifies to the paramagnetic γ-phase, then to the magnetically disordered β-phase [132, 162] and ultimately to the anti-ferromagnetic α-phase [163]. At the pressure of 6 GPa, the α-phase transforms into the anti-ferromagnetic δ-phase [164–166]. As the pressure increases to about 8 GPa, the δ-phase of oxygen is destroyed, leading to the ε-O_8 phase consisting of O_8 clusters [167, 168]. Above 96 GPa, ε-O_8 was observed to transform into a metallic ζ-phase [169, 170] (that intriguingly exhibits superconductivity with a transition temperature of 0.6 K [171]). Zhu and co-workers predicted another phase of oxygen at 1.92 TPa exhibiting polymeric spiral chains of O_4 [101]. These studies explored the high-pressure phase diagrams of solid oxygen up to the maximum pressure of 2 TPa.

Like the elementary substances, also the binary N–H, N–O, and O–H systems have been extensively studied. The low temperature and pressure phase-I ($P2_13$) of NH_3 undergoes first-order phase transitions into phase-IV ($P2_12_12_1$) at around 3-4 GPa and then into phase-V at about 14 GPa [133–135]. In 2008, Pickard *e*t al. found that the phase-V of ammonia also belongs to the space group of $P2_12_12_1$. Furthermore, they predicted two new ionic phases (Pma2 and $P2_1/m$) under high pressure that then re-transform into a molecular phase (Pnma) at about 440 GPa [64].

As one of the most important binary compounds, H_2O ice has a very rich phase diagram. Till now, at least 15 solid phases have been identified experimentally [172, 173] and another 7 high-pressure phases have been predicted through theoretical studies [174–177]. Experimentally, all crystalline phases were found to consist of water molecules connected by hydrogen bonds except ice-X. This is an atomic crystal that is stable above 70 GPa at low temperature.

Nitrogen oxides like NO, N_2O_5, NO_2 and N_2O have also been studied both experimentally and theoretically. NO is a metastable compound at low pressure, while a polymeric NO structure becomes stable at 198 GPa [178]. Molecular N_2O_5 phases are stable in a wide pressure range from 9 to 446 GPa, when they decompose into NO and O [178]. The cubic phase ($Im-3$) of NO_2 forgoes two phase transitions at 7 GPa (to a $P2_1/c$ crystal) and then at 64 GPa (to an another $P2_1/c$ phase), before decomposing at 91 GPa [178]. N_2O follows a series of phase transitions from $Pa\bar{3}$[179] $\rightarrow$ $Cmca$[180] $\rightarrow$ $C2m$[181] $\rightarrow$ $P2_1/m$[182] at the pressures of 5, 57, 177 and 194 GPa, respectively.

Finally, the ternary phase AMH I [183] of NH_3H_2O transforms into AMH II [184] at about 2.8 GPa and then transforms into a $P4/nmm$ and then to a $Ima2$ phase at 3.3 GPa and 42 GPa [185] respectively. On the other hand, a new high-pressure phase ($P2_1/c$) of

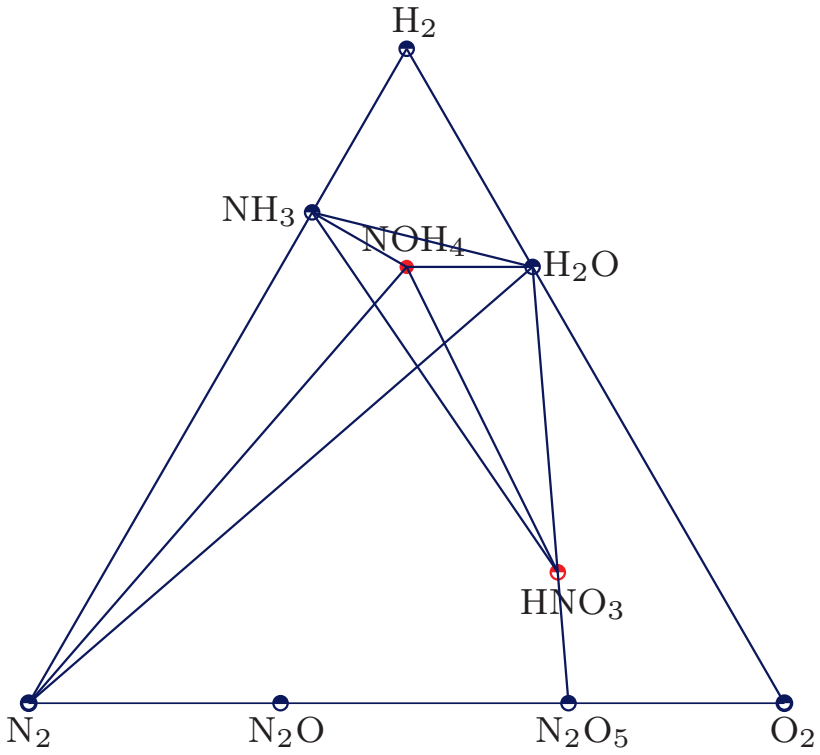

Figure 4.1 Ternary phases diagram of the N–H–O system at 150 GPa. The novel phases are marked in red.

pure nitric acid (HNO_3) has been characterized at 1.6 GPa at room temperature by high-pressure neutron powder and X-ray single-crystal diffraction techniques by D. R. Allan and co-workers in 2010 [186].

4.3 Methods

For our study we chose to perform structural prediction with a method based on a particle-swarm optimization algorithm as implemented in the CALYPSO code [67, 68]. This method is unbiased by any known structural information, and has been successfully used for the prediction of various systems under high pressure [106, 107, 187]. The underlying ab initio structural relaxations and the electronic band structure calculations were performed within the framework of density functional theory (DFT) as implemented by the VASP code [109]. The calculations were carried out at the level of the generalized gradient approximation using the Perdew-Burke-Ernzerhof [25] (PBE) approximation for the exchange correlation functional. The electronic wave functions were expanded in a plane wave basis set with a cutoff energy of 600 eV. The electron-ion interaction was described by means of projector

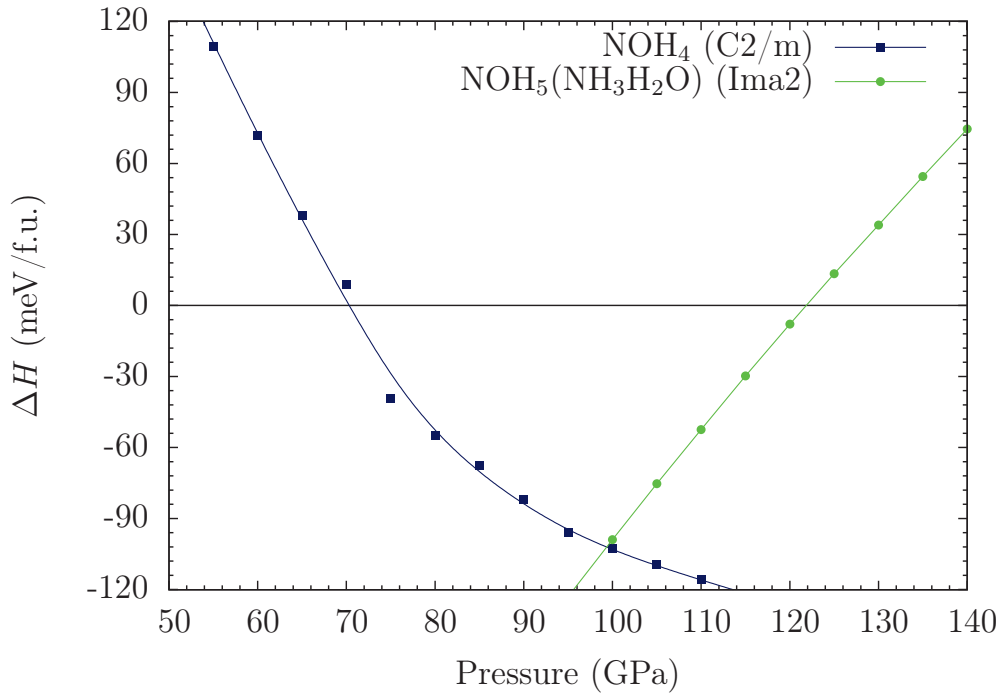

Figure 4.2 Enthalpy per formula unit of the *Ima*2 phase of NOH_5 (NH_3H_2O) and of the C2/m phase of NOH_4 as a function of pressure. The zero line corresponds to the decomposition into NH_3 and H_2O (for NOH_5) and into NH_3, H_2O, and N_2 (for NOH_4).

augmented wave (PAW) [110] pseudopotentials with $1s^1$, $2s^2 2p^3$ and $2s^2 2p^4$ electrons in the valence for the H, N and O atoms, respectively. Monkhorst-Pack k-point [111] meshes with a grid density of 0.03 $Å^{-1}$ were chosen to achieve a total energy convergence of better than 1 meV per atom. The phonon dispersion curves were computed by the direct supercell calculation method as implemented in the Phonopy program [113].

4.4 Results and discussion

We investigated systematically the phase stability of stoichiometric NOH_x (x = 1, 2, 3, 4, 5), HON_x (x = 1, 2, 3, 4, 5), HNO_x (x = 1, 2, 3, 4, 5) and H_3NO_4 compounds at the pressure of 50, 100 and 150 GPa. The structural predictions were performed with simulation cell sizes of 2 and 4 formula units (f.u.). We calculated the convex hull with respect to the decomposition into all known phases of the H–N–O ternary system in their corresponding stable pressure range. They are: H_2 ($C2/c$), N_2 ($I2_13$), O_2 ($C2/m$), H_2O (phase X for the pressure above 70 GPa and phase VIII below 70 GPa), N_2O ($P2_1/c$) and N_2O_5 ($C2/c$).

Our main result is the ternary phase diagram of H–N–O, that is shown in Fig. 4.1 for a pressure of 150 GPa (the largest pressure considered). Meta-stable compositions that appear

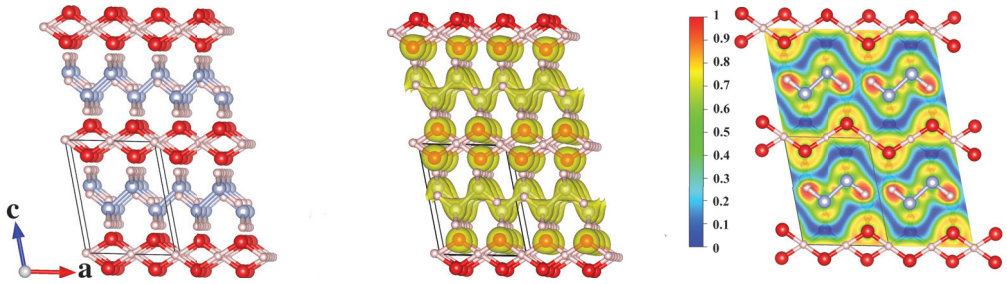

(a) (b) (c)

Figure 4.3 (a) Crystal structure of NOH_4 with space group of $C2/m$. The white, blue and red atoms represent H, N and O, respectively. (b) Charge density plot. (c) Electron-localization function on a plane perpendicular to the (010) crystallographic direction.

above the convex hull are not plotted for clarity. There are several conclusions that we can immediately extract from Fig. 4.1. First, all compositions HON_x (x = 1, 2, 3, 4, 5) are above the convex hull, which implies that they are not thermodynamically stable at 150 GPa. For HNO_x (x = 1, 2, 3, 4, 5), only HNO_3 (nitric acid) is on the convex hull, although in a novel structure different from the low-pressure phases. Finally, for NOH_x (x = 1, 2, 3, 4, 5) the only stable composition is interestingly not NOH_5 (i.e., NH_3H_2O, a mixture of water and ammonia that is 0.098 eV/f.u. above the hull) but NOH_4. This is again an indication of the profound influence that high pressure has on the chemistry of even simple elements, leading to surprising stoichiometries, bonding patterns, and crystal structures.

The structures of two novel phases HNO_3 and NOH_4 are shown in Fig. 4.3 (a) and Fig. 4.4 (a) and (b). We also ploted the charge density and electron localization functions of these two phase, as shown in Fig. 4.3 (b) and (c) and Fig. 4.4 (c) and (d), respectively. A complete summary of the results is shown in Tab. 4.1, which includes the structural parameters of our predicted stable structures for the N–H–O ternary system. In the following we analyze systematically these two new phases.

We calculated the dependence of the enthalpy on the applied pressure for the decomposition of NOH_5 and NOH_4 into water, ammonia, and nitrogen, as shown in Fig. 4.2. We find that NH_3H_2O is stable in a large range of pressures, in good agreement with previous works [185], but that it becomes thermodynamically unstable at around 122 GPa when it decomposes into NH_3 and H_2O. We find the opposite behavior for NOH_4 that becomes stable at around 71 GPa, as shown in Fig. 4.2.

The new phase of NOH_4 has $C2/m$ symmetry (space group #12) with 24 atoms per unit cell as shown in Fig. 4.3 (a), and is composed by O–H chains separated by a layer of NH_3 molecules. To understand the bonding character of this structure, we plot in Fig. 4.3 (b) the charge density and in Fig. 4.3 (c) the electron localization function (ELF). This latter

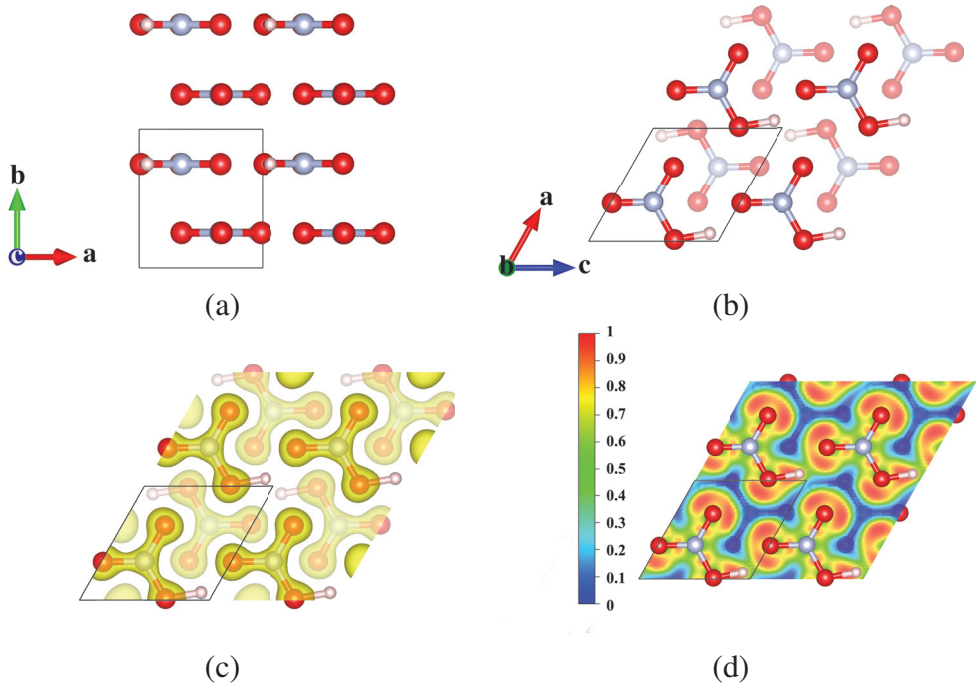

Figure 4.4 (a) and (b) The $P2_1/m$ phase of HNO_3. The red, light blue, and white atoms represent respectively O, N and H. (c) Charge density plot of the $P2_1/m$ phase of HNO_3. (d) Slabs cut along the (010) direction of the ELF. For clarity, we used here a $(2\times1\times2)$ supercell.

quantity is a valuable tool developed in quantum chemistry to visualize bonds, lone pairs, etc. It assumes values in the range from zero to one, with one meaning perfect localization of electrons (such as in a bond). We find that the ELF has large values between two NH_3 molecules, indicating a covalent bond between the two N atoms. We thus conclude that the NH_3 layer is in fact built from N_2H_6 "dumbbell" clusters.

The H–O distance is 1.117 Å and the H–O–H angle is 112.87° at 150 GPa. In the chains, the electrons are mainly distributed in the center of the O–H bonds. The covalent character of these bonds can also be confirmed by the charge density plot in Fig. 4.3 (b). On the other hand, the N–N distance is 1.355 Å at 150 GPa. The N–N bond is a single bond, which is confirmed by the shape of the ELF.

The $C2/m$ phase of NOH_4 at 150 GPa is dynamically stable as it does not exhibit any imaginary phonon frequencies, as shown in Fig. 4.6. The electronic band structure and projected density of states (DOS) are shown in Fig. 4.5. We see that the $C2/m$ phase is an insulator with a large band gap of 6.0 eV at 150 GPa. Note that this value was calculated with the PBE functional, that systematically underestimate band-gaps.

HNO_3 (nitric acid) at 150 GPa crystallizes in a novel phase of $P2_1/m$ symmetry and with an interesting structural configuration containing two parallel layers forming a "quasi clover"

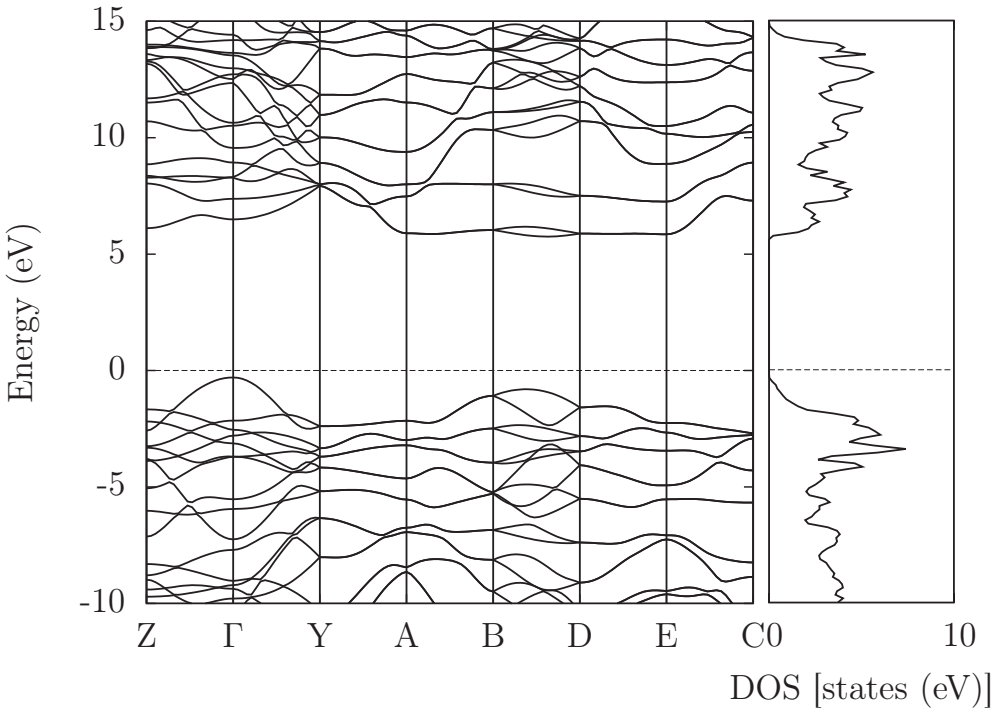

Figure 4.5 Band structure and density of states of the $C2/m$ phase of NOH_4 at 150 GPa.

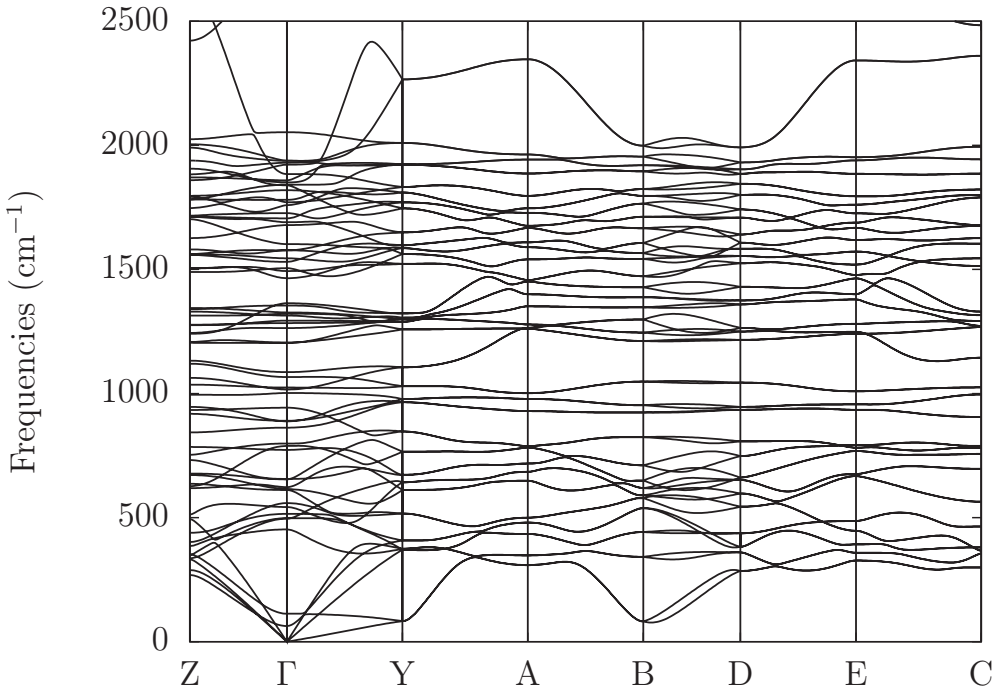

Figure 4.6 Phonon dispersion of the $C2/m$ phase of NOH_4 at 150 GPa.

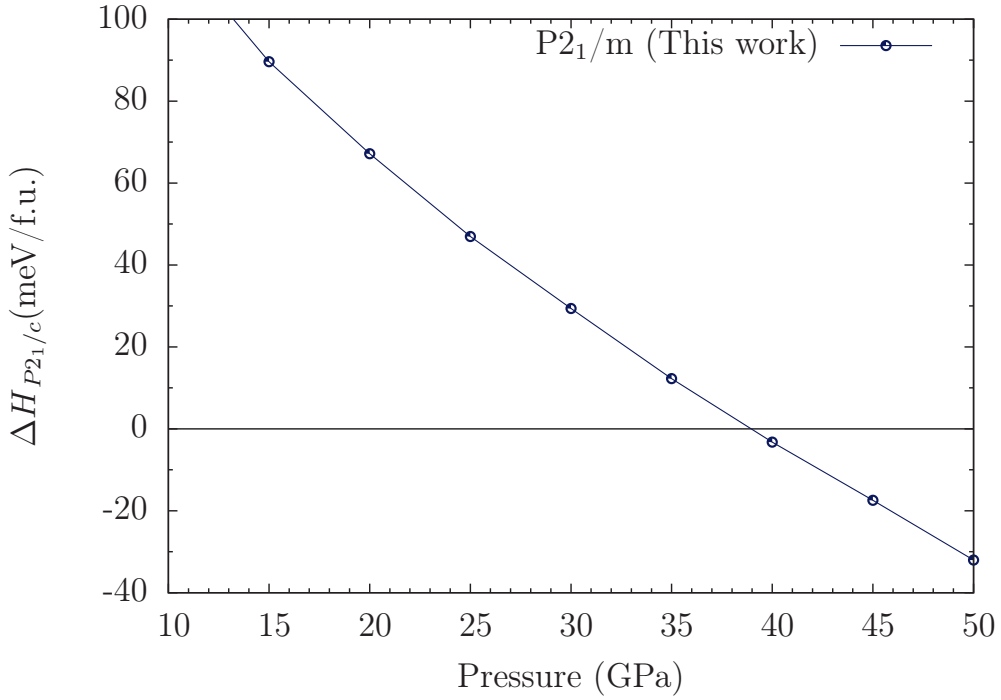

Figure 4.7 Relative enthalpy per formula unit of the new phase $P2_1/m$ of HNO_3 with respect to phase II ($P2_1/c$) of nitric acid as a function of pressure.

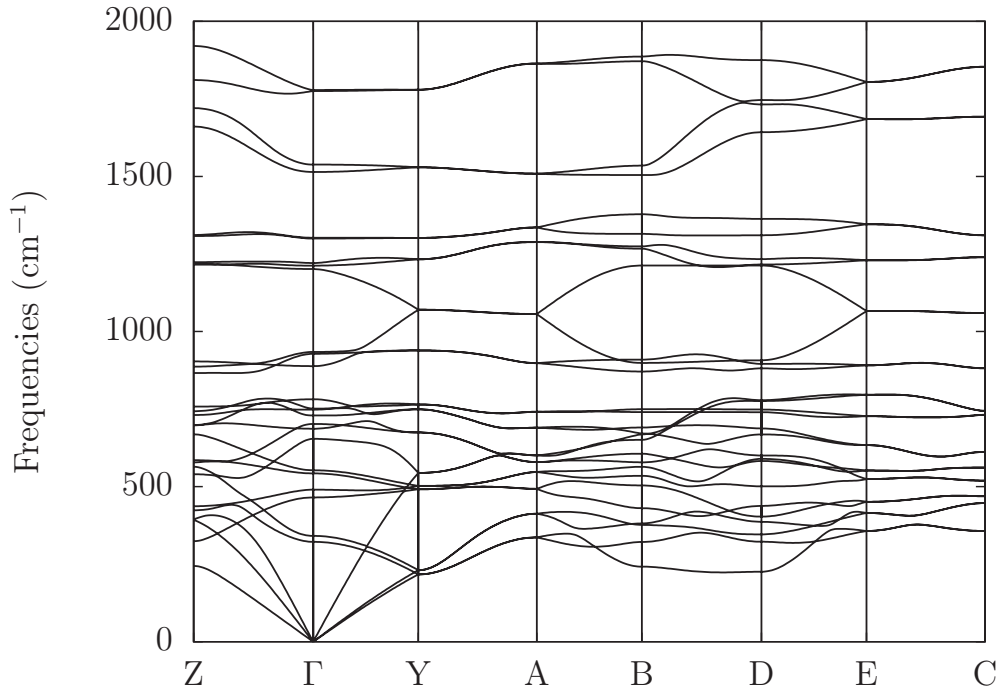

Figure 4.8 Phonon dispersion of the $P2_1/m$ phase of HNO_3 at 150 GPa.

Table 4.1 Calculated structural parameters of our predicted stable structures of the N–H–O compounds at their corresponding pressures.

Space group Pressure	Lattice parameters	Atomic coordinates (fractional)
$C2/m$-NOH_4	a=4.80513 Å	H (8j) 0.73862 0.27769 0.18187
150 GPa	b=3.94998 Å	H (2a) 0.00000 0.00000 0.00000
	c=3.72274 Å	H (2b) 0.00000 0.50000 0.00000
	α=γ=90°	H (4i) 0.47412 0.00000 0.83563
	β=101.9°	O (4i) 0.86866 0.00000 0.21498
		N (4i) 0.60060 0.00000 0.65717
$P2_1/m$-HNO_3	a=3.76343 Å	H (2e) 0.09859 0.25000 0.06669
150 GPa	b=3.71923 Å	O (2e) 0.34502 0.25000 0.01337
	c=3.79534 Å	O (2e) 0.67110 0.25000 0.65678
	α=γ=90°	O (2e) -0.01431 0.25000 0.33338
	β=119.7°	N (2e) 0.67195 0.25000 0.34246
$Ima2$-NOH_5	a=3.82308 Å	H (8h) 0.00000 0.05335 0.26087
(NH_3H_2O)	b=4.11076 Å	H (8i) 0.27414 0.25000 0.02918
100 GPa	c=5.62304 Å	H (4d) 0.25000 0.25000 0.75000
	α=β=γ=90°	O (4e) 0.00000 0.25000 0.86373
		N (4e) 0.00000 0.25000 0.37254

with a H atom tail. There are 10 atoms in the unit cell, as shown in Fig. 4.4 (a) and (b). The "quasi clover" is formed by three nitrogen atoms, one oxygen atom and one hydrogen atom. Every N atom in the middle of the "quasi clover" has three nearest O atoms while one of the three O atoms is bonded with one H atom.

The charge density plot of the $P2_1/m$ phase of HNO_3 is shown in Fig. 4.4 (c). We can clearly find that the electron cloud is almost entirely distributed around the region between the N and O atoms. Obviously, there are two different kinds of N–O covalent bonds with bond lengths of 1.195 Å and 1.246 Å at 150 GPa. From the plot of the ELF [see Fig. 4.4 (d)] one can distinguish the three N–O covalent bonds, together with the lone pairs around the oxygen atoms. The O–H bond distance is 1.042 Å at 150 GPa.

The relative enthalpy per formula unit of the new $P2_1/m$ phase of HNO_3, with respect to the phase II ($P2_1/c$) [186], is shown in Fig. 4.7 as a function of pressure. Our calculations show that the new phase of becomes energetically favorable in a large range of pressures from about 39 GPa to more than 150 GPa.

Finally, we calculated the phonon dispersion of this phase at 150 GPa, as depicted in Fig. 4.8, that proves that the $P2_1/m$ phase is mechanically stable. We also calculated the

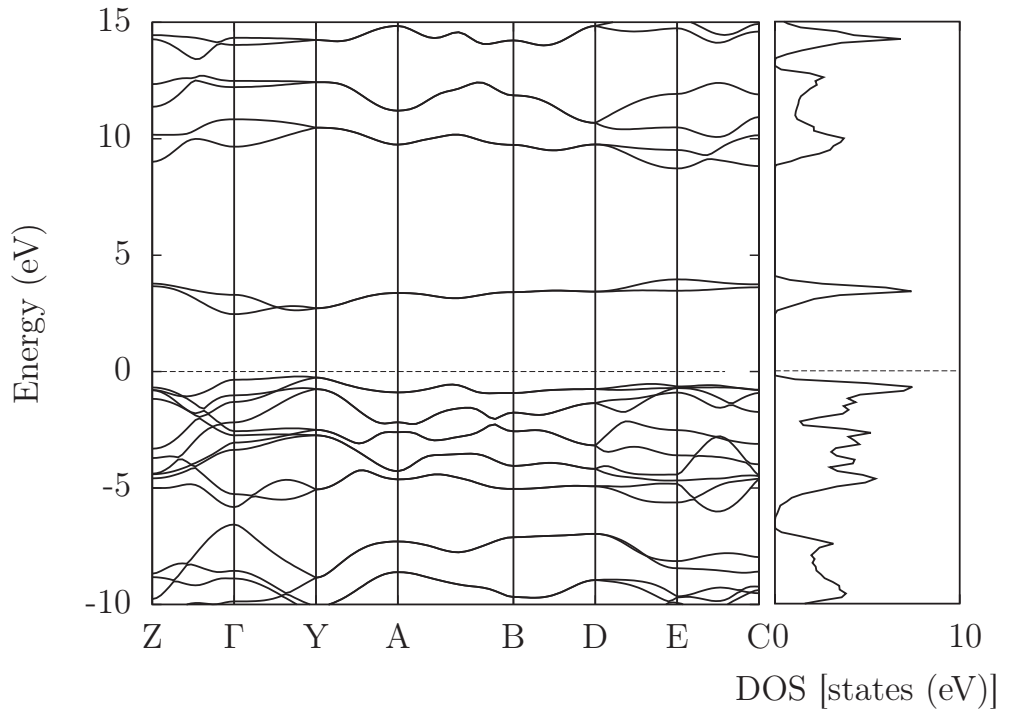

Figure 4.9 Band structure and density of states of the $P2_1/m$ phase of HNO_3 at 150 GPa.

electronic band structure and density of states, as shown in Fig. 4.9. It reveals that the $P2_1/m$ phase of HNO_3 is a semiconductor with a PBE band gap of 2.6 eV.

4.5 Conclusions

In summary, we explored the ternary phase diagram of the N–H–O system at high-pressure using a global structural prediction method combined with first-principle calculations. We found only two stable ternary phases up to 150 GPa, namely NOH_4 and HNO_3. The novel phase of NOH_4 possesses $C2/m$ symmetry while the new phase of HNO_3 has $P2_1/m$ symmetry. While the former composition becomes thermodynamically stable at 71 GPa, the $P2_1/m$ phase of HNO_3 is stabilized with respect to the phase II at pressures higher than 39 GPa. Both are layered systems, with the $C2/m$ phase of NOH_4 containing HO chains separated by NH_3-NH_3 "dumbbell clusters", and the $P2_1/m$ phase of HNO_3 composed of "quasi-clovers" with a H tail. These remarkable and unexpected structures are a consequence of the high-pressure affected bonding behavior of even simple elements. Our results can be viewed as a guide for further experimental synthesis of the ternary N–H–O system.

Chapter 5

Novel p-type transparent electrodes of ternary chalcogenides

5.1 Introduction

The delafossite mineral group is composed of ternary compounds with a general formula ABX_2. This crystal structure, named after the French crystallographer Gabriel Delafosse, has been known since the 19th century, but it started to be intensively studied after the discovery in 1997 of *p*-type electrical conductivity in a transparent thin-film of $CuAlO_2$ delafossite [188]. Transparent conductive materials (TCMs) possess two usually mutually exclusive characteristics which are transparency and conductivity. TCMs are now essential components of many modern technologies as they are used as transparent electrodes for optoelectronic device applications [189] (e.g., flat-panel displays and solar cells).

The atomic structure of delafossite crystals consists of planes of linearly coordinated A cations forming a triangular lattice, stacked between layers of flattened edge-sharing octahedra BO_6. The cation A is usually a noble metal like Cu, Ag, Pd or Pt; the cation B is typically a transition or group 13 element or a rare earth species; finally, the anion X is usually oxygen, although few delafossites with other anions can be found in material databases [190–192]. The trigonal delafossite structure (space group 166) is shown in the left panel of Fig. 5.1. A polytype of this structure with hexagonal symmetry (space group 194) can be formed when two neighboring A layers are stacked with each layer rotated by 180° in relation to one another. If A belongs to the IA group, one often finds another closely related trigonal structure (space group 164) with a slightly different stacking and where the layers are closer (see right panel of Fig. 5.1).

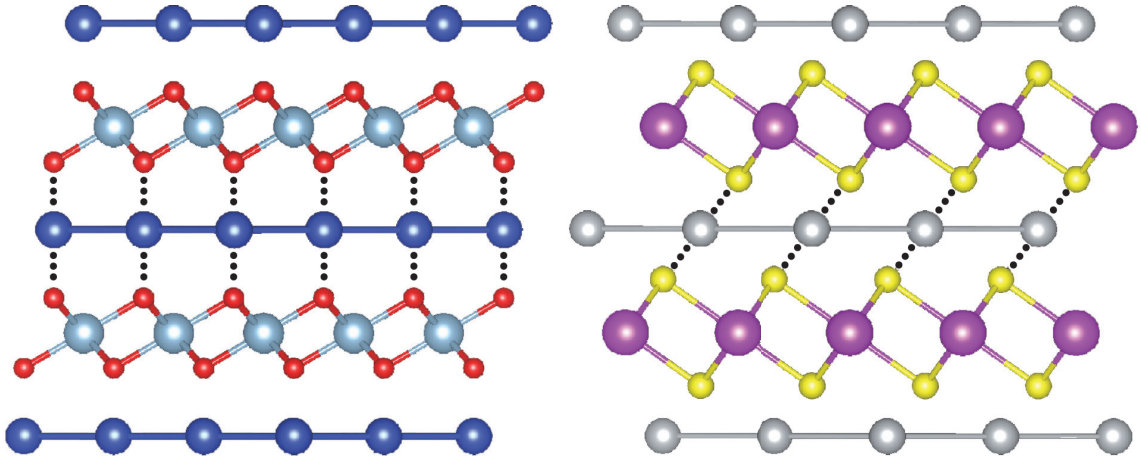

Figure 5.1 Left: Trigonal delafossite structure (space group 166) of $CuAlO_2$ (Cu dark blue, Al cyan, O red); Right: Trigonal structure (space group 164) of $AgBiS_2$ (Ag gray, Bi magenta, S yellow). From this perspective, there is no difference between this phase of $AgBiS_2$ and the trigonal (space group 166) structure of $TlScSe_2$. The A cations of ABX_2 form a triangular lattice that alternates with layers composed of distorted edge-sharing BX_6 octahedra. The similarity between the left and right panels is evident: only the alignment of A and X atoms differentiates the two structures (the dotted lines are a guide to the eye meant to emphasize this difference).

Due to the rather large range of possible stable configurations, it is not surprising that delafossites exhibit a significant richness in properties and potential applications. Several important technological applications have been proposed for members of this family, such as electrodes for hydrogen production by photo-electrochemical water splitting [193, 194], as luminescent materials [195], in solar cells [196–198], for thermoelectricity [199–202], as possible transparent superconductors [203], etc. Recently, it was also found that delafossite $PtCoO_2$ behaves like a nearly free-electron system, turning this surprising 5d transition-metal system in the most conductive oxide known [204].

The discovery of *p*-type conductivity in $CuAlO_2$ was particularly significant, as all technologically relevant transparent conducting oxides (TCOs), such as indium-tin-oxide (ITO) or Al- and Ga-doped ZnO (AZO and GZO), are *n*-type semiconductors. Unfortunately, neither $CuAlO_2$ nor other recently proposed *p*-type TCOs possess adequate conductivity and transparency for technological applications.

The reasons for the difficulty of finding good *p*-type TCOs are well understood and they are related to the strong localization of holes at the valence band edge of most oxides. In fact, the O-2*p* orbitals, which form hole transport paths at the top of the valence band of many oxides, are rather localized and generally much lower in energy than the valence orbitals of

the metal species. These two facts imply difficulties in hole doping and large hole effective masses (and therefore low hole mobilities).

In the race for obtaining such elusive material, delafossites have been widely explored for the past years. Getting inspiration from the structure/property relations in the delafossite family, Hosono and co-workers [205, 206] proposed few empirical rules for *p*-type TCOs, aiming at favoring at the same time large band gaps and dispersive top valence bands: (i) The A cations should possess closed *d* shells to prevent from absorbing light in the visible range. Optical transparency has also been associated with dipole forbidden transitions related to the linear O-A-O coordination motif. (ii) The energy levels of the A cations should overlap with the anion *p* levels (O 2*p*) to allow for strong hybridization at the top of the valence band. (iii) Hole paths should be favored, for example providing B states that can mix strongly with O 2*p* states into the valence band to build a A-O-B-O-A pathway.

Following Hosono's rules, the discovery of *p*-type conductivity in $CuAlO_2$ triggered the experimental and theoretical characterization of other delafossites [207–211] and of transparent *p*-*n* junctions. $CuCrO_2$ and $CuGaO_2$ are also *p*-type TCOs [212, 213]. $CuInO_2$ [214] is particularly interesting because it is amphoteric, i.e. it can be alternatively acceptor-doped or donor-doped. This ability is explained by the unique presence of two cationic environments in the delafossite structure: an octahedral indium environment that favors strong hybridization and *n*-type dopability, together with a linear copper environment that favors hybridization at the top valence and *p*-type doping [211]. Among delafossite compounds, $CuCr_{1-x}Mg_xO_2$ [215] possesses the highest conductivity of 220 S cm^{-1}, but transparency in the visible range is only about 30%, much smaller than for the traditional *n*-type TCOs. The recently synthesized Cu deficient $CuCrO_2$ has a conductivity in the range of 1–12 S cm^{-1} [216]. It was also claimed that the transparency can be improved by increasing the temperature, at the cost of higher resistivity [215, 217, 218]. Recently, A. Barnabé and co-workers studied Mg-doped $CuCrO_2$ thin films by using RF-sputtering [219]. They found that, at 600°C, the Mg-doped $CuCrO_2$ structure displayed an optical transmittance of only 63% in the visible range with, however, a conductivity of 1.6 S cm^{-1}.

Another idea, again put forward by Hosono and co-workers [220], is to replace oxygen with a chalcogen (S, Se, or Te) with more delocalized *p* orbitals. This has led to the synthesis of LaCuOS and LaCuOSe *p*-type oxides [221, 222]. Unfortunately, these latter compounds have either a too low mobility (LaCuOS) or a too small band gap (LaCuOSe). However, this strategy looks appealing as the *p* states of the chalcogen atoms are usually higher and therefore make the compound more prone to be *p*-doped. Recent calculations suggest that this is the case for $Ba(Cu,Ag)_2(S,Se)_2$ compounds [223].

Going beyond simple empirical rules, experimental databases have been recently explored by performing high-throughput *ab initio* calculations [224, 225] to single out compounds with large band gaps ($> 3\,\text{eV}$) and low effective masses. These previous investigations focused on oxides and showed that small hole effective masses are much rarer that small electron effective masses. Hautier *e*t al. [224] found that hole effective masses of 0.5–1.0 electron masses (m_e) in transparent oxides like $PbTiO_3$, $PbZrO_3$, $PbHfO_3$, $K_2Sn_2O_3$, and $Tl_4V_2O_7$ are due to the hybridization of the oxygen $2p$ orbitals with s states of Sn^{2+}, Pb^{2+}, Tl^{1+}. Similarly, hole effective masses smaller than 1.0 m_e and band gaps larger than 3.0 eV are reported by Sarmadian *e*t al. [225] for X_2SeO_2, with X = La, Pr, Nd, and Gd. Recently, Cerqueira *e*t al. [226] performed a search of new compounds of the form (Cu,Ag,Au)XO_2 by combining global structural prediction methods and high-throughput calculations. They showed that there are 45 new (quasi) stable phases in this system, some of which are candidate *p*-type transparent conductors. However, these new stable phases contain Ag and Au, which are not ideal elements for commercial applications.

We remind that finding a large band gap and low hole effective masses is not a sufficient condition for a good *p*-type TCO. In fact, another essential condition, much harder to translate to the minimization/maximization of a simple material property, is the *p*-type dopability of the system. As an example, we can think about ZnO: the hole effective mass values for ZnO range from 0.31 m_e to 0.59 m_e and its band gap is about 3.5 eV. Despite these ideal parameters, numerous attempts to produce *p*-type doped ZnO have failed [211].

It appears by now clear that if we work only with known materials it will be very hard to improve both transparency and conductivity to technologically acceptable limits. However, the search for improved *p*-type TCMs remains an important open question. Fortunately, we only know experimentally a fraction of all possible stable compounds. Delafossite structures, which combine the advantages of linear and octahedral environments for the two cations remain particularly attractive for *p*-type TCMs and ambipolar doping. We therefore asked ourselves: Are there more delafossite compounds that wait to be synthesized and characterized? And more precisely: can good *p*-type TCMs be found in the delafossite family or should we resign ourselves and direct future search towards completely different crystal families?

Here we provide an answer to the questions above by performing a comprehensive first-principles investigation of ABX_2 systems that may crystallize in the delafossite structure. We extend in fact our study to all ABX_2 compositions where A and B cover the periodic table from H to Bi (excluding the rare gases and the lanthanides) and X is a chalcogen (O, S, Se, and Te). This set contains $63 \times 62 \times 4 = 15\,624$ compositions and includes the already known delafossites crystals. At this point, we take all A and B elements and do not make any

bias towards non-toxic or abundant elements. Such filtering can however be easily performed *a posteriori*.

We note that most research on delafossites is restricted to oxide materials. Also most of the systems known have X=O. For example, the materials project database [190], contains 90 trigonal ABX_2 oxides (with space group 166) while only 23 sulfides, 10 selenides and 7 tellurides. It is unclear if this is because the delafossite structure prefers the highly electronegative oxygen, or if it simply reflects a bias against sulfides, selenides, and tellurides.

To screen the large amount of possible compositions of ABX_2 compounds, we use a combination of high-throughput density-functional theory [227] and global structural prediction methods [228]. This two-step process is essential to ensure that our predicted structures are (i) thermodynamically stable, i.e. that do not decompose to other more stable species, and (ii) are indeed delafossites, i.e. that there are no other lower energy phases for the given composition. The resulting stable delafossite phases are then characterized theoretically using state-of-the-art *ab initio* methods. The final results provide precious indications for further experimental synthesis and open the way for more specific theoretical and experimental studies of dopability and transport properties, which can be restricted only to the most interesting candidates.

5.2 Methods

As starting prototype unit cell we used the rhombohedral (space group 166) delafossite structure, and not the hexagonal (space group 194) one. In fact, these two layered phases only differ in the stacking of the layers, and we have verified [226] that they exhibit very similar total energies (with differences of the order of few meV/atom) and electronic properties. In that sense these two crystal structures are equivalent in our calculations. However, the former contains 4 atoms in the primitive unit cell, while the latter contains 8, which would lead to a considerable increase of the computational burden of our high-throughput search.

As the A and B atoms are in the inequivalent crystallographic positions 1*a* and 1*b* of the delafossite structure, there are 15 624 possible ABX_2 compositions that combine the 64 chemical elements considered here. It is true that this number could be quite reduced by eliminating compositions on the basis of empirical rules based on oxidation states or the radius of the A, B, and X elements. However, we decided not to follow this path in order to allow for delafossites that do not conform to our intuition.

For each one of these structures we optimized the geometry and calculated the total energy. This was done within *ab initio* density functional theory as implemented in the computer code VASP [229, 230]. All parameters were set to guarantee compatibility with the data

available in the materials project database [190] and open quantum materials database [191]. We used the PAW [231] datasets of version 5.2 with a cutoff of 520 eV and Γ-centered *k*-point grids, as dense as required to ensure an accuracy of 2 meV/atom in the total energy. All forces were converged to better than 0.005 eV/Å. We followed the same protocol as in Ref. [226]: spin-polarized calculation using the Perdew-Burke-Ernzerhof [25] (PBE) exchange-correlation functional, with the exception of oxides and fluorides containing Co, Cr, Fe, Mn, Mo, Ni, V, W, where an on-site Coulomb repulsive interaction U with a value of 3.32, 3.7, 5.3, 3.9, 4,38, 6.2, 3.25, and 6.2 eV, respectively, was added to correct the *d*-states. We are of course aware that the PBE (+U) functional is not always able to determine the correct electronic and spin ground-state. Moreover, it is well-known that the PBE, as well as many other exchange correlation functionals, including hybrid functionals [232], yield an average error for the energies of formation substantially larger than the so-called chemical accuracy (around 1 kcal/mol $\simeq$ 43 meV) [233]. Nevertheless, the optimized crystal structure and the ordering of low-energy phases, resulting from differences of formation energies, is very often qualitatively and quantitatively good within PBE (+U), even in many cases in which the electronic states are not correctly described.

The second step of our search is to identify which compositions are thermodynamically stable (see Chapter 2 for more details). We worked always at zero temperature and pressure, and we neglected the effects of the zero point motion of the phonons (that are expected to be negligible for these materials). In this case, the thermodynamic quantity of interest is the total energy. Fortunately, it is no longer necessary to calculate the total energy of all possible reservoir compounds, as this information is already available in excellent public databases, such as the materials project [190], open quantum materials database, [191] and the ab-initio electronic structure library AFLOWLIB [192]. We chose to use the materials project database for our reference energies, and to determine the distances to the convex hull of stability with PYMATGEN [234]. The materials project database includes most of the experimentally known inorganic crystals that are present in the ICSD database [235, 236] and an increasing number of theoretically predicted phases, including those proposed in Ref. [226]. Note that, as we only use the compounds included in the database to build the convex hull, new materials will appear with negative distances to the hull.

The next step is to perform global structural prediction runs for the most stable structures stemming from the high-throughput runs. There are several good algorithms available in the market for this task. Our method of choice is the minima hopping method (see Chapter 2).

Having in mind the possible final application as TCM, for a first characterization of the structures we determined hole effective masses and band gaps. For the calculation of effective masses we used the same framework as for the calculation of the total energies, that relies on

the PBE functional. Effective masses were calculated with the program BOLTZTRAP [237] for a concentration of 10^{18} cm^{-3} and a temperature of 300 K. We remark that while it is clearly desirable to have dispersive valence bands close to the band gap to ensure high hole mobilities, this is not the only possibility as other transport mechanisms, e.g., based on small polarons, have been proposed for delafossite *p*-type TCOs [211].

Although the PBE functional is a quite reasonable approximation for the curvature of the bands, it is well known that this functional underestimates considerably the band gaps. Therefore we decided to adopt the hybrid exchange-correlation functional of Heyd, Scuseria, and Ernzerhof (HSE06) [46] to obtain reliable band gaps.

Finally, we give a first estimate of the *p*-type dopability by testing if acceptor-like defects can be easily formed in the system and whether one can expect or not the generation of compensating native defects (e.g., anion vacancies). To this purpose, a simple criterion with significant predictive power is the determination of the branch point energy. The branch point energy [225, 238, 239], or charge neutrality level, is defined as the energy at which the defect states induced in the gap change their character from predominantly donor-like to acceptor-like. The position of this energy with respect to the band edges is particularly important as the formation of acceptor (donor) defect states in the gap becomes favorable above (below) it. Hence, in a material with a branch point energy lying in the conduction band (such as ZnO) or high in the band gap, donor impurity defects tend to be shallow, while acceptor impurities, if they can exist, will be necessarily deep. The condition to favor *p*-type doping is therefore to have the branch point energy at least in the middle of the gap. In general, the lower the value of this energy the easier *p*-type doping can be expected. To calculate this quantity we follow Schleife *e*t al. [238] and we define it as a weighted average of the mid-gap energies (calculated with a hybrid HSE06 functional) over the Brillouin zone. The number of valence and conduction states included in the calculation follows the prescription of Ref. [238], which has already been adopted in other works [225, 239]. This method is a particularly convenient criterion to use in high-throughput calculations as it only requires the energy levels of the perfect crystals. We note, however, that reliable conclusions on the *p*-type dopability of the system can be obtained only by performing extensive defect calculations.

Crystal structures were visualized with VESTA [240].

Table 5.1 Common prototype structures for the composition ABX_2 used in this study. We list the space group (spg) number, the number of atoms in the unit cell, and an example of a composition that crystallizes in the phase.

spg	# atoms	example
166	4	$CuAlO_2$
122	8	$CuInSe_2$
62	16	$CaBaO_2$
14	16	$CuBrTe_2$
15	8	$KFeSe_2$
141	8	$CuGaSe_2$
12	4	$NaCuO_2$
63	8	$CuSrO_2$
15	32	$KAlTe_2$
140	8	$KAlTe_2$
160	4	$CuAsSe_2$
33	16	$LiAlSe_2$
123	4	$AgSbTe_2$
9	8	$AgInSe_2$
156	4	$AgAlS_2$

5.3 Results and discussion

5.3.1 Overview

The main results of our high-throughput search are summarized in the stability maps of Fig. 5.2, where we plot the distance to the convex hull of the delafossite phase for all the compositions studied here. In order to put into evidence the chemical similarity between the chemical elements, we order them using an optimized [241] Pettifor scale [242]. Each point in the plots corresponds to a different compound, and the color code is used to indicate the distance to the convex hull of stability (light green – stable, red – unstable). It is quite evident that the large majority of the compositions are highly unstable in the delafossite phase, with distances to the hull larger than 400 meV/atom. However, there are still many systems that are either thermodynamically stable or close to stability.

We then filter this list using a threshold of 50 meV/atom above the convex hull. This is a rather conservative threshold, that tries to minimize the number of false positives, but at the same time takes into account the errors in evaluating differences of PBE energies [233] and the possible reduction of the energy of formation related to small distortions of the lattice, native defects, temperature and disorder, etc. This also allows us to include in our list some

experimentally known delafossite structures that exhibit (small) positive distances to the hull in our formalism, such as $CuInO_2$ (7 meV/atom).

Within this threshold we find 285 compositions (109 oxides, 66 sulfides, 67 selenides, and 43 tellurides). We can find entries in the materials project database for 101 of the 285 compositions, namely for 72 oxides (including our predictions of Ref. [226], 11 sulfides, 11 selenides, and 7 tellurides. Obviously, there are many more entries ABX_2 with X=O, S, Se, Te in the materials project database (463 in total at the time of writing), but most of these, such as, e.g., the chalcopyrites, have atomic arrangements very different from the delafossites, and do not appear therefore as a result of our search. We could also find in literature some (unfortunately incomplete) information on other compounds that are not part of the materials project database: $MgNiO_2$, $PdCrO_2$ [243, 244], $PdRhO_2$ [244], $KBiS_2$ [245], $KScS_2$[246], KYS_2[246], $RbScS_2$[246], $AgRhS_2$[247], $AgYS_2$[248], $HgTiS_2$[249], $TlMnS_2$ [250], $TlMnSe_2$ [250], $KCrSe_2$ [251], $CsBiTe_2$[252], $TlYTe_2$ [253]. The fact that we also identify these compounds as thermodynamically stable is another confirmation of the validity of our approach.

It is quite interesting to compare these numbers at this stage. First, they indicate that there are probably many more stable ternary compounds than the ones known experimentally (or predicted theoretically and already present in the databases). Second, we can see the strong experimental bias towards oxides in detriment of other chalcogenides.

Up to now, we only know that the delafossite phase is stable (or almost) regarding decomposition into other compounds. The following step in our investigation is to evaluate if the delafossite phase is indeed the ground-state structure, or if there exist other phases lower in energy. We combined two different approaches for all stoichiometries that did not already appear in the materials project database: (i) We tested a set of common prototype structures for the composition ABX_2 (see Table 5.1). This amounts to 28 further structural optimizations per composition. (ii) For each composition, we performed two independent structural prediction runs including 8 atoms (2 formula units) in the unit cell. The length of each run was tuned in order to obtain $\sim$50 minima.

Our final step consists in filtering again the results and characterizing the remaining materials. We retain only the stoichiometries that are thermodynamically stable or slightly unstable (up to 25 meV/atom above the convex hull, which corresponds approximately to room temperature), and whose ground state structure is a delafossite or a closely related structure. We define as closely related structure a crystal structure that maintains the essential characteristics of the delafossite: the presence of both a linear and an octahedral environment for the two cations. Note however, that the linear and octahedral coordinations can be significantly distorted in some quasi-delafossites. For these structures we finally calculate

indirect and direct band gaps, magnetic moments per formula unit and hole effective masses whenever the system is non-metallic. Our results concerning all new structures, i.e. the ones *not already present* in the materials project database, are summarized in Tables 5.2, 5.3, 5.4, 5.5, 5.6, 5.7 and 5.8. For completeness, we decided to also include the information concerning the phases reported in the literature but not present in the materials project database. These can be found in bold in the tables. All crystallographic information files are given as Appendix A.

We can observe that there are 79 delafossite systems that are stable (and 123 close to stability). The tables include 16 (10) new oxides, 40 (27) sulfides, 38 (25) selenides, and 29 (17) tellurides. (The numbers in parentheses are the number of phases strictly below the hull of stability). The list includes a series of rather exotic systems that depart from the usual $A^{+}B^{+3}X_2^{-2}$ oxidation states of the delafossites. Actually, we do find often an element of the IA group (Li, Na, K, Rb, or Cs) or IB group (Cu, Ag, Au) in position A. However many other possibilities appear such as Hg, In, Tl, Bi, or even halogens such as Br or I.

Most of the new stable compositions crystallize either in the trigonal delafossite structure of, e.g., $CuAlO_2$, or in the closely related trigonal structures (see Fig. 5.1) of, e.g., $AgBiS_2$ (space group 164) or $TlScSe_2$ (space group 166). However, we also find a variety of structures showing small distortions or different stacking patterns in comparison to the standard delafossite arrangement. We will now discuss in detail our results separately for oxides, sulfides, selenides, and tellurides.

5.3.2 ABO_2

Among the 3906 possible delafossite oxides (compatible with our selection of chemical elements) there are 93 phases that within appear at least 25 meV/atom below the convex hull of stability. Of these, 77 can already be found in the materials project database [190] or in Ref. [226]. The remaining 16 compositions are reported in Table 5.2.

All compounds with A=Pd, Pt, Hg, Tl, and Br crystallize in the delafossite structure with space group 166. The only exception is $BrLaO_2$ where the stacking is slightly changed, leading to a monoclinic ground-state (prototype of $NaCuO_2$) which is 14 meV/atom lower in energy than the trigonal delafossite phase. On the other hand, when A is an alkali or an alkali earth metal, the ground-state phase has the trigonal structure of $TlScSe_2$ (space group 166), that is very similar to the trigonal structure of $AgBiS_2$ (space group 164) shown in the right panel of Fig. 5.1.

The crystals $KInO_2$, $RbInO_2$, $RbRhO_2$, $CsLaO_2$, $HgMgO_2$, and $BrLaO_2$ are semiconductors with gaps between 3 and 4 eV, and not too large effective masses of around 2 m_e (with the notable exception of $RbRhO_2$). We note that hole effective masses of $1\sim2$ m_e are not

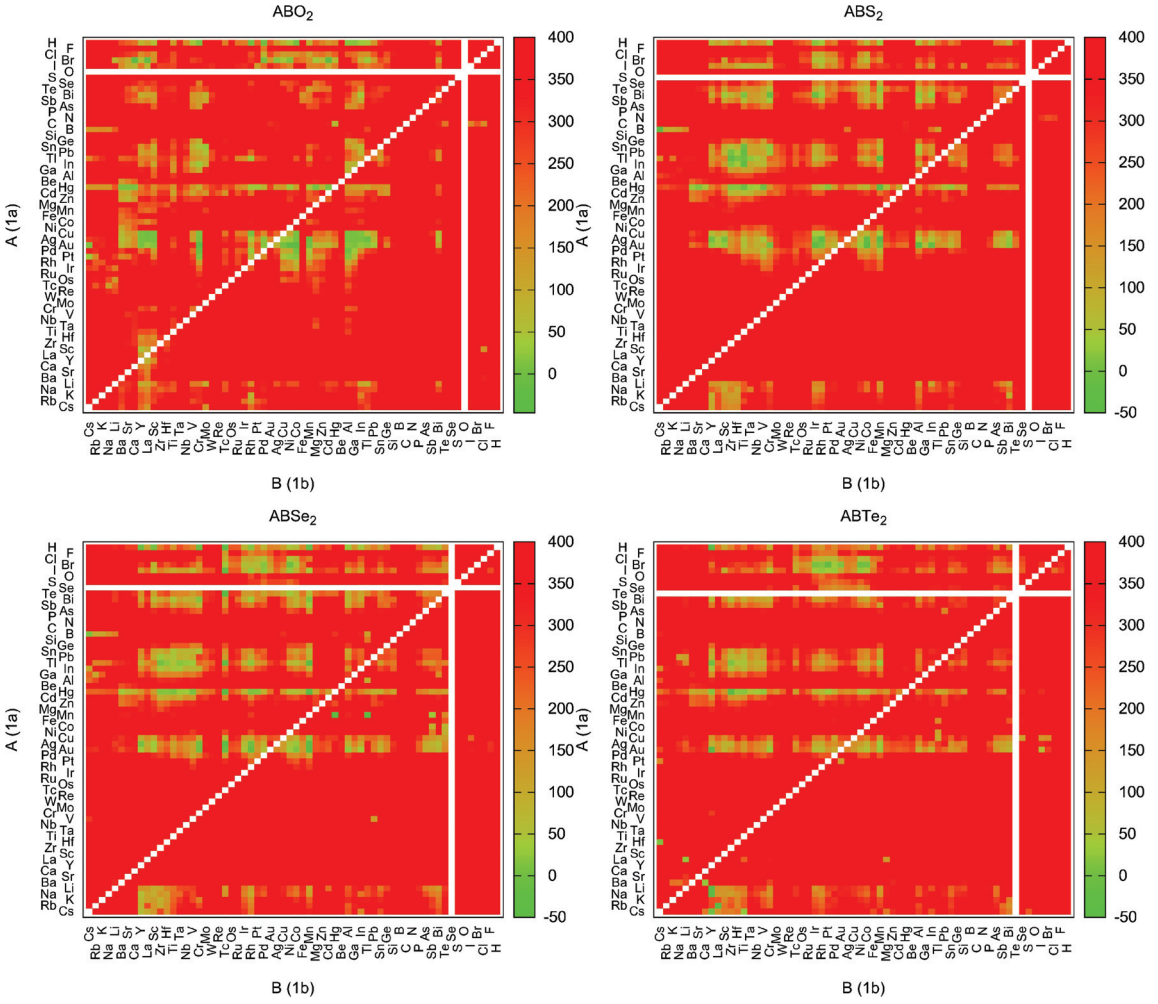

Figure 5.2 Stability maps for ABO_2, ABS_2, $ABSe_2$ and $ABTe_2$. The colors indicate the distance to the convex hull of stability (in meV per atom), with green meaning that the composition is thermodynamically stable. The order of the elements along both axes follows an optimized Pettifor scale.

Table 5.2 Distance to the convex hull (E_{hull} in meV/atom), HSE06 gaps (indirect and direct in eV), average hole effective mass for the semiconducting phases (m_h^* in m_e), magnetic moment per formula unit (μ in bohr magnetons, and space group (spg) of the new (quasi) stable delafossite and closely related phases with composition ABO_2. The compounds that are not in the materials project database, but that are reported in literature are indicated in bold. [a]See left panel of Fig. 5.1. [b]See right panel of Fig. 5.1.

Structure	E_{hull}	$E_{\text{Gap}}^{\text{ind}}$	$E_{\text{Gap}}^{\text{dir}}$	m_h^*	μ	spg
$KInO_2$	-106	3.49	3.63	2.71	0	166[b]
$RbInO_2$	-27	3.38	3.57	2.68	0	166[b]
$RbRhO_2$	-185	3.06	3.49	34.84	0	166[b]
$CsLaO_2$	-44	4.10	4.15	2.16	0	166[b]
$MgNiO_2$	-4	0	0	-	2.0	166[b]
$PdAlO_2$	-7	0	0	-	0	166[a]
$PdCrO_2$	-12	0	0	-	3.0	166[a]
$PdRhO_2$	22	0	0	-	0	166[a]
$PtAlO_2$	12	0	0	-	0	166[a]
$PtNiO_2$	17	0	0	-	1.0	166[a]
$HgMgO_2$	0	3.25	3.77	2.39	0	166[a]
$TlRhO_2$	23	0	0	-	0	166[a]
$BrCdO_2$	-29	0	0	-	0	166[a]
$BrLaO_2$	-13	3.92	4.59	2.23	0	12[a]
$BrNiO_2$	14	0	0	-	1.4	166[a]
$BrTlO_2$	24	0	0	-	0	166[a]

small in absolute terms, but they are comparable with those of $CuAlO_2$ and $CuCrO_2$. Among the metals, the compounds containing Ni and Cr are magnetic, with a total magnetization that can reach 3.0 bohr magnetons for the ferromagnetic compound $PdCrO_2$.

5.3.3 ABS_2

Among all the stable sulfides that we found in this work, only 10 compositions could be found in the materials project database [190]. These are $NaScS_2$, $NaInS_2$, $KCrS_2$, $KLaS_2$, $RbYS_2$, $CsLaS_2$, $AgBiS_2$, $AuCrS_2$, $TlBS_2$, and $TlInS_2$. All the other novel 40 compositions can be found in Tables 5.3 and 5.4. There are 6 systems with A=Ag and 9 with A=Au, however we did not find any new system with A=Cu. Most of these have the standard delafossite structure with the exception of $AgScS_2$ and $AgYS_2$ that exhibit a different stacking of the layers (space group 160 and 156 respectively). We also find 5 systems with A=Hg, 4 with A=Bi, 4 with A=Tl, and 3 with A=Pb. Interestingly, we also find a couple of delafossites with trivalent In and tetravalent Sn in the Wyckoff 1a position. Finally, there are a series of

Table 5.3 Properties of delafossite sulfides ABS_2. For an explanation see caption of Table 5.2.

Structure	E_{hull}	$E_{\text{Gap}}^{\text{ind}}$	$E_{\text{Gap}}^{\text{dir}}$	m_h^*	μ	spg
$HIrS_2$	0	2.49	2.81	1.13	0	160
$KBiS_2$	-184	2.14	2.53	5.09	0	166[b]
$KScS_2$	-158	2.89	3.72	1.20	0	166[b]
KYS_2	-194	3.37	4.14	1.23	0	166[b]
$RbScS_2$	-137	2.88	3.69	1.29	0	166[b]
$AgCoS_2$	-22	1.29	2.50	1.77	0	166[a]
$AgMnS_2$	-53	0	0	-	2.1	166[a]
$AgRhS_2$	-26	1.69	2.19	1.35	0	166[a]
$AgScS_2$	-3	2.29	3.06	0.66	0	160
$AgIrS_2$	11	1.87	2.16	0.87	0	166[a]
$AgYS_2$	-15	3.16	3.24	0.71	0	156
$AuAlS_2$	-29	2.72	2.97	0.65	0	166[a]
$AuBiS_2$	20	1.35	2.28	0.93	0	166[a]
$AuCoS_2$	-48	1.36	2.68	1.19	0	166[a]
$AuInS_2$	-13	1.70	1.95	0.68	0	166[a]
$AuIrS_2$	-23	2.13	2.52	0.83	0	166[a]
$AuMnS_2$	-41	0	0	-	2.0	166[a]
$AuRhS_2$	-54	1.72	2.39	1.19	0	166[a]
$AuScS_2$	24	2.28	3.14	0.52	0	166[a]
$AuYS_2$	23	2.95	3.68	0.62	0	166[a]

systems with an alkali in the 1a position, all assuming the trigonal lattice depicted in Fig. 5.1. The only systems that do not crystallize in one of the structures of Fig. 5.1 are $HIrS_2$ and $HgTiS_2$. While the former just exhibits a different stacking, in the latter Hg forms layers with square and not hexagonal symmetry.

Many of the novel systems are semiconducting with indirect band gaps varying in the rather large range of 0.7–3.4 eV. Hole effective masses, as expected considering the more delocalized nature of S *p* states, are significantly lower than in oxides. We would like to point out materials like (K,Rb)YS_2, composed of relatively abundant elements, with rather large band gaps of the same order of magnitude as the usual Cu delafossite TCOs, and with rather small hole effective masses (of the order of 1.2–1.3 m_e), if compared to $CuAlO_2$. $AgYS_2$, with an HSE band gap of 3.16 eV and a hole effective mass of 0.71 m_e, is the best system identified in this study. Again, stable metals with Cr or Mn in the 1b position are magnetic with relatively large magnetization.

Table 5.4 Properties of delafossite sulfides ABS_2. Continuation of Table. 5.3. For an explanation see caption of Table 5.2.

Structure	E_{hull}	$E_{\text{Gap}}^{\text{ind}}$	$E_{\text{Gap}}^{\text{dir}}$	m_h^*	μ	spg
$HgHfS_2$	14	0.79	1.34	-	2.4	166^b
$HgMnS_2$	-36	0	0	-	3.0	166^a
$HgPtS_2$	16	1.24	1.42	0.71	0	166^b
$HgTiS_2$	-14	0	0	-	0	1
$HgZrS_2$	11	0.66	1.12	0.19	0	166^b
$BiAlS_2$	23	0	0	-	0	166^a
$BiCrS_2$	-7	0	0	-	3.0	166^a
$BiTiS_2$	6	0	0	-	0	166^a
$BiIrS_2$	-5	0	0	-	0	166^a
$InTiS_2$	-25	0	0	-	0	166^a
$InZrS_2$	9	0	0	-	0	164^a
$TlHfS_2$	-5	0	0	-	0	164^a
$TlMnS_2$	-33	0	0	-	2.6	166^{a*}
$TlTiS_2$	-21	0	0	-	0	164^a
$TlZrS_2$	-43	0	0	-	0	164^a
$SnCrS_2$	24	0	0	-	2.8	166^a
$SnTiS_2$	-4	0	0	-	0	166^a
$PbCrS_2$	25	0	0	-	2.8	166^a
$PbTiS_2$	-16	0	0	-	0	166^a
$PbZrS_2$	5	0	0	-	0	166^a

* The ground-state of $TlMnS_2$ has space group number 15. The delafossite structure is only 10 meV/atom above this phase.

5.3.4 $ABSe_2$

For the selenides $ABSe_2$ we find 48 phases below 25 meV/atom, 10 of which can be found in the materials project database. The results for the remaining 38 phases can be found in Tables 5.5 and 5.6. For the compounds with a IA element in the 1a Wyckoff position we find that stable compounds tend to have larger alkalis (Rb, Cs) in detriment of the lighter ones (Na, K). The same does not seem to happen with the IB group, and we can observe several compounds containing S and Se together with both Ag and Au. We also witness the appearance of the rather exotic $INiSe_2$ at the limit of our threshold of 25 meV/atom.

Again most of the compounds crystallize in one of the structures of Fig. 5.1, with the following exceptions: $HScSe_2$ has a monoclinic ground-state structure where the layers of H are buckled; $HgTiSe_2$, like other Hg compounds, has Hg layers with square symmetry;

Table 5.5 Properties of the delafossite selenides $ABSe_2$. For an explanation see caption of Table 5.2.

Structure	E_{hull}	$E_{\text{Gap}}^{\text{ind}}$	$E_{\text{Gap}}^{\text{dir}}$	m_h^*	μ	ΔE_{GS}
$HMnSe_2$	-15	0	0	-	4.0	166^{a*}
$HScSe_2$	-15	2.28	2.51	0.97	0	11
$KCrSe_2$	-83	0	0	-	3.0	166^b
$KScSe_2$	-157	2.37	3.11	0.98	0	166^b
$KRhSe_2$	-94	1.82	1.87	1.38	0	166^b
$KYSe_2$	-203	2.85	3.72	1.00	0	166^b
$RbScSe_2$	-141	2.40	3.13	1.03	0	166^b
$RbRhSe_2$	-80	1.78	1.92	1.26	0	166^b
$CsScSe_2$	-142	2.30	2.97	1.10	0	166^b
$CsLaSe_2$	-159	3.00	3.32	1.45	0	166^b
$CsRhSe_2$	-72	1.76	1.84	1.13	0	166^b
$CsYSe_2$	-206	2.74	3.45	1.10	0	166^b
$AgMnSe_2$	-54	0.64	0.84	-	4.0	166^b
$AgRhSe_2$	-1	0.97	1.73	0.30	0	166^a
$AuCoSe_2$	15	0.60	1.86	-	0	166^a
$AuCrSe_2$	2	0	0	-	3.0	166^a
$AuMnSe_2$	-44	0	0	-	4.0	166^a
$AuRhSe_2$	-13	1.01	1.99	0.08	0	166^a
$HgHfSe_2$	12	1.06	1.40	3.51	0	166^b
$HgMnSe_2$	-67	0	0	-	2.9	166^b

* The ground-state of $HMnSe_2$ has space group number 8. The delafossite structure is 8 meV/atom above this phase.

In $HgVSe_2$ we find a different stacking of the layers leading to a monoclinic ground-state; $HgNbSe_2$ and $TlVSe_2$ present BSe_2 layers that are distorted with respect to the usual delafossite structure; Finally, $SbMnSe_2$ has buckled Sb planes.

We again obtain the usual mixture of metals and semiconductors, although, and as expected, with gaps generally smaller than for the sulfides. Compounds including Cr and Mn are magnetic, but $AuCoSe_2$, $BrNiSe_2$, and $INiSe_2$ are non-magnetic.

5.3.5 $ABTe_2$

From the systems found in our search, there are only 7 $ABTe_2$ phases in the material project database. These structures are $AgSbTe_2$, $AgBiTe_2$, $KLaTe_2$, $KYTe_2$, $TlSbTe_2$, $TlScTe_2$ and $TlBiTe_2$. Besides these known tellurides, we identify 29 new phases that are stable or very

Table 5.6 Properties of the delafossite selenides $ABSe_2$. Continuation of Table 5.5. For an explanation see caption of Table 5.2.

Structure	E_{hull}	$E_{\text{Gap}}^{\text{ind}}$	$E_{\text{Gap}}^{\text{dir}}$	m_h^*	μ	ΔE_{GS}
$HgNbSe_2$	0	0	0	-	0	38
$HgPtSe_2$	14	1.28	1.66	0.90	0	166^b
$HgRhSe_2$	13	0	0	-	0	166^a
$HgTiSe_2$	1	0	0	-	0	1
$HgVSe_2$	-7	0	0	-	0	6
$HgZrSe_2$	11	0	0	1.46	0	166^b
$InZrSe_2$	17	0	0	-	0	164^b
$TlHfSe_2$	1	0	0	-	0	164^b
$TlMnSe_2$	-98	0	0	-	4.0	166^b
$TlRhSe_2$	-63	0	0	-	0	164^b
$TlTiSe_2$	23	0	0	-	0	164^b
$TlVSe_2$	-7	0	0	-	0	187
$TlZrSe_2$	-40	0	0	-	0	164^b
$SbMnSe_2$	-4	0	0	-	4.0	11
$BiCrSe_2$	17	0	0	-	3.0	166^a
$BiMnSe_2$	12	0	0	-	3.7	166^a
$BrNiSe_2$	-2	0	0	-	0	$166^{a\dagger}$
$INiSe_2$	25	0	0	-	0	166^a

† The ground-state of $BrNiSe_2$ has space group number 2. The delafossite structure is 22 meV/atom above this phase.

close to stability (see Tables 5.7 and 5.8). As expected by the chemical similarity between Se and Te, the situation here is analogous to what was described for the Se systems. Perhaps the biggest difference regards the chalcogen in the Wyckoff position 1a. We find a series of Br and I metallic compounds with the 1b position occupied by a transition metal. Some of these systems, like $BrPtTe_2$, are quite below the convex hull of stability, which, together with the overall consistency of the results, makes us believe that these exotic systems can be experimentally synthesized.

From the compositions that do not crystallize in the structures of Fig. 5.1 we have: $HgVTe_2$, with displays distorted planes; $BrIrTe_2$ with has a different stacking; $BrPdTe_2$ with distorted Br layers; finally $INiTe_2$ and $IPdTe_2$ have a different stacking.

The two compounds with Mn in the 1b position are ferromagnetic, but, more surprisingly, we also find that $HgVTe_2$ are $TlTiTe_2$ have a relatively small magnetic moment. For the

Table 5.7 Properties of the delafossite tellurides $ABTe_2$. For an explanation see caption of Table 5.2.

Structure	E_{hull}	$E_{\text{Gap}}^{\text{ind}}$	$E_{\text{Gap}}^{\text{dir}}$	m_h^*	μ	ΔE_{GS}
$LiYTe_2$	-265	1.56	2.48	0.61	0	164^b
$NaYTe_2$	-314	1.89	2.94	0.84	0	166^b
$RbLaTe_2$	-108	2.30	2.87	1.10	0	166^b
$CsBiTe_2$	-68	1.57	1.75	1.18	0	166^b
$CsHfTe_2$	12	0	0	-	0	166^b
$CsScTe_2$	-70	1.64	2.20	0.77	0	166^b
$CsYTe_2$	-268	2.03	2.76	0.80	0	166^b
$BaCaTe_2$	25	2.26	2.94	0.58	0	166^b
$AgMnTe_2$	-4	0.01	0.28	-	4.0	166^{b*}
$HgHfTe_2$	10	0	0	-	0	166^b
$HgTiTe_2$	7	0	0	-	0	166^b
$HgVTe_2$	9	0	0	-	1.2	11
$HgZrTe_2$	-65	0	0	0	0	166^b
$InYTe_2$	-169	0.50	1.44	-	0	166^b
$TlHfTe_2$	-3	0	0	-	0	164^b

* The ground-state of $AgMnTe_2$ has space group number 72. The trigonal structure is 8 meV/atom above this phase.

semiconducting compounds there is also a further decrease of the magnitude of the gap with respect to the selenides.

5.3.6 Gaps and hole effective masses

Finally, Fig. 5.3 is a scatter plot of the direct band gap and the average hole effective mass for all delafossite-like compounds within our window of stability. We include both the new systems found in this work, as well as the other compounds from the materials project database (such as $CuAlO_2$, $CuGaO_2$, $RbYO_2$, $AgYO_2$, etc.), and the Cu, Ag, and Au oxides from Ref. [226]. Such a plot allows us to quickly recognize potential outliers for *p*-type transparent conductors. In particular, we are interested in compounds in the lower central part of the plot, with a band-gap larger than the visible range and a small hole mass. We chose to plot the direct band gap, as this is the one most directly related to optical absorption. The numbers were calculated with the HSE06 approximation to the xc potential of DFT, that usually gives accurate gaps. We should keep in mind, however, that HSE underestimates systematically the band gap of medium-large gap semiconductors. Moreover, some of

Table 5.8 Properties of the delafossite tellurides $ABTe_2$. Continuation of Table 5.7. For an explanation see caption of Table 5.2.

Structure	E_{hull}	$E_{\text{Gap}}^{\text{ind}}$	$E_{\text{Gap}}^{\text{dir}}$	m_h^*	μ	ΔE_{GS}
$TlMnTe_2$	-47	0	0	-	4.0	164^b
$TlTiTe_2$	4	0	0	-	0.4	164^b
$TlYTe_2$	-230	1.20	2.05	0.24	0	166^b
$TlZrTe_2$	-59	0	0	-	0	164^b
$BrCoTe_2$	2	0	0	-	0	166^a
$BrIrTe_2$	-4	0.92	1.72	1.48	0	160
$BrNiTe_2$	-30	0	0	-	0	166^b
$BrPdTe_2$	18	0	0	-	0	12
$BrPtTe_2$	-68	0	0	-	0	166^b
$BrRhTe_2$	16	0	0	-	0	166^a
$INiTe_2$	8	0	0	-	0	13
$IPdTe_2$	14	0	0	-	0	12
$IPtTe_2$	-8	0	0	-	0	166^b
$IRhTe_2$	25	0	0	-	0	166^a

these materials can have substantial quasi-particle corrections and large excitonic binding-energies [254, 255]. The hole masses discussed here, on the other hand, are averaged values, and may not include all the physics in cases of valence bands with multiple valleys.

We also label a few relevant points in Fig 5.3, such as $CuAlO_2$ and $CuGaO_2$. It is evident, for example, that $CuAlO_2$, synthesized for the first time in 1997 [188], possesses a large band gap of around 3.37 eV (in good agreement with the experimental value of 3.53 eV [256]), but has a relatively high hole effective mass ($\approx$2.5). We can observe several new phases that possess a sufficiently large band gap and a smaller hole effective mass. These phases are not only oxides, but also sulfides, and few selenides and tellurides. For example, some candidate *p*-type TCO systems are $BrLaO_2$ (gap 3.92 eV, hole mass 2.23), $CsLaO_2$ (gap 4.11 eV, hole mass 2.16), KYS_2 (gap 3.37 eV, hole mass 1.23), $AgYS_2$ (gap 3.16 eV, hole mass 0.71).

Looking at the branch point energies of these candidates, we found a similar behavior for all of them, with values that lie in the middle of the HSE band gap, at distances of 1.4–1.9 eV from the lowest conduction band. The fact that the branch point energy is not close to or within the conduction band is good news, as this would imply that *p*-type doping is very difficult (as in the case of ZnO). However, this result does not allow to conclude that it is possible to *p*-dope these materials. When the branch point energy is in the middle of the gap all scenarios are in fact open: the compound may be *p*- or *n*-type dopable, or even ambipolar. Accurate defect calculations are then the only safe way to draw reliable conclusions.

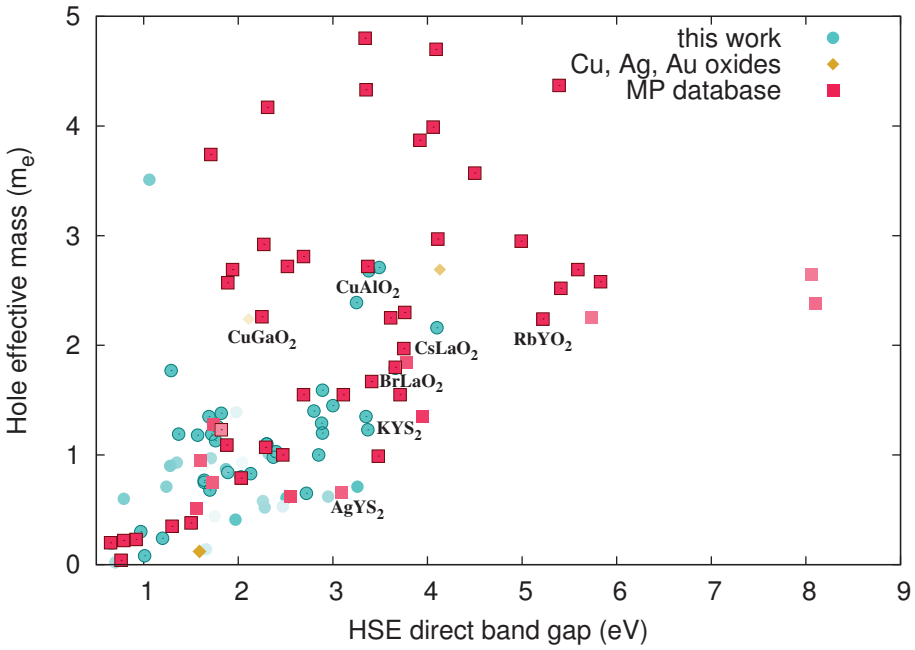

Figure 5.3 Hole effective masses as a function of the HSE06 band gap for all compounds that are thermodynamically stable.

5.4 Conclusions

We performed a high-throughput investigation using DFT and combining calculations of crystal prototypes with structural prediction. We focused on ternary compounds of composition ABX_2, where A and B are elements of the periodic table up to Bi, and X is a chalcogen (O, S, Se, and Te) in search of thermodynamically stable delafossite or closely related structures. The starting set of compositions was made of 15 624 compounds, for which we found the lowest-energy structure under the constraint to preserve the symmetries of the trigonal delafossite structure. After this step 285 compounds turn out to be within 50 meV/atom from the convex hull of stability. These compounds were further studied using the minima hopping method for global structural prediction, removing any symmetry constraint to obtain the ground-state crystal structure. At the end of this procedure, we could count 79 ternary systems not present in the materials project database that are thermodynamically stable (and therefore potentially synthesizable) and crystallize in the delafossite or in closely related structures. Among these new delafossites, 10 are oxides, 27 sulfides, 25 selenides and 17 tellurides. If we include also the new structures that are above the convex hull of stability within a threshold of 25 meV per atom, the number of new systems increases to 123.

By calculating the band gaps and hole effective masses of these structures we identified few systems that could be better *p*-type transparent conducting materials than those already

known. In particular, $AgYS_2$, with an HSE band gap of 3.16 eV and a hole effective mass of 0.71 m_e, is probably the best system that emerged from this study. KYS_2 and $RbYS_2$ have even larger band gaps (more than 4 eV) and effective masses of only about 1 m_e. We also found several systems, mainly containing Cr and Mn, that have relatively large magnetization densities.

These results provide us with a much more complete picture of the delafossite structure and can be used as a guide for further experimental and theoretical exploration of this fascinating family of compounds. The crystal structures of these new compounds are now available for more accurate theoretical characterization, hoping that some other interesting properties that have not been screened in this first study can come on the scene and motivate experimentalists to try to synthesize some of these compounds.

Chapter 6

Summary and conclusions

In this thesis, we used a combination of high-throughput and *ab initio* global structure prediction methods to study a wide range of different systems under different conditions. In the following, a summary of the most notable results is presented.

New phases of Ba-Si system under high pressure Using a global structural prediction method we studied systematically the phase diagram and the electronic properties of Ba–Si compounds. We identified five novel stoichiometric $BaSi_x$ phases with unexpected structures that might be experimentally synthesizable over a wide range of pressure. These include BaSi, $BaSi_2$, $BaSi_3$, $BaSi_5$, and $BaSi_6$. For the BaSi system, we found a new metallic *Imma* phase that is stable under pressure from 6 GPa to 65 GPa. For $BaSi_2$, there is a new metallic phase $Fd\bar{3}m$ that is stable from 21 GPa to 100 GPa. This phase, in which each Si forms six bonds with other neighboring Si atoms, becomes superconducting below 1.2 K at 50 GPa. Finally, at around 20 GPa two unexpected compositions become stable, namely $BaSi_3$ ($I4/mmm$) and $BaSi_5$ (*Cmmm*), both displaying metallic behavior. These results show the remarkable variety of Ba–Si compounds, and can serve as an important guide for further experimental studies of this binary system.

Phases diagram of N–H–O system under high pressure We explored the structures of ternary N–H–O system at 150 GPa using structural prediction (CALYPSO) combined with first-principle calculations. Two novel phases of NOH_4 and HNO_3 were predicted to exist at 150 GPa while NH_3H_2O will decompose into NH_3 and H_2O when the pressure is above 122 GPa. The novel phase of NOH_4 possesses $C2/m$ symmetry while the new phase of HNO_3 has a $P2_1/m$ symmetry. The $C2/m$ of NOH_4 becomes stable at 71 GPa, while the $P2_1/m$ phase of HNO_3 will be more energetically favorable than the phase II ($P2_1/c$) [186] from 39 GPa to 150 GPa, the maximum pressure that we have studied. For the $C2/m$ phase

of NOH_4, there is a layer formed by a NH_3-NH_3 "dumbbell cluster" which is between two layers formed by O-H chains. On the other hand, for the $P2_1/m$ phase of HNO_3, the layer is like a "quasi clover" with a H atom tail formed by three O atom, one N atom and one H atom. Surprisingly we find N-H-O covalent bonds in the $P2_1/m$ phase of HNO_3, revealing that pressure plays a major role for forming N-H-O covalent bonds in the N–H–O system. Electronic property calculations revealed that both the $C2/m$ phase of NOH_4 and the $P2_1/m$ phase of HNO_3 are insulators with a band gap of 6.0 eV and 2.6 eV, respectively.

Novel p-type transparent electrodes of ternary chalcogenides We performed a high-throughput investigation using density functional theory of possible thermodynamically stable phases of delafossite oxides, sulfides, selenides, and tellurides. The stable compositions were then studied using global structural prediction methods that allowed us to obtain their ground-state crystal structures. We found a total of 79 new delafossite (or related) phases that are stable, and therefore potentially possible to synthesize. By calculating the band gaps and hole effective masses of these structures we identified few systems that could be better *p*-type transparent conducting materials than those already known. In particular, $AgYS_2$, with an HSE band gap of 3.16 eV and a hole effective mass of 0.71 m_e, is probably the best system identified in this study. KYS_2 and $RbYS_2$ have even larger band gaps (more than 4 eV) and effective masses of about 1 m_e. We also found several systems, mainly containing Cr and Mn, that have relatively large magnetization densities. These results provide us with a much more complete picture of the interesting delafossite family and can be used as a guide for further experimental and theoretical exploration of this fascinating family of compounds.

In conclusion, the ab-initio prediction of new compounds is by now a mature subject. We showed that combining the power of DFT with high-throughput techniques and standard prediction methods is an efficient way to discover new materials with improved properties. This path is orders of magnitude faster than experimental synthesis and may allow us to have a rather complete view on more synthesizable compounds in a foreseeable future.

Acknowledgements

First, I tender my deepest thanks to my dedicated supervisors, Prof. Alfonso San Miguel, Prof. Miguel Marques and Prof. Silvana Botti for giving me the opportunity to work on this project, for your guidance and encouragement throughout my thesis work, for the discussions and corrections of my manuscript, and for your care of my living in Lyon and Jena as well. I also want to thank Dr. Stéphane Pailhès, Dr. Georges Boulon and Dr. Tristan Albaret, for the fruitful discussions. I would like to thank the rest of my thesis committee, for their encouragement, insightful comments, and hard questions.

I thank my fellow labmates in our group: Dr. Tiago Cerqueira, Dr. Sabine Korbel, Dr. Abraao Torres Dias, Pedro Borlido, Sun Lin, Dr. Claudia Rödl, Ivan Guilhon Mitoso Rocha, Valerio Armuzza, Christoph Otzen, Thomas Bischoff, Dr. Rafael A. Sarmiento Pérez , Silvio Domingos Silva Santos, Dr. Aude Stolz, Amani Tlili, and Helainne Thomeny Girao for the stimulating discussions and for all the fun we have had in the last three years.

To my friends, Zonglong Yang, Ye Tian, Xingjie Ma, Tianwen Huang, Kefeng Zhang, Zeya Jia, Ruihan Guo, Quanyi Yin, Biwen Zhu, Tingting Niu, Dan Yi, Mingchao Ji, Yang Wang, Yunpeng Luo, Jianbei Huang and other friends whose names are not listed here, thank you all for your company and help during my stay in Lyon and Jena.

I gratefully acknowledge Prof. Yanming Ma for your advice and help for applying the scholarship from China Scholarship Council (CSC). I also express my acknowledgement to CSC for funding this thesis.

I owe a great thanks to my girlfriend Wenwen Cui, thank you so much for your understanding and all your support on my work. Last but not the least, I would like to thank my family, for supporting me spiritually throughout my life.

List of Publications

■ J. Shi, W. Cui, J. Flores-Livas, S. Botti, and M. A. L. Marques. New phases in the Ba–Si phase diagram under high pressure by ab initio structural search, Phys. Chem. Chem. Phys. 2016, 18, 8108-8114.

■ J. Shi, T. F. T. Cerqueira, W. Cui, S. Botti, and M. A. L. Marques. High-throughput search of ternary chalcogenides for p-type transparent electrodes. Sci. Rep. 2017, 7, 43179.

■ J. Shi, W. Cui, S. Botti, and M. A. L. Marques. Ternary phase diagram of the N–H–O system: new phases at high pressure. 2017. (submitted to J. Phys. Chem. Lett.)

■ J. Schmidt, J. Shi, P. Borlido, L. Chen, S. Botti, and M. A. L. Marques. Predicting the thermodynamic stability of solids combining density functional theory and machine learning. 2017. Chem. Mater.

■ W. Cui, J. Shi, S. Botti, and M. A. L. Marques, Magnetism and contat properties of the ML MoS_2 interface. 2017. (ready to submit)

■ T. F. T. Cerqueira, S. Pailhès, R. Debord, V. M. Giordano, R. Viennois, J. Shi, S. Botti, and M. A. L. Marques. Prediction and synthesis of a non-zintl silicon clathrate. Chem. Mater. 2016, 3711-3717.

Bibliography

[1] Sarmiento-Pérez, R.; Cerqueira, T. F.; Valencia-Jaime, I.; Amsler, M.; Goedecker, S.; Romero, A. H.; Botti, S.; Marques, M. A. Novel phases of lithium-aluminum binaries from first-principles structural search. *J. Chem. Phys.* **2015**, *142*, 024710.

[2] Sarmiento-Pérez, R.; Cerqueira, T. F. T.; Valencia-Jaime, I.; Amsler, M.; Goedecker, S.; Botti, S.; Marques, M. A. L.; Romero, A. H. Sodium–gold binaries: novel structures for ionic compounds from an ab initio structural search. *New J. Phys.* **2013**, *15*, 115007.

[3] Bernstein, N.; Hellberg, C. S.; Johannes, M.; Mazin, I.; Mehl, M. What superconducts in sulfur hydrides under pressure and why. *Phys. Rev. B* **2015**, *91*, 060511.

[4] Flores-Livas, J. A.; Debord, R.; Botti, S.; San Miguel, A.; Marques, M. A.; Pailhès, S. Enhancing the Superconducting Transition Temperature of $BaSi_2$ by Structural Tuning. *Phys. Rev. Lett.* **2011**, *106*, 087002.

[5] Yu, L.; Zunger, A. Identification of potential photovoltaic absorbers based on first-principles spectroscopic screening of materials. *Phys. Rev. Lett.* **2012**, *108*, 068701.

[6] Lin, L.-C.; Berger, A. H.; Martin, R. L.; Kim, J.; Swisher, J. A.; Jariwala, K.; Rycroft, C. H.; Bhown, A. S.; Deem, M. W.; Haranczyk, M. In silico screening of carbon-capture materials. *Nature. Mater.* **2012**, *11*, 633–641.

[7] Krishna, R.; van Baten, J. M. In silico screening of metal–organic frameworks in separation applications. *Phys. Chem. Chem. Phys.* **2011**, *13*, 10593–10616.

[8] Yang, K.; Setyawan, W.; Wang, S.; Nardelli, M. B.; Curtarolo, S. A search model for topological insulators with high-throughput robustness descriptors. *Nature Mater.* **2012**, *11*, 614–619.

[9] Yang, J.; Li, H.; Wu, T.; Zhang, W.; Chen, L.; Yang, J. Evaluation of Half-Heusler Compounds as Thermoelectric Materials Based on the Calculated Electrical Transport Properties. *Adv. Func. Mater.* **2008**, *18*, 2880–2888.

[10] Bowler, D.; Miyazaki, T. Calculations for millions of atoms with density functional theory: linear scaling shows its potential. *J. Phys.: Condens. Matter* **2010**, *22*, 074207.

[11] Born, M.; Oppenheimer, R. Zur quantentheorie der molekeln. *Ann. Phys.* **1927**, *389*, 457–484.

[12] Dreizler, R. M.; Gross, E. K. *Density Functional Theory*; 1990.

[13] Hohenberg, P.; Kohn, W. Inhomogeneous electron gas. *Phys. Rev.* **1964**, *136*, B864.

[14] Kohn, W.; Sham, L. Density Function Theory. *Phys. Rev.* **1965**, *140*, A1133–A1138.

[15] Kohn, W.; Sham, L. J. Self-consistent equations including exchange and correlation effects. *Phys. Rev.* **1965**, *140*, A1133.

[16] Dirac, P. A. Note on exchange phenomena in the Thomas atom. Mathematical Proceedings of the Cambridge Philosophical Society. 1930; pp 376–385.

[17] Slater, J. C. A simplification of the Hartree-Fock method. *Phys. Rev.* **1951**, *81*, 385.

[18] Ceperley, D. M.; Alder, B. Ground state of the electron gas by a stochastic method. *Phys. Rev. Lett.* **1980**, *45*, 566.

[19] Vosko, S. H.; Wilk, L.; Nusair, M. Accurate spin-dependent electron liquid correlation energies for local spin density calculations: a critical analysis. *Can. J. Phys.* **1980**, *58*, 1200–1211.

[20] Perdew, J. P.; Wang, Y. Accurate and simple analytic representation of the electron-gas correlation energy. *Phys. Rev. B* **1992**, *45*, 13244.

[21] Becke, A. D. Density-functional exchange-energy approximation with correct asymptotic behavior. *Phys. Rev. A* **1988**, *38*, 3098.

[22] Lee, C.; Yang, W.; Parr, R. G. Development of the Colle-Salvetti correlation-energy formula into a functional of the electron density. *Phys. Rev. B* **1988**, *37*, 785.

[23] Colle, R.; Salvetti, O. Approximate calculation of the correlation energy for the closed shells. *Theor. Chim. Acta* **1975**, *37*, 329–334.

[24] Miehlich, B.; Savin, A.; Stoll, H.; Preuss, H. Results obtained with the correlation energy density functionals of Becke and Lee, Yang and Parr. *Chem. Phys. Lett.* **1989**, *157*, 200–206.

[25] Perdew, J. P.; Burke, K.; Ernzerhof, M. Generalized gradient approximation made simple. *Phys. Rev. Lett.* **1996**, *77*, 3865.

[26] Becke, A. Hartree–Fock exchange energy of an inhomogeneous electron gas. *Int. J. Quantum Chem.* **1983**, *23*, 1915–1922.

[27] Tao, J.; Perdew, J. P.; Staroverov, V. N.; Scuseria, G. E. Climbing the density functional ladder: Nonempirical meta–generalized gradient approximation designed for molecules and solids. *Phys. Rev. Lett.* **2003**, *91*, 146401.

[28] Becke, A. D. A new mixing of Hartree–Fock and local density-functional theories. *J. Chem. Phys.* **1993**, *98*, 1372–1377.

[29] Becke, A. D. Density-functional thermochemistry. III. The role of exact exchange. *J. Chem. Phys.* **1993**, *98*, 5648–5652.

[30] Seidl, A.; Görling, A.; Vogl, P.; Majewski, J. A.; Levy, M. Generalized Kohn-Sham schemes and the band-gap problem. *Phys. Rev. B* **1996**, *53*, 3764.

[31] Stephens, P.; Devlin, F.; Chabalowski, C.; Frisch, M. J. Ab initio calculation of vibrational absorption and circular dichroism spectra using density functional force fields. *J. Phys. Chem.* **1994**, *98*, 11623–11627.

[32] Becke, A. D. Density-functional thermochemistry. IV. A new dynamical correlation functional and implications for exact-exchange mixing. *J. Chem. Phys.* **1996**, *104*, 1040–1046.

[33] Perdew, J. P.; Ernzerhof, M.; Burke, K. Rationale for mixing exact exchange with density functional approximations. *J. Chem. Phys.* **1996**, *105*, 9982–9985.

[34] Adamo, C.; Barone, V. Toward reliable density functional methods without adjustable parameters: The PBE0 model. *J. Chem. Phys.* **1999**, *110*, 6158–6170.

[35] Ernzerhof, M.; Scuseria, G. E. Assessment of the Perdew–Burke–Ernzerhof exchange-correlation functional. *J. Chem. Phys.* **1999**, *110*, 5029–5036.

[36] Becke, A. D. Density-functional thermochemistry. V. Systematic optimization of exchange-correlation functionals. *J. Chem. Phys.* **1997**, *107*, 8554–8560.

[37] Zhao, Y.; Truhlar, D. G. The M06 suite of density functionals for main group thermochemistry, thermochemical kinetics, noncovalent interactions, excited states, and transition elements: two new functionals and systematic testing of four M06-class functionals and 12 other functionals. *Theor. Chem. Acc.* **2008**, *120*, 215–241.

[38] Grimme, S. Semiempirical hybrid density functional with perturbative second-order correlation. *J. Chem. Phys.* **2006**, *124*, 034108.

[39] Sharkas, K.; Toulouse, J.; Savin, A. Double-hybrid density-functional theory made rigorous. *J. Chem. Phys.* **2011**, *134*, 064113.

[40] Seminario, J. M. *Recent developments and applications of modern density functional theory*; Elsevier, 1996; Vol. 4.

[41] Iikura, H.; Tsuneda, T.; Yanai, T.; Hirao, K. A long-range correction scheme for generalized-gradient-approximation exchange functionals. *J. Chem. Phys.* **2001**, *115*, 3540–3544.

[42] Vydrov, O. A.; Scuseria, G. E. Assessment of a long-range corrected hybrid functional. *J. Chem. Phys.* **2006**, *125*, 234109.

[43] Gerber, I. C.; Angyán, J. G. Hybrid functional with separated range. *Chem. Phys. lett.* **2005**, *415*, 100–105.

[44] Yanai, T.; Tew, D. P.; Handy, N. C. A new hybrid exchange–correlation functional using the Coulomb-attenuating method (CAM-B3LYP). *Chem. Phys. lett.* **2004**, *393*, 51–57.

[45] Chai, J.-D.; Head-Gordon, M. Systematic optimization of long-range corrected hybrid density functionals. *J. Chem. Phys.* **2008**, *128*, 084106.

[46] Heyd, J.; Scuseria, G. E.; Ernzerhof, M. Hybrid functionals based on a screened Coulomb potential. *J. Chem. Phys.* **2003**, *118*, 8207–8215.

[47] Fujimura, K.; Seko, A.; Koyama, Y.; Kuwabara, A.; Kishida, I.; Shitara, K.; Fisher, C. A.; Moriwake, H.; Tanaka, I. Accelerated Materials Design of Lithium Superionic Conductors Based on First-Principles Calculations and Machine Learning Algorithms. *Adv. Energy Mater.* **2013**, *3*, 980–985.

[48] Ceder, G. Opportunities and challenges for first-principles materials design and applications to Li battery materials. *MRS Bull.* **2010**, *35*, 693–701.

[49] Curtarolo, S.; Hart, G. L. W.; Nardelli, M. B.; Mingo, N.; Sanvito, S.; Levy, O. The high-throughput highway to computational materials design. *Nat. Mater.* **2013**, *12*, 191–201.

[50] Carrete, J.; Li, W.; Mingo, N.; Wang, S.; Curtarolo, S. Finding unprecedentedly low-thermal-conductivity half-Heusler semiconductors via high-throughput materials modeling. *Phys. Rev. X* **2014**, *4*, 011019.

[51] Maddox, J. Waves caused by extreme dilution. *Nature* **1988**, *335*, 760–763.

[52] Day, G.; Motherwell, W.; Ammon, H.; Boerrigter, S.; Della Valle, R.; Venuti, E.; Dzyabchenko, A.; Dunitz, J.; Schweizer, B.; Van Eijck, B.; Others, A third blind test of crystal structure prediction. *Acta Crystallogr., Sect. B: Struct. Sci.* **2005**, *61*, 511–527.

[53] Kirkpatrick, S.; Gelatt, C. D.; Vecchi, M. P. Optimization by simmulated annealing. *Science* **1983**, *220*, 671–680.

[54] Woodley, S.; Battle, P.; Gale, J.; Catlow, C. A. The prediction of inorganic crystal structures using a genetic algorithm and energy minimisation. *Phys. Chem. Chem. Phys.* **1999**, *1*, 2535–2542.

[55] Abraham, N.; Probert, M. A periodic genetic algorithm with real-space representation for crystal structure and polymorph prediction. *Phys. Rev. B* **2006**, *73*, 224104.

[56] Oganov, A. R.; Glass, C. W. Crystal structure prediction using ab initio evolutionary techniques: Principles and applications. *J. Chem. Phys* **2006**, *124*, 244704.

[57] Glass, C. W.; Oganov, A. R.; Hansen, N. USPEX—evolutionary crystal structure prediction. *Comput. Phys. Commun.* **2006**, *175*, 713–720.

[58] Trimarchi, G.; Zunger, A. Global space-group optimization problem: Finding the stablest crystal structure without constraints. *Phys. Rev. B* **2007**, *75*, 104113.

[59] Wales, D. J.; Doye, J. P. Global optimization by basin-hopping and the lowest energy structures of Lennard-Jones clusters containing up to 110 atoms. *J. Phys. Chem. A* **1997**, *101*, 5111–5116.

[60] Nayeem, A.; Vila, J.; Scheraga, H. A. A comparative study of the simulated-annealing and Monte Carlo-with-minimization approaches to the minimum-energy structures of polypeptides:[Met]-enkephalin. *J.Comput. Chem.* **1991**, *12*, 594–605.

[61] Martoňák, R.; Laio, A.; Parrinello, M. Predicting crystal structures: The Parrinello-Rahman method revisited. *Phys. Rev. Lett.* **2003**, *90*, 075503.

[62] Martoňák, R.; Laio, A.; Bernasconi, M.; Ceriani, C.; Raiteri, P.; Zipoli, F.; Parrinello, M. Simulation of structural phase transitions by metadynamics. *Z. Kristallogr.* **2005**, *220*, 489–498.

[63] Pickard, C. J.; Needs, R. J. Structure of phase III of solid hydrogen. *Nat. Phys.* **2007**, *3*, 473–476.

[64] Pickard, C. J.; Needs, R. Highly compressed ammonia forms an ionic crystal. *Nat. Mater.* **2008**, *7*, 775–779.

[65] Pickard, C. J.; Needs, R. High-pressure phases of silane. *Phys. Rev. Lett.* **2006**, *97*, 045504.

[66] Mujica, A.; Needs, R. Theoretical study of the high-pressure phase stability of GaP, InP, and InAs. *Phys. Rev. B* **1997**, *55*, 9659.

[67] Wang, Y.; Lv, J.; Zhu, L.; Ma, Y. Crystal structure prediction via particle-swarm optimization. *Phys. Rev. B* **2010**, *82*, 094116.

[68] Wang, Y.; Lv, J.; Zhu, L.; Ma, Y. CALYPSO: A method for crystal structure prediction. *Comput. Phys. Commun.* **2012**, *183*, 2063–2070.

[69] Goedecker, S. Minima hopping: An efficient search method for the global minimum of the potential energy surface of complex molecular systems. *J. Chem. Phys.* **2004**, *120*, 9911–9917.

[70] Amsler, M.; Goedecker, S. Crystal structure prediction using the minima hopping method. *J. Chem. Phys.* **2010**, *133*, 224104.

[71] Kennedy, J. Eberhart. RC, 1995, Particle swarm optimization {C}. International Conference on Neural Networks, IV (Perth, Australia), Piscataway, NJ,(IEEE Service Center). 1942.

[72] Lu, H. Dynamic population strategy assisted particle swarm optimization in multi-objective evolutionary algorithm design. *IEEE Neural Network Society, IEEE NNS Student Research Grants* **2002**,

[73] Roy, S.; Goedecker, S.; Hellmann, V. Bell-Evans-Polanyi principle for molecular dynamics trajectories and its implications for global optimization. *Phys. Rev. E* **2008**, *77*, 056707.

[74] Amsler, M.; Flores-Livas, J. A.; Lehtovaara, L.; Balima, F.; Ghas emi, S. A.; Machon, D.; Pailhès, S.; Willand, A.; Caliste, D.; Botti, S.; San Miguel, A.; Goedecker, S.; Marques, M. A. L. Crystal Structure of Cold Compressed Graphite. *Phys. Rev. Lett.* **2012**, *108*, 065501.

[75] Huan, T. D.; Amsler, M.; Marques, M. A. L.; Botti, S.; Willand, A.; Goedecker, S. Low-Energy Polymeric Phases of Alanates. *Phys. Rev. Lett.* **2013**, *110*, 135502.

[76] Amsler, M.; Botti, S.; Marques, M. A. L.; Goedecker, S. Conducting Boron Sheets Formed by the Reconstruction of the α-Boron (111) Surface. *Phys. Rev. Lett.* **2013**, *111*, 136101.

[77] Cerqueira, T. F. T.; Sarmiento-Pérez, R.; Trani, F.; Amsler, M.; Goedecker, S.; Marques, M.; Botti, S. The crystal structure of p-type transparent conductive oxide $CuBO_2$. *MRS Commun.* **2013**, *3*, 157–160.

[78] Flores-Livas, J. A.; Amsler, M.; Lenosky, T. J.; Lehtovaara, L.; Botti, S.; Marques, M. A. L.; Goedecker, S. High-Pressure Structures of Disilane and Their Superconducting Properties. *Phys. Rev. Lett.* **2012**, *108*, 117004.

[79] Valencia-Jaime, I.; Sarmiento-Pérez, R.; Botti, S.; Marques, M. A.; Amsler, M.; Goedecker, S.; Romero, A. H. Novel crystal structures for lithium–silicon alloy predicted by minima hopping method. *J. Alloy. Compd.* **2016**, *655*, 147–154.

[80] Evers, J.; Weiss, A. Electrical properties of CrB type alkaline earth monosilicides and monogermanides. *Solid State Commun.* **1975**, *17*, 41–43.

[81] Schäfer, H.; Janzon, K.; Weiss, A. BaSi2, a phase with discrete Si4 tetrahedra. *Angew. Chem., Int. Ed. Engl.* **1963**, *2*, 393–394.

[82] Evers, J.; Oehlinger, G.; Weiss, A. Crystal Structure of Barium Disilicide at High Pressures. *Angew. Chem., Int. Ed. Engl.* **1977**, *16*, 659–660.

[83] Evers, J.; Oehlinger, G.; Weiss, A. A New High-Pressure Phase of Barium Disilicide. *Angew. Chem., Int. Ed. Engl.* **1978**, *17*, 538–539.

[84] Evers, J. Transformation of three-connected silicon in $BaSi_2$. *J. Solid State Chem.* **1980**, *32*, 77–86.

[85] Kumar, M.; Umezawa, N.; Imai, M. BaSi2 as a promising low-cost, earth-abundant material with large optical activity for thin-film solar cells: A hybrid density functional study. *Appl. Phys. Express* **2014**, *7*, 071203.

[86] Imai, M.; Hirano, T. Electrical resistivity of metastable phases of $BaSi_2$ synthesized under high pressure and high temperature. *J. Alloys Compd.* **1995**, *224*, 111–116.

[87] Pokhrel, A.; Samad, L.; Meng, F.; Jin, S. Synthesis and characterization of barium silicide ($BaSi_2$) nanowire arrays for potential solar applications. *Nanoscale* **2015**, *7*, 17450–17456.

[88] Morita, K.; Inomata, Y.; Suemasu, T. Optical and electrical properties of semiconducting BaSi 2 thin films on Si substrates grown by molecular beam epitaxy. *Thin Solid Films* **2006**, *508*, 363–366.

[89] Imai, M.; Hirata, K.; Hirano, T. Superconductivity of trigonal $BaSi_2$. *Phys. C* **1995**, *245*, 12–14.

[90] Flores-Livas, J. A.; Sanna, A. Superconductivity in intercalated group-IV honeycomb structures. *Phys. Rev. B* **2015**, *91*, 054508.

[91] Flores-Livas, J. A.; Debord, R.; Botti, S.; San Miguel, A.; Pailhès, S.; Marques, M. A. L. Superconductivity in layered binary silicides: A density functional theory study. *Phys. Rev. B* **2011**, *84*, 184503.

[92] Toulemonde, P.; San Miguel, A.; Merlen, A.; Viennois, R.; Le Floch, S.; Adessi, C.; Blase, X.; Tholence, J. High pressure synthesis and properties of intercalated silicon clathrates. *J. Phys. Chem. Solids* **2006**, *67*, 1117–1121.

[93] Yamanaka, S.; Enishi, E.; Fukuoka, H.; Yasukawa, M. High-pressure synthesis of a new silicon clathrate superconductor, Ba_8Si_46. *Inorg. Chem.* **2000**, *39*, 56–58.

[94] Rieger, W.; Parthé, E. Alkaline earth silicides, germanides and stannides with CrB structure type. *Acta Crystallogr.* **1967**, *22*, 919–922.

[95] Yamanaka, S.; Maekawa, S. Structural evolution of the binary system Ba-Si under high-pressure and high-temperature conditions. *Z. Naturforsch., B: J. Chem. Sci.* **2006**, *61*, 1493–1499.

[96] Dong, X.; Oganov, A. R.; Qian, G.; Zhou, X.-F.; Zhu, Q.; Wang, H.-T. How do chemical properties of the atoms change under pressure. *ArXiv preprint ArXiv:1503.00230* **2015**,

[97] Zhang, W.; Oganov, A. R.; Goncharov, A. F.; Zhu, Q.; Boulfelfel, S. E.; Lyakhov, A. O.; Stavrou, E.; Somayazulu, M.; Prakapenka, V. B.; Konôpková, Z. Unexpected Stable Stoichiometries of Sodium Chlorides. *Science* **2013**, *342*, 1502–1505.

[98] Zhu, L.; Liu, H.; Pickard, C. J.; Zou, G.; Ma, Y. Reactions of xenon with iron and nickel are predicted in the Earth's inner core. *Nat. Chem.* **2014**, *6*, 644–648.

[99] Cui, W.; Shi, J.; Liu, H.; Lu, C.; Wang, H. Novel high-pressure crystal structures of boron trifluoride. *J. Phys. Chem. Solids* **2014**, *75*, 1094–1098.

[100] Wang, H.; John, S. T.; Tanaka, K.; Iitaka, T.; Ma, Y. Superconductive sodalite-like clathrate calcium hydride at high pressures. *Proc. Natl. Acad. Sci.* **2012**, *109*, 6463–6466.

[101] Zhu, L.; Wang, Z.; Wang, Y.; Zou, G.; Mao, H.-k.; Ma, Y. Spiral chain O4 form of dense oxygen. *Proc. Natl. Acad. Sci.* **2012**, *109*, 751–753.

[102] Li, Y.; Wang, Y.; Pickard, C. J.; Needs, R. J.; Wang, Y.; Ma, Y. Metallic Icosahedron Phase of Sodium at Terapascal Pressures. *Phys. Rev. Lett.* **2015**, *114*, 125501.

[103] Liu, H.; Ma, Y. Proton or deuteron transfer in phase IV of solid hydrogen and deuterium. *Phys. Rev. Lett.* **2013**, *110*, 025903.

[104] Peng, F.; Miao, M.; Wang, H.; Li, Q.; Ma, Y. Predicted lithium–boron compounds under high pressure. *J. Am. Chem. Soc.* **2012**, *134*, 18599–18605.

[105] Lu, C.; Miao, M.; Ma, Y. Structural evolution of carbon dioxide under high pressure. *J. Am. Chem. Soc.* **2013**, *135*, 14167–14171.

[106] Lv, J.; Wang, Y.; Zhu, L.; Ma, Y. Predicted novel high-pressure phases of lithium. *Phys. Rev. Lett.* **2011**, *106*, 015503.

[107] Cui, W.; Shi, J.; Liu, H.; Yao, Y.; Wang, H.; Iitaka, T.; Ma, Y. Hydrogen segregation and its roles in structural stability and metallization: silane under pressure. *Sci. Rep.* **2015**, *5*, 13039.

[108] Gao, G.; Ashcroft, N. W.; Miao, M.; Hoffmann, R. Novel Si Networks in the Ca/Si Phase Diagram under Pressure. *J. Phys. Chem. C* **2014**, *118*, 25167–25175.

[109] Kresse, G.; Hafner, J. Ab initio molecular dynamics for liquid metals. *Phys. Rev. B* **1993**, *47*, 558.

[110] Kresse, G.; Joubert, D. From ultrasoft pseudopotentials to the projector augmented-wave method. *Phys. Rev. B* **1999**, *59*, 1758.

[111] Monkhorst, H. J.; Pack, J. D. Special points for Brillouin-zone integrations. *Phys. Rev. B* **1976**, *13*, 5188.

[112] Parlinski, K.; Li, Z.; Kawazoe, Y. First-principles determination of the soft mode in cubic ZrO_2. *Phys. Rev. Lett.* **1997**, *78*, 4063.

[113] Togo, A.; Oba, F.; Tanaka, I. First-principles calculations of the ferroelastic transition between rutile-type and $CaCl_2$-type SiO_2 at high pressures. *Phys. Rev. B* **2008**, *78*, 134106.

[114] ESPRESSO, Q. a modular and open-source software project for quantum simulations of materials/P. Giannozzi, S. Baroni, N. Bonini [et al.]. *J. Phys.: Condens. Matter* **2009**, *21*, 395502.

[115] Probst, C.; Wittig, J. Superconductivity of bcc barium under pressure. *Phys. Rev. Lett.* **1977**, *39*, 1161.

[116] Kenichi, T. High-pressure structural study of barium to 90 GPa. *Phys. Rev. B* **1994**, *50*, 16238.

[117] Hanfland, M.; Schwarz, U.; Syassen, K.; Takemura, K. Crystal structure of the high-pressure phase silicon VI. *Phys. rev. lett.* **1999**, *82*, 1197.

[118] Olijnyk, H.; Sikka, S.; Holzapfel, W. Structural phase transitions in Si and Ge under pressures up to 50 GPa. *Phys. Lett. A* **1984**, *103*, 137–140.

[119] Duclos, S. J.; Vohra, Y. K.; Ruoff, A. L. Experimental study of the crystal stability and equation of state of Si to 248 GPa. *Phys. Rev. B* **1990**, *41*, 12021.

[120] Imai, M.; Hirano, T.; Kikegawa, T.; Shimomura, O. In situ measurements of the orthorhombic-to-trigonal transition in $BaSi_2$ sunder high-pressure and high-temperature conditions. *Phys. Rev. B* **1997**, *55*, 132.

[121] Wang, J.-T.; Chen, C.; Kawazoe, Y. Phase stability and transition of $BaSi_2$-type disilicides and digermanides. *Phys. Rev. B* **2015**, *91*, 054107.

[122] Imai, M.; Hirano, T.; Kikegawa, T.; Shimomura, O. Phase transitions of $BaSi_2$ at high pressures and high temperatures. *Phys. Rev. B* **1998**, *58*, 11922.

[123] Pani, M.; Palenzona, A. The phase diagram of the Ba-Si system. *J. Alloys Compd.* **2008**, *454*, L1–L2.

[124] McMahon, J. M.; Morales, M. A.; Pierleoni, C.; Ceperley, D. M. The properties of hydrogen and helium under extreme conditions. *Rev. Mod. Phys.* **2012**, *84*, 1607.

[125] Flores-Livas, J. A. Computational and experimental studies of sp^3-materials at high pressure. PhD Thesis, École doctorale de Physique et d′Astrophysique (Lyon), 2012.

[126] Nishii, T.; Mizuno, T.; Mori, Y.; Takarabe, K.; Imai, M.; Kohara, S. X-ray diffraction study of amorphous phase of $BaSi_2$ under high pressure. *physica status solidi (b)* **2007**, *244*, 270–273.

[127] Sheng, X.-L.; Yan, Q.-B.; Ye, F.; Zheng, Q.-R.; Su, G. T-Carbon: A Novel Carbon Allotrope. *Phys. Rev. Lett.* **2011**, *106*, 155703.

[128] Wigner, E.; Huntington, H. á. On the possibility of a metallic modification of hydrogen. *J. Chem. Phys.* **1935**, *3*, 764–770.

[129] Gregoryanz, E.; Goncharov, A. F.; Hemley, R. J.; Mao, H.-k.; Somayazulu, M.; Shen, G. Raman, infrared, and x-ray evidence for new phases of nitrogen at high pressures and temperatures. *Phys. Rev. B* **2002**, *66*, 224108.

[130] Streib, W. E.; Jordan, T. H.; Lipscomb, W. N. Single-Crystal X-Ray Diffraction Study of β Nitrogen. *J. Chem. Phys.* **1962**, *37*, 2962–2965.

[131] Hanfland, M.; Lorenzen, M.; Wassilew-Reul, C.; Zontone, F. Structures of molecular nitrogen at high pressures. *Rev. High Press. Sci. Technol.* **1998**, *7*, 787–789.

[132] Hörl, E. Structure and structure imperfections of solid β-oxygen. *Acta Crystallogr.* **1962**, *15*, 845–850.

[133] Datchi, F.; Ninet, S.; Gauthier, M.; Saitta, A.; Canny, B.; Decremps, F. Solid ammonia at high pressure: A single-crystal x-ray diffraction study to 123 GPa. *Phys. Rev. B* **2006**, *73*, 174111.

[134] Gauthier, M.; Pruzan, P.; Chervin, J.; Besson, J. Raman scattering study of ammonia up to 75 GPa: Evidence for bond symmetrization at 60 GPa. *Phys. Rev. B* **1988**, *37*, 2102.

[135] Gauthier, M.; Pruzan, P.; Chervin, J.; Polian, A. Brillouin study of liquid and solid ammonia up to 20 GPa. *Solid State Commun.* **1988**, *68*, 149–153.

[136] Ma, Y.; Eremets, M.; Oganov, A. R.; Xie, Y.; Trojan, I.; Medvedev, S.; Lyakhov, A. O.; Valle, M.; Prakapenka, V. Transparent dense sodium. *Nature* **2009**, *458*, 182–185, DOI: 10.1038/nature07786.

[137] Li, Y.; Hao, J.; Liu, H.; Li, Y.; Ma, Y. The metallization and superconductivity of dense hydrogen sulfide. *J. Chem. Phys.* **2014**, *140*, 174712.

[138] Duan, D.; Liu, Y.; Tian, F.; Li, D.; Huang, X.; Zhao, Z.; Yu, H.; Liu, B.; Tian, W.; Cui, T. Pressure-induced metallization of dense (H2S) 2H2 with high-Tc superconductivity. *Sci. Rep.* **2014**, *4*, 6968.

[139] Drozdov, A.; Eremets, M.; Troyan, I.; Ksenofontov, V.; Shylin, S. Conventional superconductivity at 203 kelvin at high pressures in the sulfur hydride system. *Nature* **2015**, *525*, 73–76.

[140] Hazen, R.; Mao, H.; Finger, L.; Hemley, R. Single-crystal x-ray diffraction of n-H 2 at high pressure. *Phys. Rev. B* **1987**, *36*, 3944.

[141] Hemley, R.; Mao, H. Phase transition in solid molecular hydrogen at ultrahigh pressures. *Phys. Rev. Lett.* **1988**, *61*, 857.

[142] Mazin, I.; Hemley, R. J.; Goncharov, A.; Hanfland, M.; Mao, H.-k. Quantum and classical orientational ordering in solid hydrogen. *Phys. Rev. Lett.* **1997**, *78*, 1066.

[143] Goncharov, A. F.; Hemley, R. J.; Mao, H.-k. Vibron frequencies of solid H2 and D2 to 200 GPa and implications for the P–T phase diagram. *J. Chem. Phys.* **2011**, *134*, 174501.

[144] John, S. T.; Klug, D. D. Evidence from molecular dynamics simulations for nonmetallic behaviour of solid hydrogen above 160 GPa. *Nature* **1995**, *378*, 595.

[145] Kitamura, H.; Tsuneyuki, S.; Ogitsu, T.; Miyake, T. Quantum distribution of protons in solid molecular hydrogen at megabar pressures. *Nature* **2000**, *404*, 259–262.

[146] Tolédano, P.; Katzke, H.; Goncharov, A. F.; Hemley, R. J. Symmetry breaking in dense solid hydrogen: Mechanisms for the transitions to phase II and phase III. *Phys. Rev. Lett.* **2009**, *103*, 105301.

[147] Liu, H.; Zhu, L.; Cui, W.; Ma, Y. Room-temperature structures of solid hydrogen at high pressures. *J. Chem. Phys.* **2012**, *137*, 074501.

[148] McMinis, J.; Clay III, R. C.; Lee, D.; Morales, M. A. Molecular to atomic phase transition in hydrogen under high pressure. *Phys. Rev. Lett.* **2015**, *114*, 105305.

[149] Bini, R.; Ulivi, L.; Kreutz, J.; Jodl, H. J. High-pressure phases of solid nitrogen by Raman and infrared spectroscopy. *J. Chem. Phys.* **2000**, *112*, 8522–8529.

[150] Gregoryanz, E.; Goncharov, A. F.; Hemley, R. J.; Mao, H.-k. High-pressure amorphous nitrogen. *Phys. Rev. B* **2001**, *64*, 052103.

[151] Gregoryanz, E.; Goncharov, A. F.; Sanloup, C.; Somayazulu, M.; Mao, H.-k.; Hemley, R. J. High P-T transformations of nitrogen to 170 GPa. *J. Chem. Phys.* **2007**, *126*, 184505.

[152] Lipp, M. J.; Klepeis, J. P.; Baer, B.; Cynn, H.; Evans, W. J.; Iota, V.; Yoo, C.-S. Transformation of molecular nitrogen to nonmolecular phases at megabar pressures by direct laser heating. *Phys. Rev. B* **2007**, *76*, 014113.

[153] Eremets, M. I.; Hemley, R. J.; Mao, H.-k.; Gregoryanz, E. Semiconducting nonmolecular nitrogen up to 240 GPa and its low-pressure stability. *Nature* **2001**, *411*, 170–174.

[154] Ma, Y.; Oganov, A. R.; Li, Z.; Xie, Y.; Kotakoski, J. Novel high pressure structures of polymeric nitrogen. *Phys. Rev. Lett.* **2009**, *102*, 065501.

[155] Wang, X.; Wang, Y.; Miao, M.; Zhong, X.; Lv, J.; Cui, T.; Li, J.; Chen, L.; Pickard, C. J.; Ma, Y. Cagelike diamondoid nitrogen at high pressures. *Phys. Rev. Lett.* **2012**, *109*, 175502.

[156] Eremets, M. I.; Gavriliuk, A. G.; Trojan, I. A.; Dzivenko, D. A.; Boehler, R. Single-bonded cubic form of nitrogen. *Nat. Mater.* **2004**, *3*, 558–563.

[157] Tomasino, D.; Kim, M.; Smith, J.; Yoo, C.-S. Pressure-induced symmetry-lowering transition in dense nitrogen to layered polymeric nitrogen (LP-N) with colossal Raman intensity. *Phys. Rev. Lett.* **2014**, *113*, 205502.

[158] Eremets, M.; Gavriliuk, A.; Serebryanaya, N.; Trojan, I.; Dzivenko, D.; Boehler, R.; Mao, H.; Hemley, R. Structural transformation of molecular nitrogen to a single-bonded atomic state at high pressures. *J. Chem. Phys.* **2004**, *121*, 11296–11300.

[159] Gregoryanz, E.; Sanloup, C.; Bini, R.; Kreutz, J.; Jodl, H. J.; Somayazulu, M.; Mao, H.-k.; Hemley, R. J. On the -ζ transition of nitrogen. *J. Chem. Phys.* **2006**, *124*, 116102.

[160] Goncharov, A. F.; Gregoryanz, E.; Mao, H.-k.; Liu, Z.; Hemley, R. J. Optical evidence for a nonmolecular phase of nitrogen above 150 GPa. *Phys. Rev. Lett.* **2000**, *85*, 1262.

[161] Frost, M.; Howie, R. T.; Dalladay-Simpson, P.; Goncharov, A. F.; Gregoryanz, E. Novel high-pressure nitrogen phase formed by compression at low temperature. *Phys. Rev. B* **2016**, *93*, 024113.

[162] LeSar, R.; Etters, R. Character of the α-β phase transition in solid oxygen. *Phys. Rev. B* **1988**, *37*, 5364.

[163] Meier, R.; Helmholdt, R. Neutron-diffraction study of α-and β-oxygen. *Phys. Rev. B* **1984**, *29*, 1387.

[164] Schiferl, D.; Cromer, D.; Schwalbe, L.; Mills, R. Structure of'orange'18O2 at 9.6 GPa and 297 K. *Acta Crystallogr., Sect. B: Struct.* **1983**, *39*, 153–157.

[165] Gorelli, F. A.; Santoro, M.; Ulivi, L.; Hanfland, M. Crystal structure of solid oxygen at high pressure and low temperature. *Phys. Rev. B* **2002**, *65*, 172106.

[166] Goncharenko, I.; Makarova, O.; Ulivi, L. Direct determination of the magnetic structure of the delta phase of oxygen. *Phys. Rev. Lett.* **2004**, *93*, 055502.

[167] Fujihisa, H.; Akahama, Y.; Kawamura, H.; Ohishi, Y.; Shimomura, O.; Yamawaki, H.; Sakashita, M.; Gotoh, Y.; Takeya, S.; Honda, K. O 8 cluster structure of the epsilon phase of solid oxygen. *Phys. Rev. Lett.* **2006**, *97*, 085503.

[168] Lundegaard, L. F.; Weck, G.; McMahon, M. I.; Desgreniers, S.; Loubeyre, P. Observation of an O8 molecular lattice in the phase of solid oxygen. *Nature* **2006**, *443*, 201–204.

[169] Desgreniers, S.; Vohra, Y. K.; Ruoff, A. L. Optical response of very high density solid oxygen to 132 GPa. *Journal of Physical Chemistry* **1990**, *94*, 1117–1122.

[170] Akahama, Y.; Kawamura, H.; Häusermann, D.; Hanfland, M.; Shimomura, O. New high-pressure structural transition of oxygen at 96 GPa associated with metallization in a molecular solid. *Physical review letters* **1995**, *74*, 4690.

[171] Shimizu, K.; Suhara, K.; Ikumo, M.; Eremets, M.; Amaya, K. Superconductivity in oxygen. *Nature* **1998**, *393*, 767–769.

[172] Petrenko, V. F.; Whitworth, R. W. *Physics of ice*; OUP Oxford, 1999.

[173] Salzmann, C. G.; Radaelli, P. G.; Mayer, E.; Finney, J. L. Ice XV: a new thermodynamically stable phase of ice. *Phys. Rev. Lett.* **2009**, *103*, 105701.

[174] Benoit, M.; Bernasconi, M.; Focher, P.; Parrinello, M. New high-pressure phase of ice. *Phys. Rev. Lett.* **1996**, *76*, 2934.

[175] Militzer, B.; Wilson, H. F. New phases of water ice predicted at megabar pressures. *Phys. Rev. Lett.* **2010**, *105*, 195701.

[176] Wang, Y.; Liu, H.; Lv, J.; Zhu, L.; Wang, H.; Ma, Y. High pressure partially ionic phase of water ice. *Nat. Commun.* **2011**, *2*, 563.

[177] Pickard, C. J.; Martinez-Canales, M.; Needs, R. J. Decomposition and terapascal phases of water ice. *Phys. Rev. Lett.* **2013**, *110*, 245701.

[178] Li, D.; Oganov, A. R.; Dong, X.; Zhou, X.-F.; Zhu, Q.; Qian, G.; Dong, H. Nitrogen oxides under pressure: stability, ionization, polymerization, and superconductivity. *Sci. Rep.* **2015**, *5*.

[179] Hamilton, W. C.; Petrie, M. CONFIRMATION OF DISORDER IN SOLID NITROUS OXIDE BY NEUTRON DIFFRACTION1. *J. Phys. Chem.* **1961**, *65*, 1453–1454.

[180] Mills, R.; Olinger, B.; Cromer, D.; LeSar, R. Crystal structures of N2O to 12 GPa by x-ray diffraction. *J. Chem. Phys.* **1991**, *95*, 5392–5398.

[181] Zhu, C.; Bi, H.; Zhang, S.; Wei, S.; Li, Q. Exploring the metallic phase of N 2 O under high pressure. *RSC Adv.* **2015**, *5*, 65745–65749.

[182] An, Q.; Xiao, H.; Goddard III, W. A.; Meng, X. Stability of NNO and NPO Nanotube Crystals. *J. Phys. Chem. Lett.* **2014**, *5*, 485–489.

[183] Olovsson, I.; Templeton, D. H. The crystal structure of ammonia monohydrate. *Acta Crystallogr.* **1959**, *12*, 827–832.

[184] Fortes, A. D.; Suard, E.; Lemee-Cailleau, M.-H.; Pickard, C. J.; Needs, R. J. Crystal structure of ammonia monohydrate phase II. *J. Am. Chem. Soc.* **2009**, *131*, 13508–13515.

[185] Mafety, A. Étude ab initio des glaces d'ammoniac fluoré et hydraté sous conditions thermodynamiques extrêmes. PhD Thesis, École doctorale de Physique et Chinie des Matériaux - ED 397, 2016.

[186] Allan, D.; Marshall, W.; Francis, D.; Oswald, I.; Pulham, C.; Spanswick, C. The crystal structures of the low-temperature and high-pressure polymorphs of nitric acid. *Dalton Trans.* **2010**, *39*, 3736–3743.

[187] Shi, J.; Cui, W.; Flores-Livas, J. A.; San-Miguel, A.; Botti, S.; Marques, M. A. Investigation of new phases in the Ba–Si phase diagram under high pressure using ab initio structural search. *Phys. Chem. Chem. Phys.* **2016**, *18*, 8108–8114.

[188] Kawazoe, H.; Yasukawa, M.; Hyodo, H.; Kurita, M.; Yanagi, H.; Hosono, H. P-type electrical conduction in transparent thin films of $CuAlO_2$. *Nature* **1997**, *389*, 939–942, DOI: 10.1038/40087.

[189] Minami, T. Transparent conducting oxide semiconductors for transparent electrodes. *Semicond. Sci. Technol.* **2005**, *20*, S35, DOI: 10.1088/0268-1242/20/4/004.

[190] Jain, A.; Ong, S. P.; Hautier, G.; Chen, W.; Richards, W. D.; Dacek, S.; Cholia, S.; Gunter, D.; Skinner, D.; Ceder, G. The Materials Project: A materials genome approach to accelerating materials innovation. *APL Mater.* **2013**, *1*, 011002, DOI: 10.1063/1.4812323.

[191] Saal, J. E.; Kirklin, S.; Aykol, M.; Meredig, B.; Wolverton, C. Materials design and discovery with high-throughput density functional theory: the open quantum materials database (OQMD). *JOM* **2013**, *65*, 1501–1509, DOI: 10.1007/s11837-013-0755-4.

[192] Curtarolo, S.; Setyawan, W.; Wang, S.; Xue, J.; Yang, K.; Taylor, R. H.; Nelson, L. J.; Hart, G. L.; Sanvito, S.; Buongiorno-Nardelli, M. AFLOWLIB.ORG: A distributed materials properties repository from high-throughput ab initio calculations. *Comput. Mater. Sci.* **2012**, *58*, 227–235, DOI: 10.1016/j.commatsci.2012.02.002.

[193] Younsi, M.; Saadi, S.; Bouguelia, A.; Aider, A.; Trari, M. Synthesis and characterization of oxygen-rich delafossite $CuYO_{2+x}$–Application to H_2-photo production. *Sol. Energy Mater. Sol. Cells* **2007**, *91*, 1102 – 1109, DOI: 10.1016/j.solmat.2007.03.014.

[194] Saadi, S.; Bouguelia, A.; Derbal, A.; Trari, M. Hydrogen photoproduction over new catalyst $CuLaO_2$. *J. Photochem. Photobiol., A* **2007**, *187*, 97 – 104, DOI: 10.1016/j.jphotochem.2006.09.017.

[195] Liu, Y.; Gong, Y.; Mellott, N. P.; Wang, B.; Ye, H.; Wu, Y. Luminescence of delafossite-type $CuAlO_2$ fibers with Eu substitution for Al cations. *Sci. Technol. Adv. Mater.* **2016**, *17*, 200–209, DOI: 10.1080/14686996.2016.1172024.

[196] Daniel, U.; Radu, B.; Nicolae, V. Photovoltaic Performance of (Al, Mg)-Doped $CuCrO_2$ for p-type Dye-sensitized Solar Cells Application. *Nanosci. Nanotechnol.* **2016**, *6*, 71–76, DOI: 10.5923/c.nn.201601.14.

[197] Zakutayev, A. Design of nitride semiconductors for solar energy conversion. *J. Mater. Chem. A* **2016**, *4*, 6742–6754, DOI: 10.1039/C5TA09446A.

[198] Jiang, T.; Bujoli-Doeuff, M.; Farré, Y.; Blart, E.; Pellegrin, Y.; Gautron, E.; Boujtita, M.; Cario, L.; Odobel, F.; Jobic, S. Copper borate as a photocathode in p-type dye-sensitized solar cells. *RSC Adv.* **2016**, *6*, 1549–1553, DOI: 10.1039/C5RA24397A.

[199] Ono, Y.; i. Satoh, K.; Nozaki, T.; Kajitani, T. Structural, magnetic and thermoelectric properties of Delafossite-type oxide, $CuCr_{1-x}Mg_xO_2$ ($0 < x < 0.05$). 25th International Conference on Thermoelectrics, 2006. 2006; pp 92–96, DOI: 10.1109/ICT.2006.331288.

[200] Yasuhiro Ono, T. N., Ken-ichi Satoh; Kajitani, T. Structural, Magnetic and Thermoelectric Properties of Delafossite-type Oxide, $CuCr_{1-x}Mg_xO_2$ ($0 \leq x \leq 0.05$). *Jpn. J. Appl. Phys.* **2007**, *46*, 1071, DOI: 10.1143/JJAP.46.1071.

[201] Hayashi, K.; Nozaki, T.; Kajitani, T. Structure and High Temperature Thermoelectric Properties of Delafossite-Type Oxide $CuFe_{1-x}Ni_xO_2$ ($0 \leq x \leq 0.05$). *Jpn. J. Appl. Phys.* **2007**, *46*, 5226, DOI: 10.1143/JJAP.46.5226.

[202] Ohkubo, I.; Mori, T. Anisotropic Anomalies of Thermoelectric Transport Properties and Electronic Structures in Layered Complex Nitrides AMN_2 (A = Na, Cu; M = Ta, Nb). *Chem. Mater.* **2015**, *27*, 7265–7275, DOI: 10.1021/acs.chemmater.5b02015.

[203] Chutirat Taddee, T. K.; Amornkitbamrung, V. Characterization of transparent superconductivity Fe-doped $CuCrO_2$ delafossite oxide. *Appl. Surf. Sci.* **2016**, *380*, 237 – 242, DOI: 10.1016/j.apsusc.2016.01.120.

[204] Kushwaha, P.; Sunko, V.; Moll, P. J. W.; Bawden, L.; Riley, J. M.; Nandi, N.; Rosner, H.; Schmidt, M. P.; Arnold, F.; Hassinger, E.; Kim, T. K.; Hoesch, M.; Mackenzie, A. P.; King, P. D. C. Nearly free electrons in a 5d delafossite oxide metal. *Sci. Adv.* **2015**, *1*, e1500692, DOI: 10.1126/sciadv.1500692.

[205] Yanagi, H.; Kawazoe, H.; Kudo, A.; Yasukawa, M.; Hosono, H. Chemical Design and Thin Film Preparation of p-Type Conductive Transparent Oxides. *J. Electroceram.* **2000**, *4*, 407–414, DOI: 10.1023/A:1009959920435.

[206] Kawazoe, H.; Yanagi, H.; Ueda, K.; Hosono, H. Transparent p-Type Conducting Oxides: Design and Fabrication of p-n Heterojunctions. *MRS Bull.* **2000**, *25*, 28–36, DOI: 10.1557/mrs2000.148.

[207] Marquardt, M. A.; Ashmore, N. A.; Cann, D. P. Crystal chemistry and electrical properties of the delafossite structure. *Thin Solid Films* **2006**, *496*, 146 – 156, DOI: 10.1016/j.tsf.2005.08.316.

[208] Scanlon, D. O.; Godinho, K. G.; Morgan, B. J.; Watson, G. W. Understanding conductivity anomalies in CuI-based delafossite transparent conducting oxides: Theoretical insights. *J. Chem. Phys.* **2010**, *132*, 024707, DOI: 10.1063/1.3290815.

[209] Scanlon, D. O.; Walsh, A.; Watson, G. W. Understanding the p-Type Conduction Properties of the Transparent Conducting Oxide $CuBO_2$: A Density Functional Theory Analysis. *Chem. Mater.* **2009**, *21*, 4568–4576, DOI: 10.1021/cm9015113.

[210] Scanlon, D. O.; Watson, G. W. Understanding the p-type defect chemistry of $CuCrO_2$. *J. Mater. Chem.* **2011**, *21*, 3655–3663, DOI: 10.1039/C0JM03852K.

[211] Ginley, D. S., Hosono, H., Paine, D. C., Eds. *Handbook of transparent conductors*; Springer, 2010.

[212] Han, M.; Jiang, K.; Zhang, J.; Yu, W.; Li, Y.; Hu, Z.; Chu, J. Structural, electronic band transition and optoelectronic properties of delafossite $CuGa_{1-x}Cr_xO_2$ ($0 < x < 1$) solid solution films grown by the sol-gel method. *J. Mater. Chem.* **2012**, *22*, 18463–18470, DOI: 10.1039/C2JM33027J.

[213] Ueda, K.; Hase, T.; Yanagi, H.; Kawazoe, H.; Hosono, H.; Ohta, H.; Orita, M.; Hirano, M. Epitaxial growth of transparent p-type conducting $CuGaO_2$ thin films on sapphire (001) substrates by pulsed laser deposition. *J. Appl. Phys.* **2001**, *89*, 1790–1793, DOI: 10.1063/1.1337587.

[214] Yanagi, H.; Hase, T.; Ibuki, S.; Ueda, K.; Hosono, H. Bipolarity in electrical conduction of transparent oxide semiconductor $CuInO_2$ with delafossite structure. *Appl. Phys. Lett.* **2001**, *78*, 1583–1585, DOI: 10.1063/1.1355673.

[215] Nagarajan, R.; Draeseke, A.; Sleight, A.; Tate, J. P-type conductivity in $CuCr_{1-x}Mg_xO_2$ films and powders. *J. Appl. Phys.* **2001**, *89*, 8022–8025, DOI: 10.1063/1.1372636.

[216] Farrell, L.; Norton, E.; Smith, C. M.; Caffrey, D.; Shvets, I. V.; Fleischer, K. Synthesis of nanocrystalline Cu deficient $CuCrO_2$–a high figure of merit p-type transparent semiconductor. *J. Mater. Chem. C* **2016**, *4*, 126–134, DOI: 10.1039/C5TC03161C.

[217] Nagarajan, R.; Duan, N.; Jayaraj, M.; Li, J.; Vanaja, K.; Yokochi, A.; Draeseke, A.; Tate, J.; Sleight, A. P-type conductivity in the delafossite structure. *Int. J. Inorg. Mater.* **2001**, *3*, 265–270, DOI: 10.1063/1.1337587.

[218] Wang, Y.; Gu, Y.; Wang, T.; Shi, W. Structural, optical and electrical properties of Mg-doped $CuCrO_2$ thin films by sol-gel processing. *J. Alloys Compd.* **2011**, *509*, 5897–5902, DOI: 10.1016/j.jallcom.2011.02.175.

[219] Barnabé, A.; Thimont, Y.; Lalanne, M.; Presmanes, L.; Tailhades, P. p-Type conducting transparent characteristics of delafossite Mg-doped $CuCrO_2$ thin films prepared by RF-sputtering. *J. Mater. Chem. C* **2015**, *3*, 6012–6024, DOI: 10.1039/C5TC01070E.

[220] Hosono, H. Recent progress in transparent oxide semiconductors: Materials and device application. *Thin Solid Films* **2007**, *515*, 6000 – 6014, DOI: 10.1016/j.tsf.2006.12.125.

[221] Ueda, K.; Inoue, S.; Hirose, S.; Kawazoe, H.; Hosono, H. Transparent p-type semiconductor: LaCuOS layered oxysulfide. *Appl. Phys. Lett.* **2000**, *77*, 2701–2703, DOI: 10.1063/1.1319507.

[222] Hiramatsu, H.; Ueda, K.; Ohta, H.; Hirano, M.; Kamiya, T.; Hosono, H. Degenerate p-type conductivity in wide-gap $LaCuOS_{1-x}Se_x$ ($x = 0 - 1$) epitaxial films. *Appl. Phys. Lett.* **2003**, *82*, 1048–1050, DOI: 10.1063/1.1544643.

[223] Krishnapriyan, A.; Barton, P. T.; Miao, M.; Seshadri, R. First-principles study of band alignments in the p-type hosts BaM_2X_2 (M = Cu, Ag; X = S, Se). *J. Phys.: Condens. Matter* **2014**, *26*, 155802, DOI: 10.1088/0953-8984/26/15/155802.

[224] Hautier, G.; Miglio, A.; Ceder, G.; Rignanese, G.-M.; Gonze, X. Identification and design principles of low hole effective mass p-type transparent conducting oxides. *Nat. Commun.* **2013**, *4*, 2292, DOI: 10.1038/ncomms3292.

[225] Sarmadian, N.; Saniz, R.; Partoens, B.; Lamoen, D. Easily doped p-type, low hole effective mass, transparent oxides. *Sci. Rep.* **2016**, *6*, 20446, DOI: 10.1038/srep20446.

[226] Cerqueira, T. F.; Lin, S.; Amsler, M.; Goedecker, S.; Botti, S.; Marques, M. A. Identification of novel Cu, Ag, and Au ternary oxides from global structural prediction. *Chem. Mater.* **2015**, *27*, 4562–4573, DOI: 10.1021/acs.chemmater.5b00716.

[227] Morgan, D.; Ceder, G.; Curtarolo, S. High-throughput and data mining with ab initio methods. *Meas. Sci. Technol.* **2005**, *16*, 296, DOI: 10.1088/0957-0233/16/1/039.

[228] Oganov, A. R., Ed. *Modern Methods of Crystal Structure Prediction*; Wiley-VCH: Berlin, 2010.

[229] Kresse, G.; Furthmüller, J. Efficiency of ab-initio total energy calculations for metals and semiconductors using a plane-wave basis set. *Comput. Mater. Sci.* **1996**, *6*, 15–50, DOI: 10.1016/0927-0256(96)00008-0.

[230] Kresse, G.; Furthmüller, J. Efficient iterative schemes for ab initio total-energy calculations using a plane-wave basis set. *Phys. Rev. B* **1996**, *54*, 11169–11186, DOI: 10.1103/PhysRevB.54.11169.

[231] Blöchl, P. E. Projector augmented-wave method. *Phys. Rev. B* **1994**, *50*, 17953, DOI: 10.1103/PhysRevB.50.17953.

[232] Tran, F.; Stelzl, J.; Blaha, P. Rungs 1 to 4 of DFT Jacob's ladder: Extensive test on the lattice constant, bulk modulus, and cohesive energy of solids. *The Journal of Chemical Physics* **2016**, *144*, DOI: 10.1063/1.4948636.

[233] Sarmiento-Pérez, R.; Botti, S.; Marques, M. A. L. Optimized Exchange and Correlation Semilocal Functional for the Calculation of Energies of Formation. *J. Chem. Theory Comput.* **2015**, *11*, 3844–3850, DOI: 10.1021/acs.jctc.5b00529.

[234] Ong, S. P.; Richards, W. D.; Jain, A.; Hautier, G.; Kocher, M.; Cholia, S.; Gunter, D.; Chevrier, V. L.; Persson, K. A.; Ceder, G. Python Materials Genomics (pymatgen): A robust, open-source python library for materials analysis. *Comput. Mater. Sci.* **2013**, *68*, 314–319, DOI: 10.1016/j.commatsci.2012.10.028.

[235] Bergerhoff, G.; Brown, I. Inorganic Crystal Structure Database. In *Crystallographic Databases*; International Union of Crystallography: Chester, 1987.

[236] Belsky, A.; Hellenbrandt, M.; Karen, V. L.; Luksch, P. New developments in the Inorganic Crystal Structure Database (ICSD): accessibility in support of materials research and design. *Acta Crystallogr., Sect. B: Struct. Sci., Cryst. Eng. Mater.* **2002**, *58*, 364–369, DOI: 10.1107/S0108768102006948.

[237] Madsen, G. K.; Singh, D. J. BoltzTraP. A code for calculating band-structure dependent quantities. *Comput. Phys. Commun.* **2006**, *175*, 67–71, DOI: 10.1016/j.cpc.2006.03.007.

[238] Schleife, A.; Fuchs, F.; Rödl, C.; Furthmüller, J.; Bechstedt, F. Branch-point energies and band discontinuities of III-nitrides and III-II-oxides from quasiparticle band-structure calculation. *Appl. Phys. Lett.* **2009**, *94*, 012104, DOI: 10.1063/1.3059569.

[239] Robertson, J.; Clark, S. J. Limits to doping in oxides. *Phys. Rev. B* **2011**, *83*, 075205, DOI: 10.1103/PhysRevB.83.075205.

[240] Momma, K.; Izumi, F. VESTA 3 for three-dimensional visualization of crystal, volumetric and morphology data. *J. Appl. Crystallogr.* **2011**, *44*, 1272–1276.

[241] Glawe, H.; Sanna, A.; Gross, E. K. U.; Marques, M. A. L. The optimal one dimensional periodic table: a modified Pettifor chemical scale from data mining. *New J. Phys.* **2016**, *18*, 093011, DOI: 10.1088/1367-2630/18/9/093011.

[242] Pettifor, D. A chemical scale for crystal-structure maps. *Solid State Commun.* **1984**, *51*, 31–34, DOI: 10.1016/0038-1098(84)90765-8.

[243] Takatsu, H.; Nénert, G.; Kadowaki, H.; Yoshizawa, H.; Enderle, M.; Yonezawa, S.; Maeno, Y.; Kim, J.; Tsuji, N.; Takata, M. Magnetic structure of the conductive triangular-lattice antiferromagnet $PdCrO_2$. *Phys. Rev. B* **2014**, *89*, 104408, DOI: 10.1103/PhysRevB.89.104408.

[244] Shannon, R. D.; Rogers, D. B.; Prewitt, C. T. Chemistry of noble metal oxides. I. Syntheses and properties of ABO_2 delafossite compounds. *Inorg. Chem.* **1971**, *10*, 713–718, DOI: 10.1021/ic50098a011.

[245] Boon, J. The crystal structure of $NaBiS_2$ and $KBiS_2$. *Recl. Trav. Chim. Pays-Bas* **1944**, *63*, 32–34, DOI: 10.1002/recl.19440630203.

[246] Havlak, L.; Fabry, J.; Henriques, M.; Dušek, M. Structure determination of $KScS_2$, $RbScS_2$ and $KLnS_2$ (Ln= Nd, Sm, Tb, Dy, Ho, Er, Tm and Yb) and crystal chemical discussion. *Acta Crystallogr., Sect. C: Struct. Chem.* **2015**, *71*, 623–630, DOI: 10.1016/0025-5408(87)90038-9.

[247] Pachoud, E.; Damay, F.; Martin, C.; Mordvinova, N. E.; Lebedev, O. I.; Maignan, A. Robustness of Antiferromagnetism and Pyroelectricity in $AgCr_{1-x}Rh_xS_2$. *Chem. Mater.* **2016**, *28*, 1816–1822, DOI: 10.1021/acs.chemmater.5b04948.

[248] Ballestracci, R. Une classe de nouveaux composés sulfurés de terres rares et d'argent de type $AgTS_2$. *C. R. Seances Acad. Sci., Ser. C* **1966**, *262*, 1253–1256.

[249] Sidorov, M.; McKelvy, M.; Sharma, R.; Glaunsinger, W.; Ganal, P.; Moreau, P.; Ouvrard, G. Structural Investigation of Mercury-Intercalated Titanium Disulfide. 2. HRTEM of Hg_xTiS_2. *Chem. Mater.* **1995**, *7*, 1140–1152, DOI: 10.1021/cm00054a014.

[250] Veliev, R.; Sadykhov, R.; Asadov, Y. G.; Kerimova, E.; Dzhabbarov, A. Magnetization, paramagnetic susceptibility, and electrical conductivity of layered $TlMnS_2$ and $TlMnSe_2$ antiferromagnets. *Crystallogr. Rep.* **2008**, *53*, 130–133, DOI: 10.1134/S1063774508010161.

[251] Dijkstra, J.; Van Bruggen, C.; Haas, C.; de Groot, R. Electronic structure of the half-metallic ferromagnet $KCrSe_2$. *Phys. Rev. B* **1989**, *40*, 7973, DOI: 10.1103/PhysRevB.40.7973.

[252] Trippel, A.; Lazarev, V.; Berul, S. Synthesis and properties of some compounds $ABiTe_2$. *Zh. Neorg. Khim.* **1978**, *23*, 707–710.

[253] S. Kabré, M. G., M. Julien Pouzol Sur une nouvelle famille de tellurures doubles de thallium(I) et de terres rares. *C. R. Seances Acad. Sci., Ser. C* **1972**, *275*, 1367–1370.

[254] Vidal, J.; Trani, F.; Bruneval, F.; Marques, M. A. L.; Botti, S. Effects of Electronic and Lattice Polarization on the Band Structure of Delafossite Transparent Conductive Oxides. *Phys. Rev. Lett.* **2010**, *104*, 136401, DOI: 10.1103/PhysRevLett.104.136401.

[255] Trani, F.; Vidal, J.; Botti, S.; Marques, M. A. L. Band structures of delafossite transparent conductive oxides from a self-consistent *GW* approach. *Phys. Rev. B* **2010**, *82*, 085115, DOI: 10.1103/PhysRevB.82.085115.

[256] Pellicer-Porres, J.; Segura, A.; Gilliland, A.; Munoz, A.; Rodríguez-Hernández, P.; Kim, D.; Lee, M.; Kim, T. On the band gap of $CuAlO_2$ delafossite. *Appl. Phys. Lett.* **2006**, *88*, 181904–181904, DOI: 10.1063/1.2200398.

Appendix A

Structual parameters of the novel phases with composition ABX_2. (Chapter 5)

We summarize structual parameters of the new stable delafossite and closedly related phases with composition ABO_2, ABS_2, $ABSe_2$ and $ABTe_2$.

Table A.1 Structual parameters of the new stable delafossite and closely related phases with composition ABO_2.

Compounds	Spg nunmber (name)	Lattice parameters	Atom	Coordinates parameters
		a=3.35949 Å	In	0.00000 0.00000 0.50000
$KInO_2$	166^b(R -3 2/m)	b=3.35949 Å	K	0.00000 0.00000 0.00000
		c=18.54410 Å	O	0.00000 0.00000 -0.22894
		α=β=90°,γ=120°		
		a=3.39981 Å	In	0.00000 0.00000 0.00000
$RbInO_2$	166^b(R -3 2/m)	b=3.39981 Å	Rb	0.00000 0.00000 0.50000
		c=19.36914 Å	O	0.00000 0.00000 -0.27463
		α=β=90°,γ=120°		
		a=3.29582 Å	Rh	0.00000 0.00000 0.00000
$RbRhO_2$	166^b(R -3 2/m)	b=3.29582 Å	Rb	0.00000 0.00000 0.50000
		c=17.953 Å	O	0.00000 0.00000 -0.28092
		α=β=90°,γ=120°		
		a=3.78465 Å	La	0.00000 0.00000 0.00000
$CsLaO_2$	166^b(R -3 2/m)	b=3.78465 Å	Cs	0.00000 0.00000 0.50000
		c=20.84 Å	O	0.00000 0.00000 -0.27684
		α=β=90°,γ=120°		
		a=3.00143 Å	Ni	0.00000 0.00000 0.50000
$MgNiO_2$	166^b(R -3 2/m)	b=3.00143 Å	Mg	0.00000 0.00000 0.00000
		c=14.558 Å	O	0.00000 0.00000 0.25082
		α=β=90°,γ=120°		
		a=2.86607 Å	Pd	0.00000 0.00000 0.50000
$PdAlO_2$	166^a(R -3 2/m)	b=2.86607 Å	Al	0.00000 0.00000 0.00000
		c=18.09580 Å	O	0.00000 0.00000 -0.38662
		α=β=90°,γ=120°		
		a=3.00903 Å	Pd	0.00000 0.00000 0.50000
$PdCrO_2$	166^a(R -3 2/m)	b=3.00903 Å	Cr	0.00000 0.00000 0.00000
		c=18.23102 Å	O	0.00000 0.00000 -0.38882
		α=β=90°,γ=120°		
		a=3.08303 Å	Pd	0.00000 0.00000 0.00000
$PdRhO_2$	166^a(R -3 2/m)	b=3.08303 Å	Rh	0.00000 0.00000 0.50000
		c=18.30676 Å	O	0.00000 0.00000 0.11048
		α=β=90°,γ=120°		

Table A.2 Structual parameters of the new stable delafossite and closely related phases with composition ABO_2. Continuation of Table A.1.

$PtAlO_2$	166[a](R -3 2/m)	a=2.85681 Å b=2.85681 Å c=18.15331 Å $\alpha=\beta=90°,\gamma=120°$	Pt Al O	0.00000 0.00000 0.00000 0.00000 0.00000 0.50000 0.00000 0.00000 0.11357
$PtNiO_2$	166[a](R -3 2/m)	a=2.92246 Å b=2.92246 Å c=18.21565 Å $\alpha=\beta=90°,\gamma=120°$	Pt Ni O	0.00000 0.00000 0.50000 0.00000 0.00000 0.00000 0.00000 0.00000 -0.39247
$HgMgO_2$	166[a](R -3 2/m)	a=3.25902 Å b=3.25902 Å c=18.25154 Å $\alpha=\beta=90°,\gamma=120°$	Hg Mg O	0.00000 0.00000 0.00000 0.00000 0.00000 0.50000 0.00000 0.00000 0.11034
$TlRhO_2$	166[a](R -3 2/m)	a=3.16242 Å b=3.16242 Å c=20.77487 Å $\alpha=\beta=90°,\gamma=120°$	Tl Rh O	0.00000 0.00000 0.00000 0.00000 0.00000 0.50000 0.00000 0.00000 -0.12102
$BrCdO_2$	166[a](R -3 2/m)	a=3.51303 Å b=3.51303 Å c=18.64577 Å $\alpha=\beta=90°,\gamma=120°$	Cd Br O	0.00000 0.00000 0.00000 0.00000 0.00000 0.50000 0.00000 0.00000 0.39411
$BrLaO_2$	12 (A 1 2/m 1)	a=8.25488 Å b=3.94162 Å c=6.85559 Å $\alpha=\gamma=90°,\beta=134.99°$	La Br O	0.00000 0.00000 0.00000 0.50000 0.50000 0.50000 -0.16000 0.00000 1.00000
$BrNiO_2$	166[a](R -3 2/m)	a=3.11474 Å b=3.11474 Å c=17.78526 Å $\alpha=\beta=90°,\gamma=120°$	Br Ni O	0.00000 0.00000 0.00000 0.00000 0.00000 0.50000 0.00000 0.00000 -0.11013
$BrTlO_2$	166[a](R -3 2/m)	a=3.63606 Å b=3.63606 Å c=18.94165 Å $\alpha=\beta=90°,\gamma=120°$	Tl Br O	0.00000 0.00000 0.50000 0.00000 0.00000 0.00000 0.00000 0.00000 -0.11016

Table A.3 Structual parameters of the new stable delafossite and closely related phases with composition ABS_2.

Compounds	Spg nunmber (name)	Lattice parameters	Atom	Coordinates parameters
		a=3.65516 Å	Ir	0.00000 0.00000 0.19100
$HIrS_2$	160 (R 3 m)	b=3.65516 Å	S	0.00000 0.00000 -0.21000
		c=17.47866 Å	S	0.00000 0.00000 -0.41600
		α=β=90°,γ=120°	H	0.00000 0.00000 -0.33500
		a=4.15325 Å	Bi	0.00000 0.00000 0.00000
$KBiS_2$	166[b](R -3 2/m)	b=4.15325 Å	K	0.00000 0.00000 0.50000
		c=22.36348 Å	S	0.00000 0.00000 -0.26288
		α=β=90°,γ=120°		
		a=3.84107 Å	Sc	0.00000 0.00000 0.00000
$KScS_2$	166[b](R -3 2/m)	b=3.84107 Å	K	0.00000 0.00000 0.50000
		c=21.87898 Å	S	0.00000 0.00000 -0.26922
		α=β=90°,γ=120°		
		a=4.05568 Å	Y	0.00000 0.00000 0.00000
KYS_2	166[b](R -3 2/m)	b=4.05568 Å	K	0.00000 0.00000 0.50000
		c=22.12079 Å	S	0.00000 0.00000 -0.26596
		α=β=90°,γ=120°		
		a=3.87064 Å	Rb	0.00000 0.00000 0.00000
$RbScS_2$	166[b](R -3 2/m)	b=3.87064 Å	Sc	0.00000 0.00000 0.50000
		c=22.80286 Å	S	0.00000 0.00000 0.22769
		α=β=90°,γ=120°		
		a=3.35973 Å	Ag	0.00000 0.00000 0.00000
$AgCoS_2$	166[a](R -3 2/m)	b=3.35973 Å	Co	0.00000 0.00000 0.50000
		c=21.26877 Å	S	0.00000 0.00000 -0.11332
		α=β=°,γ=120°		
		a=3.32591 Å	Ag	0.00000 0.00000 0.00000
$AgMnS_2$	166[a](R -3 2/m)	b=3.32591 Å	Mn	0.00000 0.00000 0.50000
		c=22.33769 Å	S	0.00000 0.00000 -0.10862
		α=β=90°,γ=120°		
		a=3.57217 Å	Ag	0.00000 0.00000 0.00000
$AgRhS_2$	166[a](R -3 2/m)	b=3.57217 Å	Rh	0.00000 0.00000 0.50000
		c=21.49311 Å	S	0.00000 0.00000 -0.11138
		α=β=90°,γ=120°		
		a=b=3.76128 Å	Ag	0.00000 0.00000 0.00658
$AgScS_2$	160 (R 3 m)	c=20.68221 Å	Sc	0.00000 0.00000 0.15680
		α=β=90°	S	0.00000 0.00000 0.41700
		γ=120°	S	0.0000 0.00000 -0.11144
		a=3.60138 Å	Ir	0.00000 0.00000 0.50000
$AgIrS_2$	166[a](R -3 2/m)	b=3.60138 Å	Ag	0.00000 0.00000 0.00000
		c=21.37937 Å	S	0.00000 0.00000 -0.11235
		α=β=90°,γ=120°		

Table A.4 Structual parameters of the new stable delafossite and closely related phases with composition ABS_2. Continuation of Table A.3.

$AgYS_2$	156 (P 3 m 1)	a=b=4.05641 Å c=6.63987 Å α=β=90° γ=120°	Ag Y S S	0.33300 0.66700 -0.42100 0.00000 0.00000 -0.00178 0.33300 0.66700 0.20456 0.66700 0.33300 -0.23684
$AuAlS_2$	166[a](R -3 2/m)	a=3.56258 Å b=3.56258 Å c=21.56252 Å α=β=90°,γ=120°	Au S Al	0.00000 0.00000 0.00000 0.00000 0.00000 -0.10762 0.00000 0.00000 0.50000
$AuBiS_2$	166[a](R -3 2/m)	a=4.28266 Å b=4.28266 Å c=22.26884 Å α=β=90°,γ=120°	Bi Au S	0.00000 0.00000 0.50000 0.00000 0.00000 0.0000 0.00000 0.00000 -0.10296
$AuCoS_2$	166[a](R -3 2/m)	a=3.36726 Å b=3.36726 Å c=20.78827 Å α=β=90°,γ=120°	Au Co S	0.00000 0.00000 0.00000 0.00000 0.00000 0.50000 0.00000 0.00000 -0.11258
$AuInS_2$	166[a](R -3 2/m)	a=3.94181 Å b=3.94181 Å c=22.00386 Å α=β=90°,γ=120°	Au In S	0.00000 0.00000 0.00000 0.00000 0.00000 0.50000 0.00000 0.00000 -0.10468
$AuIrS_2$	166[a](R -3 2/m)	a=3.61618 Å b=3.61618 Å c=20.86395 Å α=β=90°,γ=120°	Au Ir S	0.00000 0.00000 0.00000 0.00000 0.00000 0.50000 0.00000 0.00000 -0.11166
$AuMnS_2$	166[a](R -3 2/m)	a=3.33532 Å b=3.33532 Å c=21.81510 Å α=β=90°,γ=120°	Au Mn S	0.00000 0.00000 0.00000 0.00000 0.00000 0.50000 0.00000 0.00000 -0.10786
$AuRhS_2$	166[a](R -3 2/m)	a=3.58538 Å b=3.58538 Å c=20.98328 Å α=β=90°,γ=120°	Au Rh S	0.00000 0.00000 0.00000 0.00000 0.00000 0.50000 0.00000 0.00000 -0.11063
$AuScS_2$	166[a](R -3 2/m)	a=3.82016 Å b=3.82016 Å c=22.01038 Å α=β=90°,γ=120°	Au Sc S	0.00000 0.00000 0.00000 0.00000 0.00000 0.50000 0.00000 0.00000 -0.10493
$AuYS_2$	166[a](R -3 2/m)	a=4.13622 Å b=4.13622 Å c=22.10901 Å α=β=90°,γ=120°	Au Y S	0.00000 0.00000 0.00000 0.00000 0.00000 0.50000 0.00000 0.00000 -0.10430
$HgHfS_2$	166[b](R -3 2/m)	a=3.63137 Å b=3.63137 Å c=28.69144 Å α=β=90°,γ=120°	Hg Hf S	0.00000 0.00000 0.00000 0.00000 0.00000 0.50000 0.00000 0.00000 0.21733

Table A.5 Structual parameters of the new stable delafossite and closely related phases with composition ABS_2. Continuation of Table A.4.

$HgMnS_2$	166[a](R -3 2/m)	a=3.34606 Å b=3.34606 Å c=27.51030 Å α=β=90°,γ=120°	Hg Mn S	0.00000 0.00000 0.00000 0.00000 0.00000 0.50000 0.00000 0.00000 -0.11876
$HgPtS_2$	166[b](R -3 2/m)	a=3.57244 Å b=3.57244 Å c=26.37048 Å α=β=90°,γ=120°	Hg Pt S	0.00000 0.00000 0.50000 0.00000 0.00000 0.00000 0.00000 0.00000 -0.28647
$HgTiS_2$	1 (P 1)	a=5.90492 Å b=3.39530 Å c=9.60591 Å α=87.44096° β=105.41234° γ=89.99510°	Hg Hg Ti Ti S S S S	-0.44390 -0.49609 1.00000 0.48651 -0.42345 -0.49379 -0.01571 -0.22243 0.00483 0.48495 0.28364 0.00500 -0.11507 0.26144 0.16022 0.08440 0.30054 -0.14989 0.38464 -0.23908 0.15946 -0.41558 -0.19991 -0.15015
$HgZrS_2$	166[b](R -3 2/m)	a=3.67081 Å b=3.67081 Å c=28.05292 Å α=β=90°,γ=120°	Hg Zr S	0.00000 0.00000 0.50000 0.00000 0.00000 0.00000 0.00000 0.00000 -0.28090
$BiAlS_2$	166[a](R -3 2/m)	a=3.53328 Å b=3.53328 Å c=24.70228 Å α=β=90°,γ=120°	Bi S Al	0.00000 0.00000 0.00000 0.00000 0.00000 -0.11385 0.00000 0.00000 0.50000
$BiCrS_2$	166[a](R -3 2/m)	a=3.52727 Å b=3.52727 Å c=24.57201 Å α=β=90°,γ=120°	Bi Cr S	0.00000 0.00000 0.00000 0.00000 0.00000 0.50000 0.00000 0.00000 -0.11492
$BiTiS_2$	166[a](R -3 2/m)	a=3.44094 Å b=3.44094 Å c=25.83420 Å α=β=90°,γ=120°	Bi Ti S	0.00000 0.00000 0.50000 0.00000 0.00000 0.00000 0.00000 0.00000 -0.38896
$BiIrS_2$	166[a](R -3 2/m)	a=3.59387 Å b=3.59387 Å c=24.25913 Å α=β=90°,γ=120°	Bi Ir S	0.00000 0.00000 0.00000 0.00000 0.00000 0.50000 0.00000 0.00000 -0.11851
$InTiS_2$	166[a](R -3 2/m)	a=3.39205 Å b=3.39205 Å c=26.02497 Å α=β=90°,γ=120°	In Ti S	0.00000 0.00000 0.00000 0.00000 0.00000 0.50000 0.00000 0.00000 -0.11113
$InZrS_2$	164 (P -3 2/m 1)	a=b=3.61485 Å c=8.18948 Å α=β=90°,γ=120°	In Zr S	0.00000 0.00000 0.50000 0.00000 0.00000 0.00000 0.33333 0.66667 0.18891

Table A.6 Structual parameters of the new stable delafossite and closely related phases with composition ABS_2. Continuation of Table A.5.

		a=b=3.59750 Å	Tl	0.00000 0.00000 0.00000
$TlHfS_2$	164 (P -3 2/m 1)	c=8.54200 Å	Hf	0.00000 0.00000 0.50000
		α=β=90°,γ=120°	S	0.33333 0.66667 -0.32445
		a=3.37108 Å	Tl	0.00000 0.00000 0.00000
$TlMnS_2$	166[a](R -3 2/m)	b=3.37108 Å	Mn	0.00000 0.00000 0.50000
		c=26.36703 Å	S	0.00000 0.00000 -0.11764
		α=β=90°,γ=120°		
		a=b=3.47225 Å	Tl	0.00000 0.00000 0.00000
$TlTiS_2$	164 (P -3 2/m 1)	c=8.17414 Å	Ti	0.00000 0.00000 0.50000
		α=β=90°,γ=120°	S	0.33333 0.66667 -0.32576
		a=b=3.64723 Å	Tl	0.00000 0.00000 0.00000
$TlZrS_2$	164 (P -3 2/m 1)	c=8.25608 Å	Zr	0.00000 0.00000 0.50000
		α=β=90°,γ=120°	S	0.33333 0.66667 0.31475
		a=3.46684 Å	Sn	0.00000 0.00000 0.00000
$SnCrS_2$	166[a](R -3 2/m)	b=3.46684 Å	Cr	0.00000 0.00000 0.50000
		c=24.44877 Å	S	0.00000 0.00000 -0.11396
		α=β=90°,γ=120°		
		a=3.39805 Å	Sn	0.00000 0.00000 0.00000
$SnTiS_2$	166[a](R -3 2/m)	b=3.39805 Å	Ti	0.00000 0.00000 0.50000
		c=25.67830 Å	S	0.00000 0.00000 -0.11020
		α=β=90°,γ=120°		
		a=3.46683 Å	Pb	0.00000 0.00000 0.00000
$PbCrS_2$	166[a](R -3 2/m)	b=3.46683 Å	Cr	0.00000 0.00000 0.50000
		c=25.11917 Å	S	0.00000 0.00000 -0.11541
		α=β=90°,γ=120°		
		a=3.43824 Å	Pb	0.00000 0.00000 0.00000
$PbTiS_2$	166[a](R -3 2/m)	b=3.43824 Å	Ti	0.00000 0.00000 0.50000
		c=26.24558 Å	S	0.00000 0.00000 -0.11203
		α=β=90°,γ=120°		
		a=3.60049 Å	Pb	0.00000 0.00000 0.00000
$PbZrS_2$	166[a](R -3 2/m)	b=3.60049 Å	Zr	0.00000 0.00000 0.50000
		c=26.99142 Å	S	0.00000 0.00000 -0.10959
		α=β=90°,γ=120°		

Table A.7 Structual parameters of the new stable delafossite and closely related phases with composition $ABSe_2$.

Compounds	Spg nunmber (name)	Lattice parameters	Atom	Coordinates parameters
		a=3.81064 Å	Se	0.00000 0.00000 -0.09441
$HMnSe_2$	166[a](R -3 2/m)	b=3.81064 Å	Mn	0.00000 0.00000 0.50000
		c=18.66232 Å	H	0.00000 0.00000 0.00000
		α=β=90°,γ=120°		
		a=7.00059 Å	Se	-0.34909 0.25000 -0.26884
$HScSe_2$	11 (P 1 21/m 1)	b=3.97127 Å	Se	-0.14044 0.25000 0.30354
		c=7.02455 Å	Sc	0.27769 0.25000 0.49027
		α=γ=90°,β=108°	H	-0.22547 0.25000 0.07693
		a=3.86391 Å	Se	0.00000 0.00000 0.27399
$KCrSe_2$	166[b](R -3 2/m)	b=3.86391 Å	Cr	0.00000 0.00000 0.00000
		c=22.19740 Å	K	0.00000 0.00000 0.50000
		α=β=90°,γ=120°		
		a=4.01205 Å	Se	0.00000 0.00000 0.26816
$KScSe_2$	166[b](R -3 2/m)	b=4.01205 Å	Sc	0.00000 0.00000 0.00000
		c=22.83015 Å	K	0.00000 0.00000 0.50000
		α=β=90°,γ=120°		
		a=3.90273 Å	Rh	0.00000 0.00000 0.00000
$KRhSe_2$	166[b](R -3 2/m)	b=3.90273 Å	Se	0.00000 0.00000 0.27722
		c=21.30640 Å	K	0.00000 0.00000 0.50000
		α=β=90°,γ=120°		
		a=4.21753 Å	Y	0.00000 0.00000 0.50000
$KYSe_2$	166[b](R -3 2/m)	b=4.21753 Å	Se	0.00000 0.00000 0.23517
		c=23.04535 Å	K	0.00000 0.00000 0.00000
		α=β=90°,γ=120°		
		a=4.04394 Å	Rb	0.00000 0.00000 0.50000
$RbScSe_2$	166[b](R -3 2/m)	b=4.04394 Å	Se	0.00000 0.00000 0.27115
		c=23.74805 Å	Sc	0.00000 0.00000 0.00000
		α=β=90°,γ=120°		
		a=3.93388 Å	Rh	0.00000 0.00000 0.00000
$RbRhSe_2$	166[b](R -3 2/m)	b=3.93388 Å	Rb	0.00000 0.00000 0.50000
		c=22.07918 Å	Se	0.00000 0.00000 0.28001
		α=β=90°,γ=120°		
		a=4.07381 Å	Cs	0.00000 0.00000 0.50000
$CsScSe_2$	166[b](R -3 2/m)	b=4.07381 Å	Se	0.00000 0.00000 0.27437
		c=24.81908 Å	Sc	0.00000 0.00000 0.00000
		α=β=90°,γ=120°		
		a=4.50022 Å	La	0.00000 0.00000 0.00000
$CsLaSe_2$	166[b](R -3 2/m)	b=4.50022 Å	Cs	0.00000 0.00000 0.50000
		c=25.13292 Å	Se	0.00000 0.00000 0.26978
		α=β=90°,γ=120°		
		a=3.97311 Å	Cs	0.00000 0.00000 0.00000
$CsRhSe_2$	166[b](R -3 2/m)	b=3.97311 Å	Rh	0.00000 0.00000 0.50000
		c=22.88826 Å	Se	0.00000 0.00000 0.21710
		α=β=90°,γ=120°		

Table A.8 Structual parameters of the new stable delafossite and closely related phases with composition $ABSe_2$. Continuation of Table A.7.

$CsYSe_2$	166[b](R -3 2/m)	a=4.27003 Å b=4.27003 Å c=25.11956 Å α=β=90°,γ=120°	Cs Y Se	0.00000 0.00000 0.00000 0.00000 0.00000 0.50000 0.00000 0.00000 -0.22865
$AgMnSe_2$	166[b](R -3 2/m)	a=3.76196 Å b=3.76196 Å c=19.82880 Å α=β=90°,γ=120°	Ag Se Mn	0.00000 0.00000 0.50000 0.00000 0.00000 -0.26018 0.00000 0.00000 0.00000
$AgRhSe_2$	166[a](R -3 2/m)	a=3.75170 Å b=3.75170 Å c=22.62660 Å α=β=90°,γ=120°	Ag Rh Se	0.00000 0.00000 0.00000 0.00000 0.00000 0.50000 0.00000 0.00000 -0.11125
$AuCoSe_2$	166[a](R -3 2/m)	a=3.56141 Å b=3.56141 Å c=21.99416 Å α=β=90°,γ=120°	Au Se Co	0.00000 0.00000 0.00000 0.00000 0.00000 -0.11227 0.00000 0.00000 0.50000
$AuCrSe_2$	166[a](R -3 2/m)	a=3.74847 Å b=3.74847 Å c=22.57021 Å α=β=90°,γ=120°	Au Se Cr	0.00000 0.00000 0.00000 0.00000 0.00000 -0.10836 0.00000 0.00000 0.50000
$AuMnSe_2$	166[a](R -3 2/m)	a=3.79353 Å b=3.79353 Å c=22.78084 Å α=β=90°,γ=120°	Au Se Mn	0.00000 0.00000 0.00000 0.00000 0.00000 -0.10703 0.00000 0.00000 0.50000
$AuRhSe_2$	166[a](R -3 2/m)	a=3.76914 Å b=3.76914 Å c=22.11265 Å α=β=90°,γ=120°	Au Rh Se	0.00000 0.00000 0.00000 0.00000 0.00000 0.50000 0.00000 0.00000 -0.11075
$HgHfSe_2$	166[b](R -3 2/m)	a=3.75047 Å b=3.75047 Å c=29.09357 Å α=β=90°,γ=120°	Hg Hf Se	0.00000 0.00000 0.00000 0.00000 0.00000 0.50000 0.00000 0.00000 -0.22118
$HgMnSe_2$	166[b](R -3 2/m)	a=3.48295 Å b=3.48295 Å c=28.09625 Å α=β=90°,γ=120°	Hg Se Mn	0.00000 0.00000 0.50000 0.00000 0.00000 0.28205 0.00000 0.00000 0.00000
$HgNbSe_2$	38(A m m 2)	a=9.60790 Å b=3.47683 Å c=6.01235 Å α=β=90°,γ=90°	Hg Nb Se	0.50000 0.00000 0.01408 0.00000 0.00000 0.33580 -0.17541 0.00000 -0.33075
$HgPtSe_2$	166[b](R -3 2/m)	a=3.74663 Å b=3.74663 Å c=26.63660 Å α=β=90°,γ=120°	Hg Pt Se	0.00000 0.00000 0.50000 0.00000 0.00000 0.00000 0.00000 0.00000 0.28394

Table A.9 Structual parameters of the new stable delafossite and closely related phases with composition $ABSe_2$. Continuation of Table A.8.

$HgRhSe_2$	166[a](R -3 2/m)	a=3.80643 Å b=3.80643 Å c=23.93630 Å α=β=90°,γ=120°	Hg Rh Se	0.00000 0.00000 0.00000 0.00000 0.00000 0.50000 0.00000 0.00000 -0.11563
$HgTiSe_2$	1 (P 1)	a=3.52743 Å b=10.10198 Å c=6.11632 Å α=102.59452° β=90° γ=99.61212°	Hg Hg Se Se Se Se Ti Ti	0.48447 0.00794 -0.02072 0.47672 -0.00430 0.47278 -0.23259 -0.33594 0.16527 0.11387 0.34262 0.21573 0.26668 -0.33700 -0.33558 -0.38583 0.34373 -0.28350 0.19058 -0.49659 -0.05892 -0.30968 -0.49673 0.44005
$HgVSe_2$	6 (P 1 m 1)	a=3.33180 Å b=9.78877 Å c=3.32996 Å α=γ=90°, β=90°	Hg Se V	-0.16355 0.00000 0.25366 0.44473 0.33673 -0.11923 0.11095 0.50000 -0.45296
$HgZrSe_2$	166[b](R -3 2/m)	a=3.78211 Å b=3.78211 Å c=28.37739 Å α=β=90°,γ=120°	Hg Zr Se	0.00000 0.00000 0.00000 0.00000 0.00000 0.50000 0.00000 0.00000 -0.22324
$InZrSe_2$	164 (P -3 2/m 1)	a=b=3.74384 Å c=8.43595 Å α=β=90°,γ=120°	In Zr Se	0.00000 0.00000 0.00000 0.00000 0.00000 0.50000 0.33333 0.66667 -0.30261
$TlHfSe_2$	164[b](P -3 2/m 1)	a=3.72705 Å b=3.72705 Å c=8.77741 Å α=β=90°,γ=120°	Tl Hf Se	0.00000 0.00000 0.50000 0.00000 0.00000 0.00000 0.33333 0.66667 0.18439
$TlMnSe_2$	166[b](R -3 2/m)	a=3.83420 Å b=3.83420 Å c=22.61324 Å α=β=90°,γ=120°	Tl Se Mn	0.00000 0.00000 0.50000 0.00000 0.00000 -0.27216 0.00000 0.00000 0.00000
$TlRhSe_2$	164 (P -3 2/m 1)	a=3.62640 Å b=3.62640 Å c=8.41867 Å α=β=90°,γ=120°	Tl Se Rh	0.00000 0.00000 0.00000 0.33333 0.66667 0.31829 0.00000 0.00000 0.50000
$TlTiSe_2$	164 (P -3 2/m 1)	a=b=3.62640 Å c=8.41867 Å α=β=90°,γ=120°	Tl Se Ti	0.00000 0.00000 0.00000 0.33333 0.66667 0.31829 0.00000 0.00000 0.50000
$TlVSe2_2$	187 (P -6 m 2)	a=b=3.42683 Å c=8.66380 Å α=β=90°,γ=120°	Tl Se V	0.33333 0.66667 0.00000 0.00000 0.00000 -0.32134 0.33333 0.66667 0.50000
$TlZrSe_2$	164 (P -3 2/m 1)	a=b=3.78264 Å c=8.47906 Å α=β=90°,γ=120°	Tl Zr Se	0.00000 0.00000 0.50000 0.00000 0.00000 0.00000 0.33333 0.66667 -0.19389

Table A.10 Structual parameters of the new stable delafossite and closely related phases with composition $ABSe_2$. Continuation of Table A.9.

$SbMnSe_2$	11 (P 1 21/m 1)	a=8.59123 Å b=3.92579 Å c=6.32267 Å α=γ=90° β=75.92688°	Sb Se Se Mn	-0.02917 0.25000 -0.15519 0.32357 0.25000 0.47176 -0.34643 0.25000 0.03697 -0.49235 0.25000 -0.27482
$BiCrSe_2$	166[a](R -3 2/m)	a=3.65977 Å b=3.65977 Å c=25.89903 Å α=β=90°,γ=120°	Bi Se Cr	0.00000 0.00000 0.00000 0.00000 0.00000 -0.11356 0.00000 0.00000 0.50000
$BiMnSe_2$	166[a](R -3 2/m)	a=3.63018 Å b=3.63018 Å c=26.29310 Å α=β=90°,γ=120°	Bi Se Mn	0.00000 0.00000 0.50000 0.00000 0.00000 -0.38732 0.00000 0.00000 0.00000
$BrNiSe_2$	166[a](R -3 2/m)	a=3.70682 Å b=3.70682 Å c=22.84750 Å α=β=90°,γ=120°	Br Se Ni	0.00000 0.00000 0.00000 0.00000 0.00000 -0.11562 0.00000 0.00000 0.50000
$INiSe_2$	166[a](R -3 2/m)	a=3.75533 Å b=3.75533 Å c=23.93427 Å α=β=90°,γ=120°	I Se Ni	0.00000 0.00000 0.00000 0.00000 0.00000 -0.11809 0.00000 0.00000 0.50000

Table A.11 Structual parameters of the new stable delafossite and closely related phases with composition $ABTe_2$.

Compounds	Spg nunmber (name)	Lattice parameters	Atom	Coordinates parameters
		a=b=4.30381 Å	Te	0.33333 0.66667 -0.25725
$LiYTe_2$	164 (P -3 2/m 1)	c=7.15747 Å	Y	0.00000 0.00000 0.00000
		α=β=90°,γ=120°	Li	0.00000 0.00000 0.50000
		a=4.43028 Å	Te	0.00000 0.00000 0.24412
$NaYTe_2$	166[b](R -3 2/m)	b=4.43028 Å	Y	0.00000 0.00000 0.50000
		c=22.70594 Å	Na	0.00000 0.00000 0.00000
		α=β=90°,γ=120°		
		a=4.74251 Å	La	0.00000 0.00000 0.50000
$RbLaTe_2$	166[b](R -3 2/m)	b=4.74251 Å	Te	0.00000 0.00000 -0.23545
		c=25.61822 Å	Rb	0.00000 0.00000 0.00000
		α=β=90°,γ=120°		
		a=4.65619 Å	Bi	0.00000 0.00000 0.00000
$CsBiTe_2$	166[b](R -3 2/m)	b=4.65619 Å	Cs	0.00000 0.00000 0.50000
		c=26.88465 Å	Te	0.00000 0.00000 0.26897
		α=β=90°,γ=120°		
		a=4.20620 Å	Hf	0.00000 0.00000 0.00000
$CsHfTe_2$	166[b](R -3 2/m)	b=4.20620 Å	Cs	0.00000 0.00000 0.50000
		c=27.05162 Å	Te	0.00000 0.00000 0.27177
		α=β=90°,γ=120°		
		a=4.37131 Å	Cs	0.00000 0.00000 0.00000
$CsScTe_2$	166[b](R -3 2/m)	b=4.37131 Å	Te	0.00000 0.00000 0.22681
		c=26.50526 Å	Sc	0.00000 0.00000 0.50000
		α=β=90°,γ=120°		
		a=4.55740 Å	Cs	0.00000 0.00000 0.50000
$CsYTe_2$	166[b](R -3 2/m)	b=4.55740 Å	Te	0.00000 0.00000 0.26999
		c=26.74329 Å	Y	0.00000 0.00000 0.00000
		α=β=90°,γ=120°		
		a=4.76440 Å	Ba	0.00000 0.00000 0.00000
$BaCaTe_2$	166[b](R -3 2/m)	b=4.76440 Å	Te	0.00000 0.00000 -0.24129
		c=23.39713 Å	Ca	0.00000 0.00000 0.50000
		α=β=90°,γ=120°		
		a=4.03881 Å	Te	0.00000 0.00000 0.24288
$AgMnTe_2$	166[b](R -3 2/m)	b=4.03881 Å	Ag	0.00000 0.00000 0.00000
		c=20.81605 Å	Mn	0.00000 0.00000 0.50000
		α=β=90°,γ=120°		
		a=3.95145 Å	Hg	0.00000 0.00000 0.00000
$HgHfTe_2$	166[b](R -3 2/m)	b=3.95145 Å	Hf	0.00000 0.00000 0.50000
		c=29.71098 Å	Te	0.00000 0.00000 0.22664
		α=β=90°,γ=120°		
		a=3.73742 Å	Hg	0.00000 0.00000 0.50000
$HgTiTe_2$	166[b](R -3 2/m)	b=3.73742 Å	Te	0.00000 0.00000 0.27456
		c=29.77145 Å	Ti	0.00000 0.00000 0.00000
		α=β=90°,γ=120°		

Table A.12 Structual parameters of the new stable delafossite and closely related phases with composition $ABTe_2$. Continuation of Table A.11.

$HgVTe_2$	11 (P 1 21/m 1)	a=6.51190 Å b=3.56739 Å c=10.08520 Å α=γ=90° β=103.2329°	Hg Te Te V	-0.27846 0.25000 -0.01198 -0.47984 0.25000 0.34788 -0.01042 0.25000 -0.30972 0.20860 0.25000 0.49595
$HgZrTe_2$	166[b](R -3 2/m)	a=3.96118 Å b=3.96118 Å c=28.83456 Å α=β=90°,γ=120°	Hg Te Zr	0.00000 0.00000 0.50000 0.00000 0.00000 0.27047 0.00000 0.00000 0.00000
$InYTe_2$	166[n](R -3 2/m)	a=4.41664 Å b=4.41664 Å c=24.30902 Å α=β=90°,γ=120°	Te In Y	0.00000 0.00000 0.26013 0.00000 0.00000 0.50000 0.00000 0.00000 0.00000
$TlHfTe_2$	164 (P -3 2/m 1)	a=b=3.98106 Å c=8.97218 Å α=β=90°,γ=120°	Tl Hf Te	0.00000 0.00000 0.00000 0.00000 0.00000 0.50000 0.33333 0.66667 0.30201
$TlMnTe_2$	164 (P -3 2/m 1)	a=b=4.09771 Å c=8.03708 Å α=β=90°,γ=120°	Tl Te Mn	0.00000 0.00000 0.00000 0.33333 0.66667 0.31205 0.00000 0.00000 0.50000
$TlTiTe_2$	164 (P -3 2/m 1)	a=b=3.87987 Å c=8.81594 Å α=β=90°,γ=120°	Tl Te Ti	0.00000 0.00000 0.50000 0.33333 0.66667 -0.19086 0.00000 0.00000 0.00000
$TlYTe_2$	166[b](R -3 2/m)	a=4.45463 Å b=4.45463 Å c=24.55466 Å α=β=90°,γ=120°	Tl Te Y	0.00000 0.00000 0.50000 0.00000 0.00000 0.26210 0.00000 0.00000 0.00000
$TlZrTe_2$	164 (P -3 2/m 1)	a=b=4.01882 Å c= 8.87565 Å α=β=90°,γ=120°	Tl Te Zr	0.00000 0.00000 0.00000 0.33333 0.66667 -0.29706 0.00000 0.00000 0.50000
$BrCoTe_2$	166[a](R -3 2/m)	a=3.92958 Å b=3.92958 Å c=24.25180 Å α=β=90°,γ=120°	Te Br Co	0.00000 0.00000 -0.11673 0.00000 0.00000 0.00000 0.00000 0.00000 0.50000
$BrIrTe_2$	160 (R 3 m) (hexagonal axes)	a=b=4.11707 Å c=25.57033 Å α=β=90°,γ=120°	Ir Te Te Br	0.00000 0.00000 -0.33956 0.00000 0.00000 0.27253 0.00000 0.00000 0.03659 0.00000 0.00000 0.13794
$BrNiTe_2$	166[b](R -3 2/m)	a=3.89925 Å b=3.89925 Å c=22.24186 Å α=β=90°,γ=120°	Te Br Ni	0.00000 0.00000 -0.27675 0.00000 0.00000 0.50000 0.00000 0.00000 0.00000

Table A.13 Structual parameters of the new stable delafossite and closely related phases with composition $ABTe_2$. Continuation of Table A.12.

$BrPdTe_2$	12 (A 1 2/m 1)	a=9.3950 Å,b=4.1186 Å c=15.46901 Å α=γ=90° β=158.55°	Te Pd Br	0.21339 0.00000 0.01870 0.00000 0.50000 0.00000 0.50000 0.00000 0.50000
$BrPtTe_2$	166[b](R -3 2/m)	a=4.09656 Å b=4.09656 Å c=22.19780 Å α=β=90°,γ=120°	Pt Te Br	0.00000 0.00000 0.50000 0.00000 0.00000 0.22624 0.00000 0.00000 0.00000
$BrRhTe_2$	166[a](R -3 2/m)	a=4.13050 Å b=4.13050 Å c=24.26323 Å α=β=90°,γ=120°	Te Rh Br	0.00000 0.00000 -0.11598 0.00000 0.00000 0.50000 0.00000 0.00000 0.00000
$INiTe_2$	13 (P 1 2/n 1)	a=8.9478 Å,b=3.9454 Å c=8.14783 Å α=γ=90° β=133.06°	I Te Ni	0.75000 -0.24968 0.75000 0.02430 0.25030 -0.31515 0.75000 0.24964 0.25000
$IPdTe_2$	12 (A 1 2/m 1)	a=9.61944 Å,b=4.15255 Å c=7.20406 Å α=γ=90° β=126.20°	I Te Pd	0.50000 0.50000 0.50000 -0.16809 0.00000 -0.47290 0.00000 0.00000 0.00000
$IPtTe_2$	166[b](R -3 2/m)	a=4.11626 Å b=4.11626 Å c=23.44422 Å α=β=90°,γ=120°	Pt I Te	0.00000 0.00000 0.00000 0.00000 0.00000 0.50000 0.00000 0.00000 0.27680
$IRhTe_2$	166[a](R -3 2/m)	a=4.14203 Å b=4.14203 Å c=25.37537 Å α=β=90°,γ=120°	I Te Rh	0.00000 0.00000 0.00000 0.00000 0.00000 -0.11790 0.00000 0.00000 0.50000